VIBRATIONAL MICROSPECTROSCOPIC IMAGING OF NORMAL, WOUNDED, AND ARTIFICIAL SKIN

I. WOUND CHARACTERIZATION IN SKIN PUNCH BIOPSIES AND DIABETIC FOOT ULCERS

II. MOLECULAR ORGANIZATION OF HUMAN SKIN EQUIVALENTS

By

GUO YU

A Dissertation submitted to the

Graduate School-Newark

Rutgers, The State University of New Jersey

in partial fulfillment of the requirements

for the degree of

Doctor of Philosophy

Graduate Program in Chemistry

written under the direction of

Professor Richard Mendelsohn

and approved by

_____

_____

_____

_____

_____

Newark, New Jersey

May, 2013

ABSTRACT OF THE DISSERTATION

VIBRATIONAL MICROSPECTROSCOPIC IMAGING OF NORMAL, WOUNDED, AND ARTIFICIAL SKIN

I. WOUND CHARACTERIZATION IN SKIN PUNCH BIOPSIES AND DIABETIC FOOT ULCERS

II. MOLECULAR ORGANIZATION OF HUMAN SKIN EQUIVALENTS

By Guo Yu

Thesis director: Professor Richard Mendelsohn

Vibrational microspectroscopy and imaging offer several advantages for dermatological research, including drug permeation, monitoring of metabolism in vivo, and characterization of skin components. Applications of this technology to the investigation of wound healing in an *ex vivo* skin punch biopsy and in diabetic foot ulcers are demonstrated in this thesis, along with a comparison of the skin barrier in native skin and in human skin equivalents.

Three projects are described herein. The first is the study of lipid conformation in the migrating epithelial tongue during wound healing. The spatial distribution of lipid structure in an *ex vivo* skin wound healing model was studied using infrared microscopic imaging. Infrared images of samples at different times post wounding (Day 0, 2, 4 and 6) were collected and analyzed. The presence of a lipid class with disordered chains within and in the vicinity of the migrating epithelial tongue (MET) was revealed by analyzing spectra and spectral images of skin samples. The symmetric and asymmetric CH_2 stretching frequencies revealed the presence of disordered lipid phases while factor analysis of spectral regions of lipids and univariate analysis of spectral regions provide

the information concerning the spacial distribution of the lipids. Gene array analysis also provides evidence for an increase of an unsaturated lipid population. It is hypothesized that this lipid population increase might involve the epidermal growth factor receptor (EGFR) and that this lipid may play a role in controlling the migration of the MET and restoration of barrier functions at the wound site.

The second application concerns wound healing in diabetic foot ulcer (DFU). Wound healing in this pathological state is hindered by factors such as glycation of proteins and delayed inflammatory response; these factors also alter the structure and function of the wounded tissue itself. Our study revealed spectral differences between the healing DFU and non-healing DFU samples which were traced to glycation probably of keratin. These results might provide a better understanding wound healing mechanisms in this pathological state.

In the third project, vibrational microspectroscopy was applied to compare barrier physical properties in native and artificial skin. Barrier properties of human skin, pigskin, and two human skin equivalents (HSE), "Epiderm"^{TM} 200X with an enhanced barrier, and "Epiderm"^{TM} 200 with a normal barrier were studied. IR spectra reveal that the human stratum corneum (SC) contains a large portion of orthorhombically packed lipid chains at physiological temperature. However, this lipid packing motif occurs to a much lower extent or is absent entirely in pig skin and HSE. Confocal Raman microscopy revealed increased levels of cholesterol-enriched pockets within the HSE samples compared with native tissue. Taken together, these findings provide a useful set of experiments for preliminary characterization of HSE structure.

Acknowledgements

I would like to express my sincere gratitude to my advisor and mentor, Prof. Richard Mendelsohn, for his patience, encouragement, enthusiastic and elaborated guidance throughout my graduate studies. This dissertation would not have been possible without his continuous support and guidance.

Many thanks to Dr. Carol Flach, thank her for the help, patience and beneficial suggestions throughout my dissertation work.

I want thank my thesis committee: Prof. Agostino Pietrangelo, Prof. Bozena Michniak-Kohn, Prof. Jenny V. Lockard and Prof. Max Diem, for their suggestions and insightful comments that make the dissertation more complete.

I must also thank our collaborators Prof. Olivera Stojadinovic and Prof. Marjana Tomic-Canic, for their generous and professional support. Thanks to Prof. Joan I. Morrell, for her help with microtoming that is important to every piece of my research.

I thank former and current group members and friends in the Chemistry Department for their advice, encouragement and sharing these years with me.

Last but not the least; I thank my family for their infinite love. Without them, I see no way to get here.

Table of Contents

List of Figures

List of Tables

List of Abbreviations

3-Hydroxy-3-Methylglutaryl-Coenzyme A	HMG-CoA
3-Hydroxy-3-Methylglutaryl-Coenzyme A Synthase 1	HMGCS1
Advanced Glycation End Products	AGEs
Attenuated Total Reflectance	ATR
Charge-Coupled Device	CCD
Connective Tissue Growth Factor	CTGF
Diabetic Foot Ulcer	DFU
Dimethyl Sulfoxide	DMSO
Electron Microscope	EM
Endothelial Differentiation, Lysophosphatidic Acid G-Protein Coupled Receptor 2	EDG2
Epiderm 200	EpD 200
Epiderm 200X	EpD 200X
Epidermal Growth Factor	EGF
Epidermal Growth Factor Receptor	EGFR
Extracellular Matrix	ECM
Factor Analysis	FA
Fatty Acid Desaturases	FADS
Fibroblast Growth Factor	FGF
Fourier Transform Infrared	FTIR
High Performance Thin Layer Chromatography	HPTLC
Human Skin Equivalents	HSEs

Infrared	IR
Interleukin	IL
Mercurycadmium-Telluride	MCT
Metalloproteinases	MMPs
Migrating Epithelial Tongue	MET
N-(Carboxymethyl) Lysine	CML
Natural Moisturizing Factor	NMF
Near-Infrared	NIR
Nuclear Magnetic Resonance	NMR
Platelet-Derived Growth Factor	PDGF
Polymorphonuclear cells	PMNs
Principal Component	PC
Principal Component Analysis	PCA
Stearoyl-Coenzyme A desaturase	SCD
Stratum Corneum	SC
Three-Dimensional	3-D
Transforming Growth Factor	TGF
Transmission Electron Microscopy	TEM
Tumor Necrosis Factor	TNF
Two-Dimensional	2-D
Urokinase Plasminogen Activator	uPA
Vascular Endothelial Growth Factor	VEGF
Viable Epidermis	VE

Chapter 1 Introduction

1.1 Skin structure

Skin, the largest organ in the human body, provides the primary barrier against the surrounding environment. It protects the body against physical, chemical and biological insults. In addition, skin serves as a sensor for the body. It feels the temperature, moisture, pressure, pain, and allergen presence. To preserve homeostasis within the body, skin also responds to the environmental change by controlling blood flow and sweating (Tobin, *et al.*, 2006).

All the functions skin performs are related to its structure and chemical composition. Typically, skin is composed of four layers. From the outside in, these are the stratum corneum (SC), epidermis, dermis, and hypodermis (subcutaneous tissue) (Fig. 1-1) (Walters, *et al.*, 2002).

Stratum corneum, the outermost layer of the epidermis, is a 10-20 um thick layer, containing 15-25 layers of cornified cells. These flattened, stacked, hexagonal and cornified cells (corneocytes) are embedded in the intercellular lipid, and organized into a 'bricks-and-mortar' array. The thickness of SC varies depending on the site within the body. It's thickest in some areas such as the palms of the hand and soles of the feet. This is related to the physical and mechanical interaction with the environment.

Corneocytes are differentiated from the outermost layers of stratum granulosum cells, where the keratinocytes lose their nuclei and other cytoplasmic organelles as a result of the release of selective lysing enzymes. During differentiation, the contents of lamellar

granules in keratinocytes are also extruded into the intercellular space, providing important components for the SC.

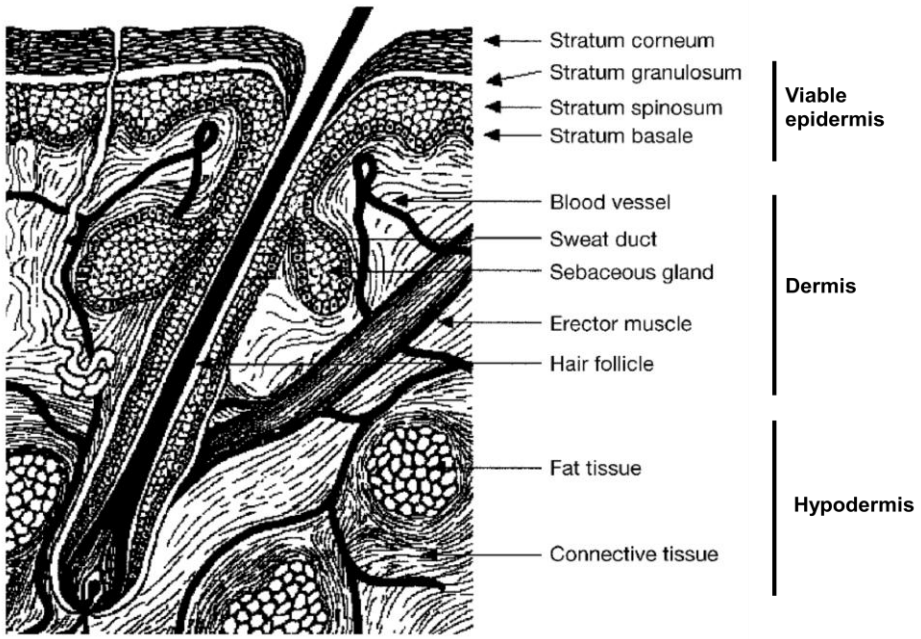

Fig. 1-1 A schematic cross-section through skin with anatomical features and sub-regions labeled (Walters, *et al.*, 2002)

The main components of corneocytes are insoluble bundled keratins (70%) and lipid (20%), which is encased in cell envelopes. Several proteins are cross-linked by disulfide and isopeptide bonds, forming protein envelopes attached covalently to lipid envelopes. These envelopes lie to the interior surface of the plasma membrane. The structural proteins in the envelopes include: involucrin, loricin, small proline-rich proteins, cystalin A and keratolinin, etc, which are very insoluble and resistant to chemical modification. Downing et al. found that the envelope involucrin's β-sheet confromation provides glutamate side chains as ester-linkers for N-ω-hydroxyceramides from the lipid envelope (Lazo, *et al.*, 1995). This is important for structural assembly of the intercellular lipid

lamellae. It is also suggested that the lipid envelopes may be the framework for the generation of intercellular lipid lamellae.

The intercellular region of the SC consists mainly of lipids and desmosomes. The lipids in the SC form a continuous phase composed of cholesterol (27%), ceramides (41%), free fatty acids (9%), cholesteryl esters (10%), and cholesteryl sulfate (2%). The composition varies with body site. Calcium and potassium ions are important for the regulation of the barrier function. It is suggested that the long-chain ceramides from the lipid envelope play a critical role in stabilizing the intercellular lipids by linking to the corneocyte protein envelope.

Below the stratum granulosum are several layers of the stratum spinosum. The mitosis of these cells has already ceased and differentiation to the stratum granulosum begins. Keratins in the cells are different form the stratum basale in that, numerous organelles and filaments are produced. The basal part of the stratum spinosum is connected to the the stratum basale, layers of undifferentiated but proliferative cells, by desmosomes.

The dermis not only serves as a scaffold of support for the epidermis, but also plays an important role in temperature, pressure and pain regulation. Compared with the epidermis, the dermal layer has fewer cells. The volume of this layer arises from extracellular matrix (ECM) produced by fibroblasts etc. This 0.1 – 0.5 cm thick ECM mainly contains collagenous fibers (90% of total dermal protein), some elastin and extrafibrillar matrix. Collagens possess a triple helix peptide chain structure with 1000 amino acids; they function in a variety of circumstances such as providing anchoring sites for epidermis, regulating angiogenesis etc. Type 1 collagen is the most abundant collagen in normal skin

(85-90%), followed by type 3 (8-11%) and type 5 (2-4%). Type 3 collagen increases during the early stages of wound healing and decreases in the remodelling stage.

Elastins are the other major ECM constituent of dermis. These stretchable fibers have a highly cross-linked structure, which makes elastins elastic and insoluble. Besides collagens and elastins, the extrafibrillar matrix is the third dermal material in dermis. This matrix contains proteoglycans, glycoproteins, water and hyaluronic acid. The extrafibrillar matrix functions in varies ways. Proteoglycans such as versican can associate with elastic fibres and hyaluronic aced to provide tautness (Hattori, *et al.*, 2011), while syndecans serve in the cell adhesion to ECM. Skin appendages including sweat glands, apocrine sweat glands, sebaceous glands, hair follicles and nails are also important constituents of the skin.

In this thesis, structural differences between normal human skin and other skin samples will be studied and discussed.

1.2 Cutaneous Wound Healing:

The most common interruption to the integrity of skin is wounding, which consists of physical or chemical insult making a cut through the skin. Generally, the wound healing process is divided into three sequential and overlapping phases: inflammation, new tissue formation and remodeling (Fig. 1-2) (Gurtner, *et al*., 2008).

Inflammation

The inflammation phase starts with hemostasis. Hemostasis begins right after wounding: blood clots are formed, and provide fast and provisional protection for the wound bed. The healing process is activated at the same time (Fig. 1-3). Fibrin is produced from

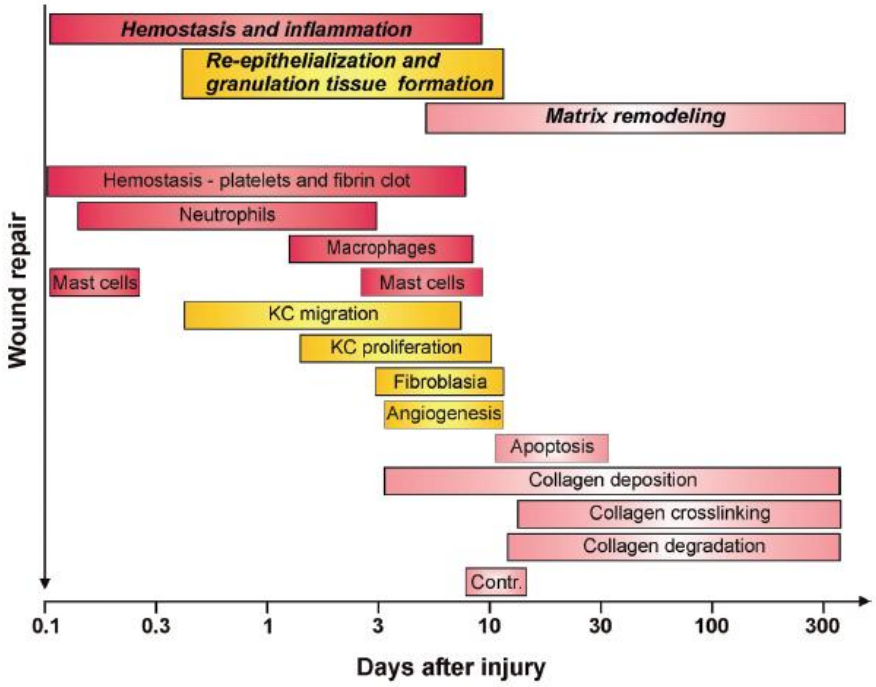

Fig. 1-2 The phases and functional events of cutaneous wound healing (Toriseva, *et al*., 2009).

fibrinogen by thrombin and bound to platelet to produce blood clots, a viable, dynamic protein and cell matrix lattice for inflammatory cells, fibroblasts and growth factors. After the formation of a clot, fibrin begins to degrade. Platelets are also activated by thrombin: the number of surface receptors increases, granules are released and aggregated. Platelet granules contain fibrinogen, albumin, platelet-derived growth factor (PDGF), transforming growth factor (TGF)-B, epidermal growth factor (EGF), *etc.* (Gieringer, *et al*., 2010; Baum, *et al*., 2005). These proteins and growth factors participate in all phases

of healing. Growth factors and cytokines such as platelet-derived growth factor and interleukin (IL)-8 attract polymorphonuclear cells (PMNs) to the wound site. The PMNs remove cellular debris, foreign particles and bacteria, they also provide several proinflammatory cytokines such as IL-1a, IL-6 and tumor necrosis factor (TNF)-a. Macrophages appear after PMNs, these cells are transformed from circulating monocytes, they also clean the wound site as PMNs. Macrophages secrete a series of growth factors and cytokines, which can stimulate fibroblasts to produce collagen or stimulate the differentiation of fibroblast to myofibroblast, etc. Angiogenesis is also stimulated by macrophage released factors. T lymphocytes regulate the healing process by producing factors such as connective tissue growth factor (CTGF). Fibrocytes, a group of fibroblast-like cells, participate in the inflammatory phase through cytokine and collagen production, and supply of chemokines and growth factors.

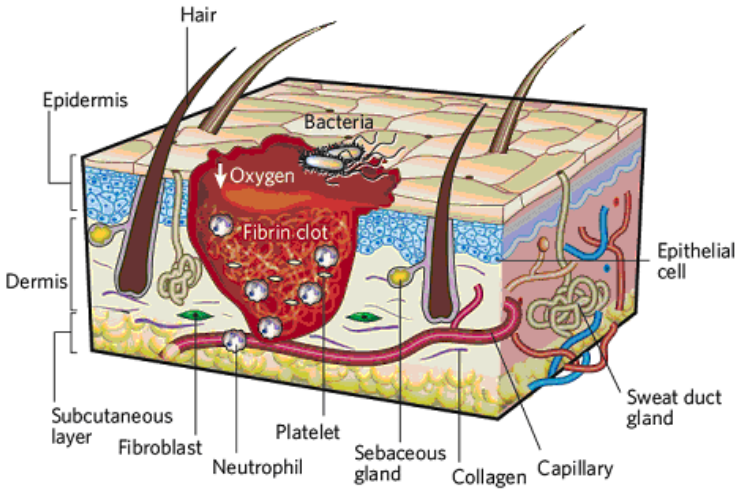

Fig. 1-3 Inflammation phase of cutaneous wound healing (Gurtner, *et al*., 2008).

The inflammation phase provides a burst of information, which sends signals to prepare necessary materials for the next stage.

New tissue formation

The new tissue formation phase includes re-epithelialization, granulation and angiogenesis (Fig. 1-4). Re-epithelialization begins within hours after injury. Cells close to the wound and hair bulges convert to keratinocytes, start to proliferate and migrate as the migrating epithelial tongue (MET): intracellular tonofilaments retract; intercellular desmosomes are dissolved to break the connections between cells; peripheral cytoplasmic actin filaments are formed to provide tracks for cell movement. The epidermal keratinocytes also detach from dermal cells for movement. During the process, keratinocytes produce a series of enzymes such as urokinase plasminogen activator (uPA) to cleave the path of migration. Enzymes such as metalloproteinase (MMPs), collagenase and plasmin clear the way by degrading the ECM and collagen (Toriseva, *et al*., 2009). Integrin receptors expressed on keratinocytes facilitate the interaction with ECM and fibrin clot in the wound space. A number of factors including growth factors, cytokines, damaged resident lipids, leptin and nitric oxide etc. are involved in the regulation of epithelialization. Connections between epidermal keratinocytes and dermal cells are reestablished after epithelialization. The whole epithelialization can be completed in 24 to 48 hours in a shallow or sutured wound.

Granulation begins at about four days after injury: activated by growth factors and ECM molecules, fibroblasts begin to proliferate and migrate. These fibroblasts, which derived

from differentiated cells close to the wound and nearby undifferentiated mesenchymal cells, start to replace the fibrin matrix with granulation tissue. The extracellular matrix

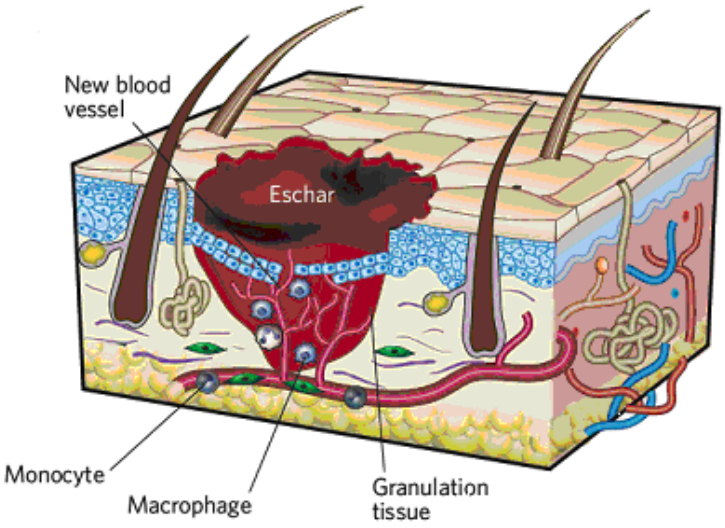

Fig. 1-4 New tissue formation phase of cutaneous wound healing (Gurtner, *et al*.,2008)

(ECM), which contains fibrin, fibronectin and hyaluronic acid, provides a scaffold for fibroblasts to migrate: Because of the interaction between fibroblast surface integrins and the ECM components such as fibrin and fibronectin, the cells migrate along the fibers in the extracellular matrix. During migration, fibroblasts produce several metalloprotainases (MMPs) to clean out "obstacles" such as cellular debris and fibrils which block the way (Toriseva, *et al*., 2009; Baum, *et al*., 2005). Concurrent with migration and proliferation, fibroblasts also start the production of new ECM to take the place of the provisional ECM formed during the inflammation phase. The new ECM is mainly composed of collagen, glycoaminoglycan and proteoglycans rather than fibrin in the provisional one. Various cytokines and growth factors such as IL-1 and TNF-α are produced by

fibroblasts to regulate other wound healing process like angiogenesis and cell-matrix interaction.

Angiogenesis is stimulated by environmental change, growth factors and cytokines. VEGF, FGF, angiopoietin, and TGF-β are the four most important growth factors in this process. Stimulated by growth factors, the endothelial cells begin to migrate along the individual fibrils in the ECM on the second day following injury. Integrins expressed in endothelial cells serve as receptors that interact with ECM components such as fibronectin. Like fibroblasts, endothelial cells produce MMPs and plasmin to clean the way for migration. MMPs expressed here also function in the degradation of basement membrane and in the formation of new tubules and capillaries. The new capillaries mature after stimulation of angiopoietins. Angiogenesis ceases when the new granulation tissue fills the wound. Several antiangiogenesis factors and matrix molecules regulate this process. The new tissue formation phase provide an improved but not final protection: reepthelialization provides fast coverage to the wound bed, while granulation enhances the strength of the ECM, and angiogenesis provides a nutrition supply for the tissue.

Remodeling

The remodeling phase, also termed the maturation phase, includes wound contraction and extracellular-matrix reorganization (Boateng, *et al.*, 2008). This phase begins approximately 4 to 5 days after wounding and lasts up to a year or more. Activated by PDGF and TGF- β, fibroblasts start a phenotypic morphogenesis: large bundles of microfilaments disposed on the plasma membrane, and finally these cells convert to

myofibroblasts which are responsible for the compaction of connective tissue and wound contraction.

The extracellular-matrix reorganization is a balance of decomposition and construction. Several enzymes and growth factors such as MMP, PDGF and TGF- β take part in this

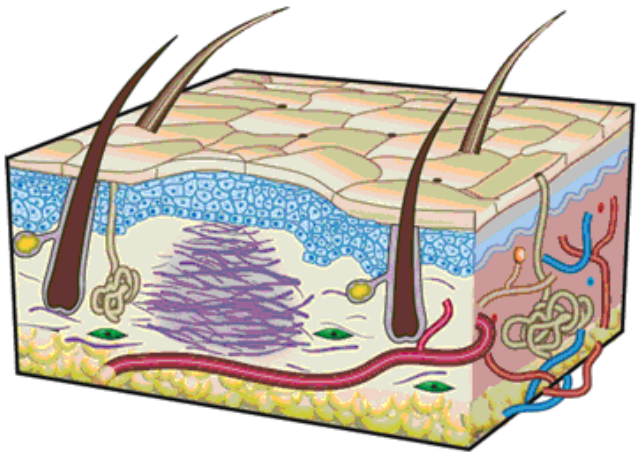

Fig. 1-5 Remodeling phase of cutaneous wound healing (Gurtner, *et al*., 2008)

process. Cells which produce these enzymes and factors, include endothelial cells, macrophages, fibroblasts and myofibroblasts undergo a programmed apoptosis during this phase. By breaking down the 'old' collagen and producing 'new' collagen, the wound structure is changed and the wound strength increases with time. Collagen synthesis peaks at about day 21 post-wounding, and then the rate slows down. Haphazardly arranged collagen fibrils are decomposed, new fibrils with increased interfibril binding and increased diameter are produced and rearranged, which results in an increased tensile strength and decreased wound thickness. As the remodeling process proceeds, the abundance of type 1 collagen (well organized and strong) increases and type 3 collagen (less organized and weak) decreases. The wound strength will increase

from 20% of normal skin at day 21 to a maximum of 80% of normal skin by 6 months post-wounding, it will never regain the same strength of uninjured skin. Skin appendages such as hair follicles cannot be regenerated.

1.3 Human Skin Equivalent Structure

The need for curing chronic skin wounds and acute large area skin wounds drives the search for skin transplants (Clark, *et al*., 2007; MacNeil, S. 2007). Because of the limited availability of human skin grafts, several human skin equivalents were developed to provide a safe and effective substitutes. The general methodology of preparing HSE is through culturing epidermal or fibroblast cells *etc.* in certain media such as bovine serum and degradable polymers. There are mainly three types of equivalents: epidermal layer substitutes, dermal layer substitutes, and full thickness substitute with epidermal and dermal layers. These human skin equivalents can provide a rapid cover to the wound bed; while preventing water loss and bacterial sepsis. In the meantime, the healing process can be facilitated by the growth factors and enzymes supplied by keratinocytes and fibroblasts in the human skin equivalents (Clark, *et al*., 2007).

Besides the equivalents used in clinical practice, there are many products developed for various laboratory purposes. Governmental regulations about in vivo/vitro human and animal experimental procedures, the need for reducing the experimental cost and the development of effective experimental models are the main reasons for developing human skin equivalents (HSEs). Efforts have been made to develop HSEs which mimic the normal human skin morphologically, structurally and chemically. There are already a number of products in the market e.g. Epiderm^{TM}, EpiSkin^{TM}, Skin Ethic^{TM} *etc.*, that are

widely used for studying skin barrier penetration, skin diseases, skin metabolism, irritancy, *etc.*(Netzlaff, F. *et al.*, 2005). The structure of these products can be divided into three categories: epithelial substitutes, dermal substitutes and full thickness substitutes. Compared with HSEs for clinical purposes, HSE for laboratory use has fewer requirements, i.e., human body compatibility is no longer a consideration. Although these products are all cultured from human keratinocytes and fibroblasts, their structures vary based on different culture conditions, and these differences can fit a variety of research purposes (Ponec, M. *et al.*, 2000). In this research, the structures of two different types of human skin equivalent were studied and compared with each other and with native skin.

1.4 Current Method for Skin Studies

Many methods have been applied to probe the morphology, structure and composition study of skin. Several common techniques will be summarized below.

Staining is one of the most traditional and popular methods for examining morphology. This technique requires fixation of samples in certain solvents, followed by the staining of samples with different chemicals. The fixation procedure takes as long as a few hours or a day, and is followed by embedding the samples in paraffin or other polymers. Staining requires chemicals or probes that can be attached to the sample and can be observed under condition such as uv/visible light. The organic/inorganic chemicals and solvents used in this method may disturb the native structure. In addition, sample preparation is time consuming and sometimes chemical stains for specific purposes are not available.

Transmission electron microscopy (TEM) is a popular method for the study of skin micro structure. This technique can even give detailed information concerning cell organelles, such as mitochondria and desmosomes. However, sample preparation for TEM can be time consuming and laborious: paraformaldehyde fixation is required, heavy metals such as osmium, ruthenium or gold are needed for staining to increase electron density.

X-ray diffraction measurements including small angle and wide angle X-ray scattering are also used in the study of skin micro structure. These methods permit studies at the molecular structure level of phenomena such as lamellar ordering of stratum corneum lipids, which cannot be observed by most other techniques. The technique requires only a small amount of sample (several milligrams) taken out of the specimens: this advantage can be a disadvantage. A complete understanding of an entire skin sample cannot be readily acquired.

High performance thin layer chromatography (HPTLC) is employed to study lipid composition in skin samples. This method can provide the composition and semi-quantitative information of different kinds of lipids in skin. However, the sample preparation for this method requires the extraction of lipids with organic solvent such as chloroform and methanol. Lipid organization and structural information cannot be obtained via this way.

Confocal Raman microscopy is now used for the study of skin. Compared with methods mentioned above, this technique offers some advantages: 1). It is a non-invasive method, and requires no skin sample sectioning or sampling. This means that the experiment can be carried out in vivo, which is of great value for real time studies of changes in the skin

such as those which occur as results of drug metabolism. No staining or probe is required for this method and the tissue's original state can be preserved; 2). The spatial resolution of confocal Raman microscopy can reach 1-3 μm for our study of skin samples, A good size scale which permits evaluation of the 'big picture' as well as understanding of the sample structure at molecular level. In addition, different sub layers of skin can be distinguished at this resolution. The Rayleigh's criterion for the diffraction-limited resolution of a microscope is given by the following equation: $\Delta x=0.61\lambda/N.A.$, Δx is the minimum separation between resolved points, λ is the wavelength and N.A. is the numerical aperture of the objective. In our study, λ= 785 nm for the laser, N.A.=1.35 for the oil immersion objective and Δx can reach 354.7 nm for the diffraction-limited resolution; 3). The confocal approach enables acquisition of a 2D or 3D map of the sample; 4). Composition and structural information can be extracted from the spectra. The benefits of confocal Raman microscopy as noted above will be demonstrated in this thesis.

As in traditional staining methods, IR microscopic imaging requires sectioning of skin samples; usually the sample will be microtomed to a thickness of 5 um. However, no additional stain or probes will be needed; skin sections can be measured without further treatment. The resolution of this method can is 6~10 μm depending on the wavelengths of interest which is worse than confocal Raman microscopy. Spectra from IR images provide chemical and physical information from the sample; this information can be used to provide a chemical structure map of a sample unaffected by any external factors. Many studies of pathological tissues have been acquired by IR imaging. Herein, we demonstrate the application of IR microscopic imaging in studies of skin wound healing and human

skin equivalents. In this thesis, several new applications of vibrational spectroscopy and imaging will be demonstrated including: (1) studies of lipid conformation in cutaneous wound healing; (2) comparison of barrier physical properties in native and human skin equivalents; (3) tracking of skin structure changes and development in diabetic foot ulcer wounds.

Chapter 2 Materials and Experimental Methods

2.1 Materials

Trypsin, EpD-200X and EpD-200 were purchased from MatTek Coporation (Ashland, MA). Pig skin biopsies from Yucatan white, hairless pigs were purchased from Sinclair Research Center, Inc. (Columbia, MO) and human skin wound biopsies were the generous gift from Dr. Tomic-Canic at the University of Miami. Protocols for skin collection were reviewed and accepted by institute review boards.

2.2 Microspectroscopy and imaging

2.2.1 IR Microscopy

Instrumentation: The Perkin Elmer Spotlight system 300 shown in Fig. 2-1 was used in these studies. The system consists of an FT-IR spectrometer coupled to an IR microscope. A high performance Cassegrain mirror system with a wide collection angle is used in the microscope system to collect the radiation.

Fig. 2-1 Perkin Elmer Spotlight system 300 (http://www.perkinelmer.com/Catalog/Product/ID/L1860116).

The system includes both a lower and an upper Cassegrain. The lower Cassegrain condenses the radiation from the spectrometer and focuses the beam at the sample being measured; the upper Cassegrain collects radiation that has passed the sample point and sends it to a linear array (8 x 2 detector elements) of mercury-cadmium-telluride (MCT) detector via a variable aperture and dichroic mirror. The sample is located on a motorized stage which can be moved with high precision in the X, Y and Z directions to sample the point of interest. A visible-light image of the sample can also be acquired via a camera and view system integrated into the imager; this device enables us to observe and track the points of interest in the sample directly and efficiently.

Sample preparation for IR imaging of intact skin sections: Skin samples were fast frozen in liquid N_2 to preserve their integrity and to minimize ice damage. Frozen samples were then fixed on a metal chuck stage and sealed in ice. After 5 minutes of stabilization in a microtoming instrument (Bright Instrument Company LTD, Huntington, England, Hacker Instrument, Inc., Fairfield, N.J.) that works at -30℃, skin samples were microtomed to a thickness of 5 microns and carefully transferred to CaF_2 windows. IR spectra were acquired after the sample was dried for 30 minutes in air. 32 scans were co-added, pixel size was 6.26 x 6.25 μm^2, and 8 cm^{-1} spectral resolution was utilized.

2.2.2 Raman Microscopy

Instrumentation: A Kaiser Optical Systems Raman Microprobe shown in Fig. 2-2 was used in this study. A solid-state diode laser emitting at a wavelength of 785 nm was used for excitation to minimize fluorescence from skin samples. The laser light is transmitted to the confocal microscope system via a single-mode excitation optical fiber. The power

of the laser exiting the sample is ~ 6-8 mW. The back scattered Raman light is collected by the same objective and passed through the microscope system, and is then delivered to the detector by a collection optical fiber.

The laser light sent toward the detector passes a notch filter which is used to reject the input laser signal from Rayleigh scattering. A pair of sequentially stacked transmission gratings are then used to extend the wavelength range without significant diffraction efficiency loss. The diffracted light is finally collected by the charge-coupled device (CCD) with a linear array detector possessing 128 pixels on the spatial axis and 1024 pixels on the spectral axis. The spectral range covered is 100 cm^{-1} to 3450 cm^{-1} while data are encoded at 0.3 cm^{-1} interval. A motorized sample stage which can be moved with

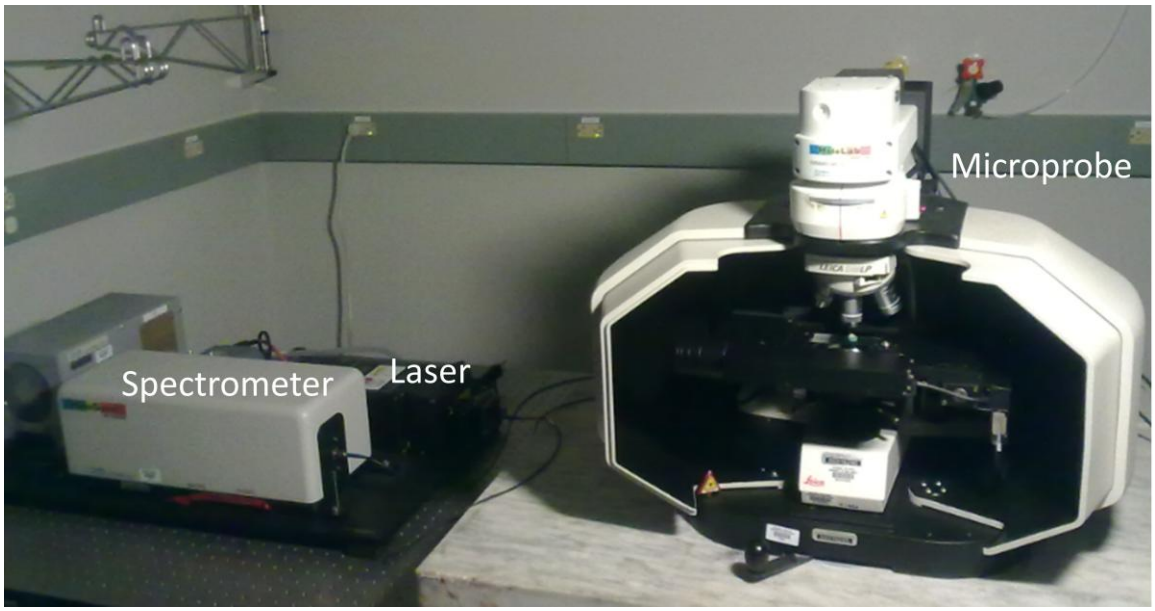

Fig. 2-2 Kaiser Optical Systems Raman Microprobe.

high precision in the X, Y and Z directions is integrated in an enclosed system which is used to reject interference from environmental light. The stage is controlled by a stage controller. Spectra can be taken in defined 3 dimensions by precise control of the stage.

Confocality is achieved by using a pair of pinhole apertures set as illustrated in the following Fig. 2-3. The first pinhole aperture is set in front of the laser light source to reduce light scattering and improve the image quality. The second pinhole aperture is placed between the microscope objectives so that the scattered rays originated from any out-of-focus point on the sample will be filtered.

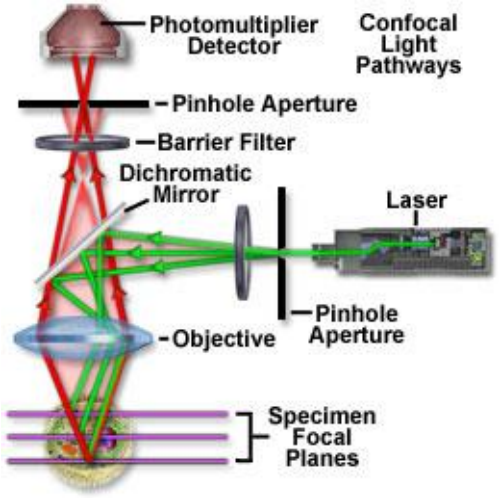

Fig. 2-3 Optical scheme for confocal spectroscopy including confocal microscope, spectrometer and multi-channel CCD detector (http://www.olympusconfocal.com /theory/index.html).

As shown in Fig. 2-3, the laser light has to travel through layers of different materials with different refractive indices. It's hard to calculate the precise refraction of these materials for each sample. In our experiments on intact skin samples, 1-2 μm lateral and 2-3 μm confocal resolution was achieved. In the intact skin Raman mapping experiments,

a Leica oil immersion objective with a 1.35 numeric aperture was used to minimize the Raman scattering losses and to acquire better resolution.

Raman microscopy of intact skin: Skin samples were cut to a size of ~ 1 x 1 cm^2, 2 mm thick sections. Surfaces were cleaned with cotton swabs several times with care, and then sealed in a bronze cell with a microscope cover slip (the thickness is ~130 μm to 170 μm) on the top of stratum corneum. The cover glass was pressed down onto the skin surface to ensure a good contact with skin. The edges of the cover glass were sealed with clay to retain the moisture. Raman spectra were then acquired with step size of 4 microns, an exposure time of 60 seconds and 4 accumulations. Cosmic ray corrections were applied. An oil immersion lens (100 x) was used, and was placed in contact with the external surface of the microscope cover slip used to cover the sample.

2.2.3 FT-IR Spectroscopy

Instrumentation: A Thermo Nicolet 6700 Spectrometer was used for bulk phase samples. It is a traditional FT-IR spectrometer; used in the transmission mode for thermotropic FT-IR measurements of the stratum corneum.

FT-IR Spectroscopy of skin stratum corneum samples: Skin was treated with a 0.5% (w/v) trypsin in pH 7.4 phosphate buffered saline solution at the air-liquid interface for 24 hours. The stratum corneun (SC) was then peeled off and transferred to zinc selenide (ZnSe) window and dried under house vacuum for 1 – 2 days. The dried SC sample was covered with another ZnSe window.

Fig. 2-4 Thermo Scientific Nicolet 6700 FT-IR spectrometer
(http://www.thermoscientific.com/ecomm/servlet/productsdetail?productId=11961710&groupType=PRODUCT&searchType=0&storeId=11152).

This ZnSe 'sandwich' was placed in a temperature-controlled IR cell (Harrick Scientific, Ossining, NY, USA). Spectra of the dried SC were taken at a temperature interval of 3℃ from 20 to 84℃. Temperature was controlled with a circulating water bath and monitored with a thermocouple (Fisher Scientific Thermostat, Model 9001, Pittsburgh, PA, USA) embedded in the sample cell.

The preparation of Epiderm SC samples was different from human and pig skin SC samples because there is no distinct physical property difference between the SC and epidermal layers. In this preparation Epiderm samples were treated in trypsin solution for two days until no additional physical change could be observed, (i.e. sample thicknesses after this time remained constant) and no more tissue could be removed from the viable epidermis side by scratching with a tweezers.

2.3 Data processing

An IR image of a skin sample acquired in these experiments contains thousands of spectra. In order to evaluate the information in these spectra, two multivariate statistical methods, principal component analysis (PCA), and factor analysis (FA), were applied.

PCA is used when a large number of variables are highly correlated. It can be used either as a data reduction method, or as a classification method by means of comparison of the projection of a data set in its original form onto loading vectors calculated for each component. PCA describes the important information in a spectral image in terms of a relatively small number of channels, the so-called principal components (PC). The PCs are ranked in terms of the percentage of total spectral variance that they explain. The first PC identified accounts for most of the variance in the data. The second PC identified accounts for the second largest amount of variance in the data and is uncorrelated with the first PC and so on. A loading vector is generated for each PC, giving the spectral dependence of that component. The projection of the original pixel spectra on the set of loading vectors yields a set of scores, which provide a representation of those spectra in terms of the PCs.

The loading vectors resulting from a PCA calculation (or any of the other ISys tools which generate loading images) are generally not pure component spectra. If the spectral image is proportional to an absorbance image, then to the extent that Beer's Law is obeyed, the intensity at the ij'th pixel and k'th wavelength can be expanded as $L_{ijk} \sim \sum c_m e_{mk}$ where c_m is the concentration of species m and the e_{mk} is the molar extinction coefficient of species m at the k'th wavelength of the spectrum. If we 'unfold' the image

cube into a two dimensional array, X, with pixel spectra along each row, we can then express that matrix as a sum of outer products of concentration vectors and pure component spectra: $X=\sum_m c_m e_{mk}$ Where each c_m is a $p \times 1$ vector (p = number of pixels in the image), each component of which represents the concentration of species m at a particular pixel. E_m is a $1 \times k$ (k = number of channels in each pixel spectrum) spectrum of species m. An analogous factorization will hold if X represents Raman data.

Note that PCA produces a similar looking factorization of the data matrix: $X=\sum_j S_j L_j$, where the S_j are the scores and the L_j are the corresponding loadings. If the data matrix can be factorized in terms of concentrations and spectra, then it will be possible to find transformations between the L_j and the e_m. The corresponding score images will then represent the concentration profiles of the various components. Factor analysis seeks transformations from the abstract PCA loading vectors which correspond to the directions of maximum uncorrelated variance, to the true underlying factors, in this case single-component absorption spectra, which explain the data.

Factor analysis (FA) is a useful method to detect structure in the relationships between variables in order to classify them (Hardle, *et al.*, 2012). It is a variable reduction technique which identifies the number of latent constructs and the underlying factor structure of a set of variables. FA includes unique factors, and errors due to unreliability in measurement, and hypothesizes underlying constructs, i.e. variables not measured directly. In contrast, PCA doesn't represent underlying constructs and most of the PCs yielded cannot be interpreted. However, PCA can be used as a quick approach to generate component scores which can be a prediction for choosing the number of factors.

Isys (Version 3.1.1.18) was used in the current studied for FA. Generally, there are three steps for the operation: determination of the number of factors, diagonalization of the original covariance matrix, and score segregation.

Determination of the number of factors is an interactive process; this is because of the characteristics of skin samples: statistically meaningful factors may or may not be biologically informative. PCA was run before FA to provide the number of factors contained in a group of data sets. In the beginning, two or more factors than the expected number can be set for the diagonalization of the original covariance matrix to see if this certain number of factors can be obtained after score segregation. The factor number should be decreased if the iterative process for the factor loading calculation does not converge or if the signal-noise level is too low for any factor loading plot. Sometimes the factor number should also be decreased if some factor loading plots appear very similar (differences are not distinguishable enough). In contrast, the factor number can also be increased for more possible new findings if all the factors generated might be biologically informative.

The set of factors loading error threshold is also a trade-off between the numbers of factors can be generated and independently distributed finite variance of the factor loadings: it decides the convergence criterion. Thus, a higher loading error threshold generates more factors with less finite variance, and a lower loading error threshold

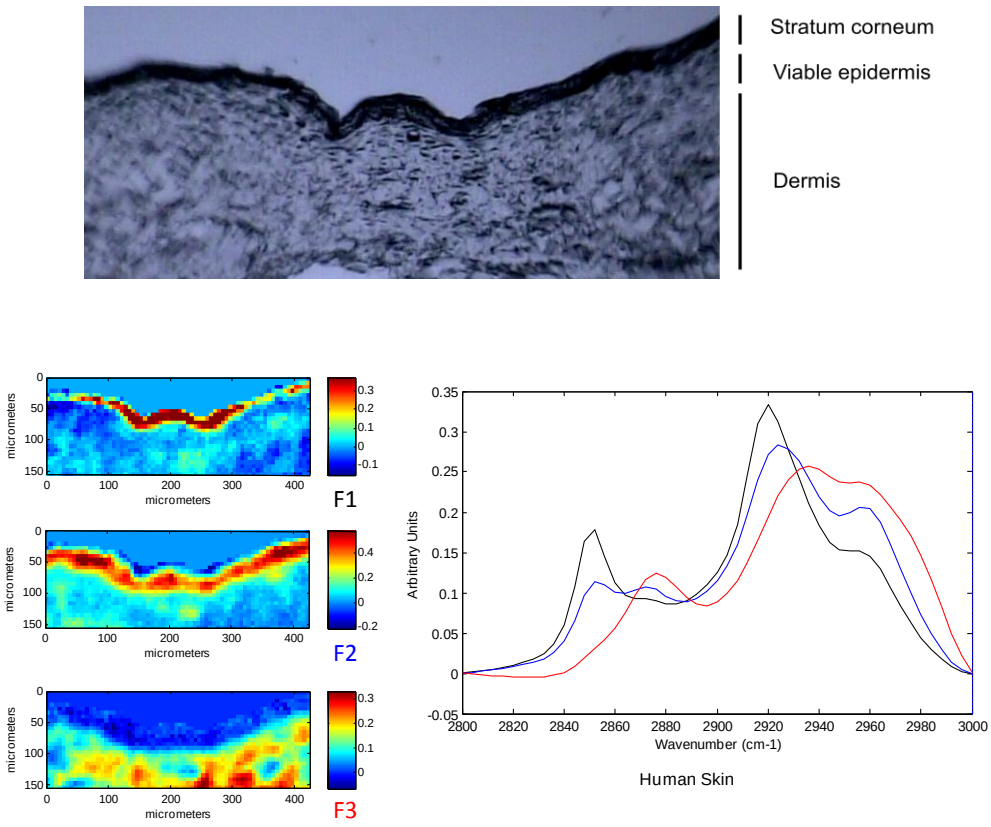

Fig. 2-5 Factor analysis of a human skin section. (A) An optical micrograph of a 5-um thick microtomed unstained skin section depicting the stratum corneum, epidermis and dermis regions. (B) Factor analysis of the IR spectral data set of skin section. Left: three factor score images. Right: three factor loadings.

produces fewer factors with higher finite variance. For the procedures performed by Isys the loading error threshold is usually set as 1 x 10^{-12} for the FA.

An example of factor analysis is shown in Fig. 2-5 and Fig. 2-6. Three factors are utilized for the analysis here. The number was limited to three for convenience of comparison between the visible image and factor loading images. In both human skin

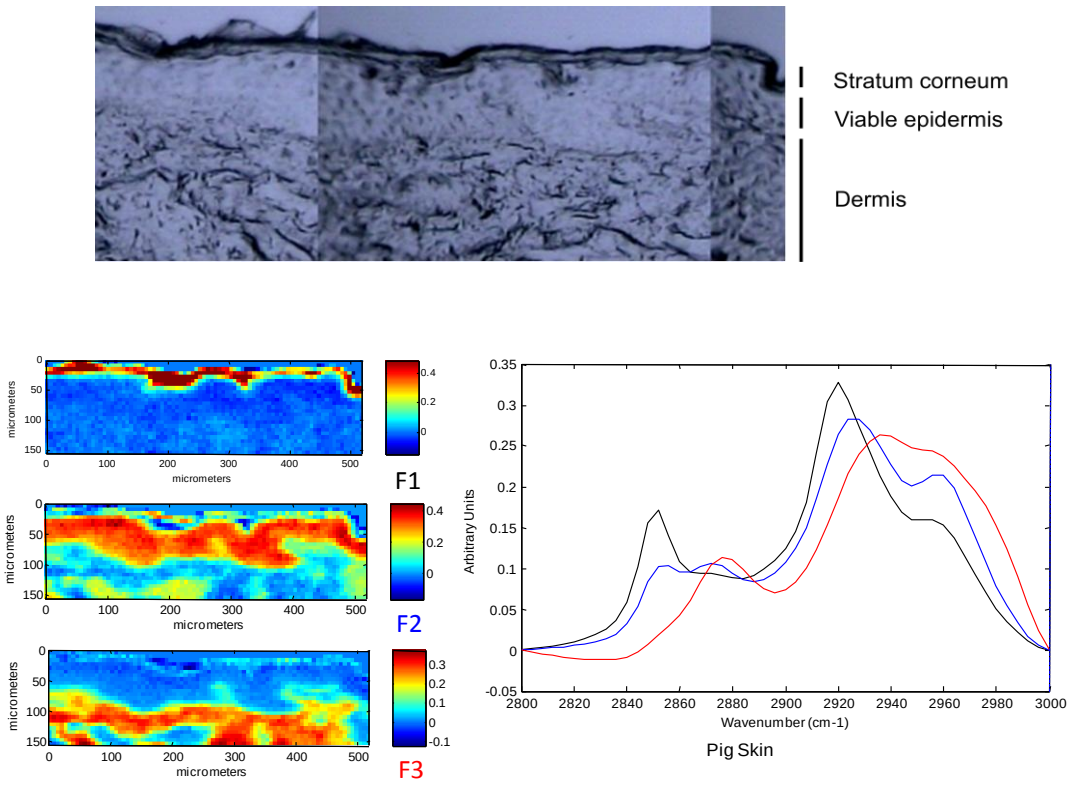

Fig. 2-6 Factor analysis of a pig skin section. (A) An optical micrograph of a 5-um thick microtomed unstained skin section depicting the stratum corneum, epidermis and dermis regions. (B) Factor analysis of the IR data set of skin section. Left: three factor score images. Right: three factor loadings.

and pig skin samples, three different factors which represent stratum corneum, epidermis and dermis resulted from factor analysis.

To compare component properties in different samples, spectral images were concatenated and analyzed for the consistency of the method. Shown in Fig. 2-7 is a concatenated image of human skin and pig skin samples. The FA of this concatenated image shows consistency with the above mentioned trials of two separate FA analyses.

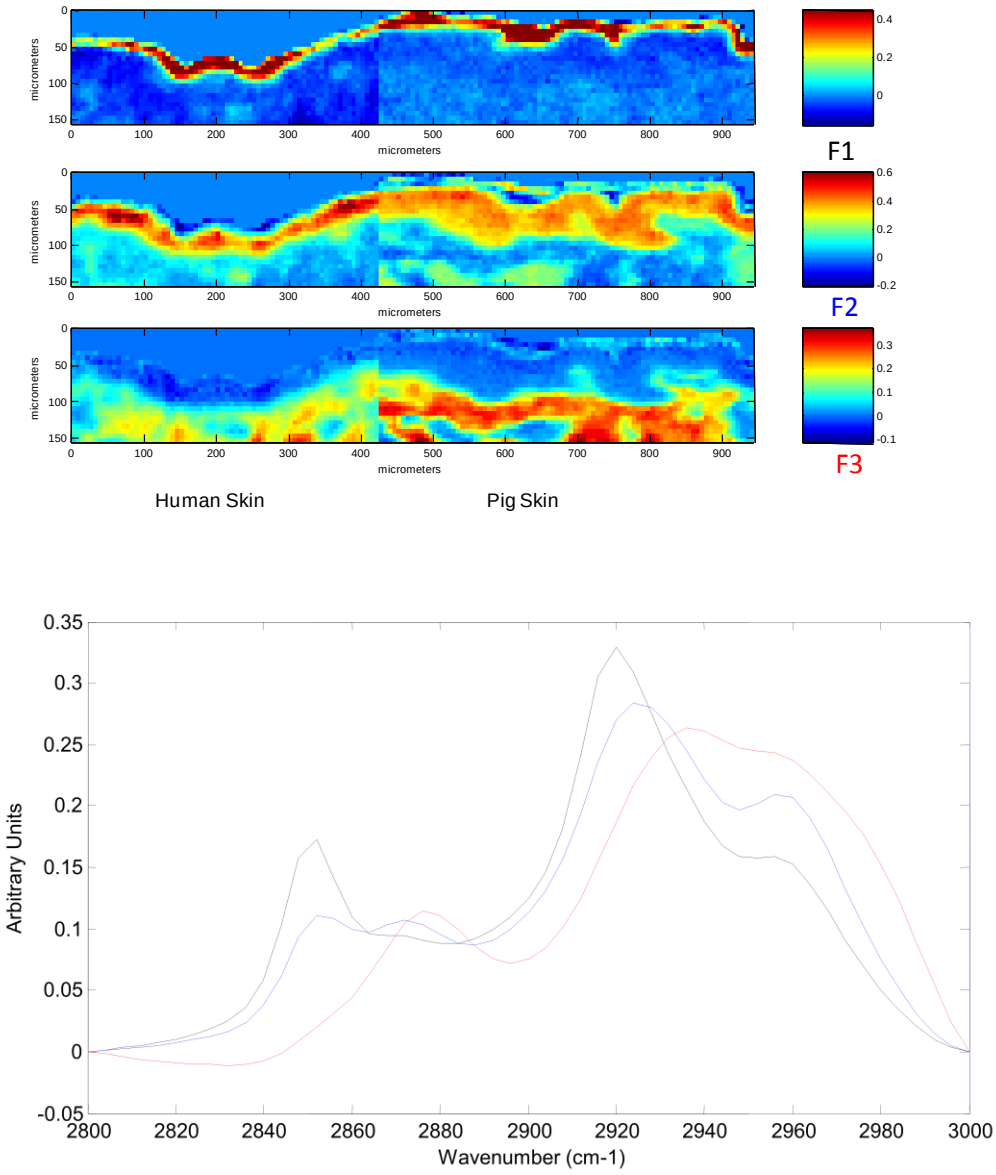

Fig. 2-7 Factor analysis of concatenated spectral data. Above: three factor score images. Below: three factor loadings.

For samples with different signal strength (usually caused by different absorbance values from different thicknesses between sample sections), univariate methods such as peak height ratio, frequency shifts can be employed for data evaluation. FA reveals the latent

constructs in the data pool, and this can be used as a hint for further clarification and interpretation of the hidden structural information in the sample.

Chapter 3 Infrared microscopic imaging of cutaneous wound healing: lipid conformation in the migrating epithelial tongue

3.1 Introduction

The healing of cutaneous wounds is a highly temporally and spatially coordinated process occurring in three sequential, yet overlapping stages. Initial rapid sealing of the damaged site is achieved via clot formation. Re-epithelialization commences within a few hours of the injury and requires activation, proliferation, and migration of keratinocytes from the wound edge to cover the denuded wound area. The keratinocyte layer (known as the migrating epithelial tongue) covers the wound bed within seven to nine days. This process is followed by the reformation of a stratified epidermal layer and finally matrix remodeling that may last up to a year (Singer, *et al*., 1999)

The molecular components and control mechanisms involved at various stages of the healing process have been analyzed extensively. Molecular techniques have monitored the spatial distribution of particular keratins as healing progresses (Chan, *et al*., 2008; Patel, *et al*., 2006; Usui, *et al*., 2005). In contrast, biophysical approaches for imaging the spatial distribution and structural characteristics of particular molecules such as lipids, proteins, or exogenous materials in the healing tissue are sparse. Such information is of particular interest for characterization of therapeutic interventions, including the study of interfaces between native skin and three dimensional skin equivalents, and the action and spatial distribution of exogenous agents.

The paucity of biophysical imaging studies of wound healing arises from the lack of available technologies to carry out such experiments. The standard high-resolution structural methods of biophysics [x-ray diffraction, nuclear magnetic resonance (NMR)]

are inapplicable in heterogeneous tissue environments. Thus, alternative methods that can identify and image tissue constituents and molecular structure are required. In the past 15 to 20 years, Fourier transform infrared (FTIR) microscopic imaging has evolved to study tissues (Zhang, *et al*., 2007; Mendelsohn, *et al*., 2003), and to characterize pathological states (Gazi, *et al*., 2007; Bird, *et al*., 2008; Schubert, *et al*., 2010). The approach provides spatially resolved compositional and molecular structure information. The experiment produces a full IR spectrum from each pixel and requires neither probe molecules nor application of stains. A single IR imaging dataset generates a multitude of images, each displaying the spatial distribution of an IR spectral parameter. IR measurements are generally performed in the transmission mode and require microtoming of sections to a thickness of ~5 μm. IR absorption provides intense signals (molar extinction coefficients range up to 10^3); thus, high-quality spectra may be generated fairly quickly (6,000 to 10,000 complete mid-IR spectra from pixels of dimension ~6.25 × 6.25 μm^2 may be acquired in 40 min), and images from millimeter-sized areas may be readily generated.

We have recently used both IR microscopic imaging and confocal Raman microscopy to monitor the permeation and metabolism of exogenous agents in skin and to track natural moisturizing factor levels and solvent-induced structural changes in single corneocytes (Zhang, *et al*., 2006; Zhang, *et al*., 2007). In addition, in our first wound healing study (Chan, *et al*., 2008), we used an ex vivo cutaneous wound healing model in combination with immunohistochemistry and gene array analysis to correlate the gene expression profile with IR images during re-epithelization. Multivariate statistical analyses of IR images were correlated with immunofluorescence staining patterns, demonstrating the

feasibility of acquiring structural and spatial information from the major proteins involved in wound healing. In the current study, we focused on the evaluation of lipid structure in the vicinity of the migrating epithelial tongue (MET). Aside from proteins, the major contributor to the IR spectra of skin arises from lipid components. In addition, the study of skin lipids by IR spectroscopy and imaging has been widespread over the past decade (Moore, *et al*., 1997; Pensack, *et al*., 2006; Bocheva, *et al*., 2008; Gooris, *et al*., 2007). Robust correlations between vibrational spectra and lipid chain conformational order and packing have thereby become available (Mendelsohn, *et al*., 1986). Therefore, we used IR microscopic imaging to evaluate the lipid chain conformation within and in the vicinity of the MET at various time points following wounding. A thorough review of the wound healing literature has produced only two experimental results evaluating changes in skin lipids during wound healing. A bioanalytical report from Kozel'tsev *et al*., (Kozel'tsev, *et al*., 2006) tracked lipid content in a rat skin wound field. A four-fold increase in triglyceride levels was observed five days into regeneration, especially in the granulation tissue. In addition, Vicanova *et al* (Vicanova, *et al*., 1998) used skin substitutes grafted onto athymic nude mice as a long-term model for the stratum corneum (SC) barrier organization. The initially impaired barrier was restored to near normal at six months postgrafting.

In additional studies by several groups over the past decade (Pike, *et al*., 2005; Ringerike, *et al*., 2001; Lambert, *et al*., 2008; Mathay, *et al*., 2008), the putative role of lipid rafts in controlling the function of cell signaling molecules, involving the epidermal growth factor receptor (EGFR), has been investigated through biochemical and molecular approaches. EGFR controls keratinocyte proliferation and motility. Here, we utilized IR

imaging and gene array analysis to further elucidate the spatial distribution and conformational order of lipids during ex vivo wound healing.

3.2 Materials and Methods

3.2.1 Human Organ Culture Wound Healing Model

Human skin specimens were obtained from reduction surgery in accordance with institutional protocols and were used to generate acute wounds as previously described (Tomic-Canic, *et al*., 2007). A 3-mm biopsy punch was used to create an acute wound and skin specimens were maintained at the air-liquid interface with Dulbecco's Modified Eagle's Medium (DMEM) (BioWhittaker), antibiotic/antimycotic and fetal bovine serum (Gemini Bio-Products) at 37℃, 5% CO2, and 95% relative humidity. Specimens were collected for further analyses at zero, two, four, and six days postwounding.

3.2.2 Gene Array Data Analysis

Microarray Suite 5.0 (Affymetrix) was used by our collaborators at the University of Miami for data extraction and for further analysis. Data Mining Tool 3.0 (Affymetrix, Santa Clara, CA) and GeneSpring Software 7.3.1 (Silicon Genetics, Redwood City, CA) were used for normalization, degree of change, and p-value calculations. Samples were normalized per chip to the 50th percentile and per gene to a median. Statistical comparisons of expression level between each condition were performed using the ANOVA test. Only genes with a p-value less than 0.05 were considered to be statistically significant. Differential expressions of transcripts were determined by calculating the degree of change. Genes were considered regulated if the expression levels differed more than two-fold relative to healthy, unwounded skin.

3.2.3 IR Imaging Experiments

For IR imaging, the experimental methods follow the protocols as introduced in Chapter 2. A high-precision XY sample stage permitted the collection of IR images (pixel area of 6.25 μm^2) over 0.5 × 0.5 mm sample areas. Spectral resolution was 8 cm^{-1}. Overall, three sets of separate skin specimens were prepared and analyzed. Results shown are representative of all three sets.

3.2.4 IR Data Analysis

IR spectral data analyses follow the protocols as introduced in Chapter 2.

3.3 Results

3.3.1 IR Imaging Identifies Changes in Epidermal Lipid Composition during Wound Healing

A typical sequence of events in the current skin wound healing explant model is depicted in a series of visible micrographs from separate sections at various times (control, zero, two, four, and six days) following wounding, as shown in Fig. 3-1. In the unwounded control skin, the SC is clearly evident at the top of the micrograph. The image acquired immediately following wounding (day zero) shows both the presence of the residual SC at the top right as well as the wounded area on the left lacking the more dense SC tissue. The MET becomes visible covering some ¾ to ⅞ of the surface from the right-hand to the left-central areas of the day two and day four images, respectively. Coulombe (Coulombe, *et al*., 2003) states that the MET arises from elongated keratinocytes that originate from the basal and suprabasal layers of the epidermis near the wound. In the current instance, the presence of the MET indicates that epithelialization occurs in the explants and thus provides evidence for the validity of the model for biophysical studies.

No uncovered area was found in the day six image, suggesting that the MET had covered the entire wounded area, i.e., the epithelization stage was complete.

The visible micrographs in Fig. 3-1 do not contain molecular level information and thus cannot be used to identify molecular constituents present in the image. IR microscopic analysis permits identification of particular molecular classes, and furthermore, permits elucidation of structural characteristics of particular constituents. Typical, single-pixel, raw IR spectra from different skin regions are overlaid in Fig. 3-2 with bands of interest marked. The high signal-to-noise level in the spectra is immediately apparent. Subtle changes in several bands are observed comparing the spectra of different skin regions.

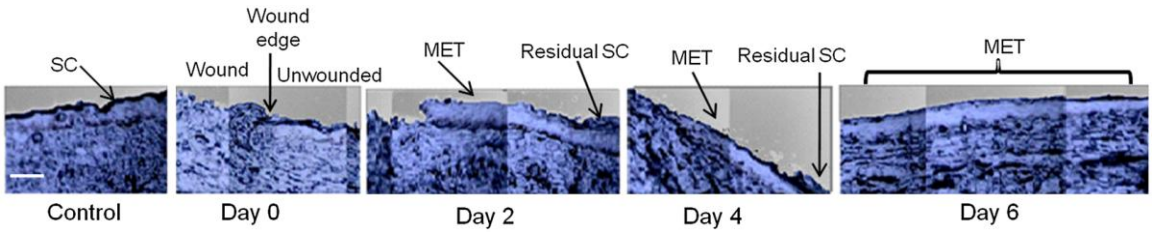

Fig. 3-1 Visible images of microtomed wound healing sections. The control is a nonwounded section of human skin (left image) and the remaining images are marked according to a postwounding timeframe (left to right, day zero, two, four, and six). The 100-μm scale bar applies to all the images.

Our analytical strategy was to apply factor analysis to the IR images within spectral regions known to be sensitive to particular aspects of molecular structure.

The sensitivity of several IR spectral regions to various aspects of skin, wound constituents, and particular elements of molecular structure are shown in Figs. 3-3 to 3-7. Fig. 3-3 (a) shows two factor loadings in the 1490 to 1720 cm^{-1} region, which encompasses the Amide I (mostly peptide bond C=O stretch, frequency range 1620 to 1690 cm^{-1}) and Amide II (mostly mixed N-H in-plane bend and C=N stretch, frequency

range 1510 to 1560 cm^{-1}) vibrational modes. The factor loadings predominantly arise from keratin-rich and collagen- rich regions of the tissue. The Amide I spectral region shows substantial differences between these two proteins and provides a powerful means to distinguish between them in skin tissue. Collagen is characterized by a major Amide I peak near 1660 cm^{-1} and a shoulder near 1636 cm^{-1} while keratin is characterized by a

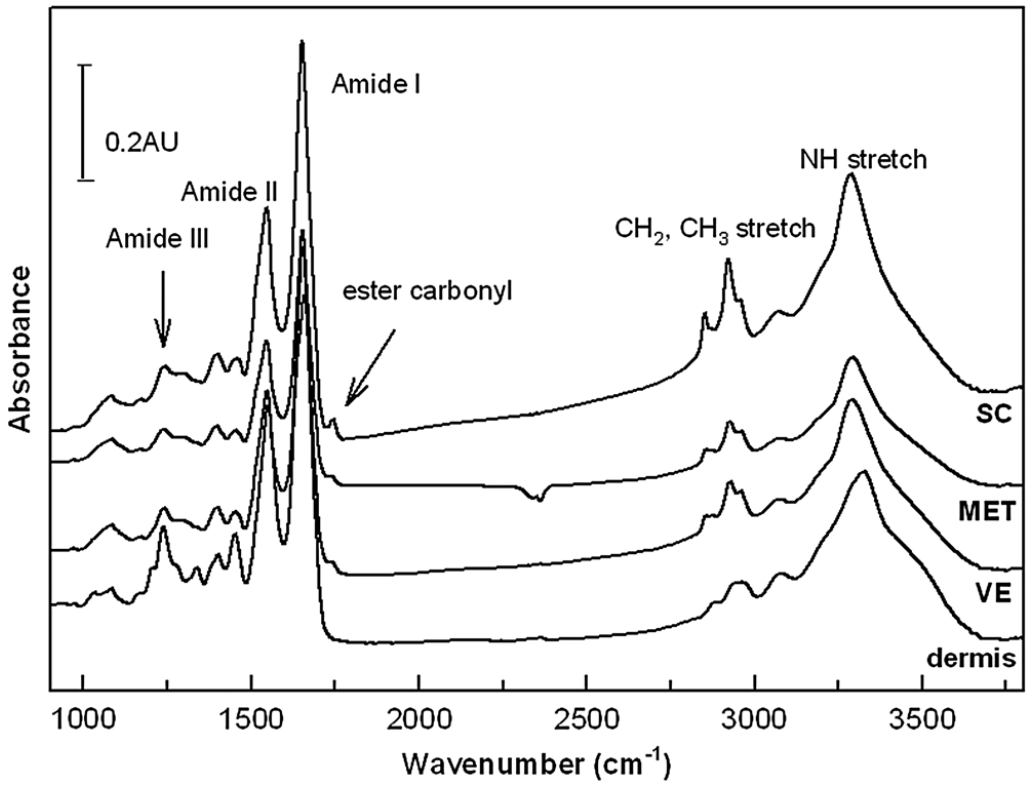

Fig. 3-2 Typical single-pixel IR spectra from various regions of microtomed human skin sections: stratum corneum (SC), migrating epithelial tongue (MET), viable epidermis (VE), and dermis as marked. Spectra of the SC, VE, and dermis were obtained from the day zero section (see Fig. 1) in the unwounded area and the spectrum of the MET was acquired from the day two section.

more symmetric single band at 1652 cm^{-1}. Significant differences in the Amide II patterns are also noted. Images of the factor scores for this spectral region in the day zero and day two samples help us to distinguish keratin in the epidermis and MET from the underlying dermis [Fig. 3-3(b), top and bottom, respectively]. The chemical identification

of proteins known to be located at particular sites [see visible images in Fig. 3-3(c)], e.g., keratin in the MET, collagen in the dermis, provides a useful validation of the factor analysis method.

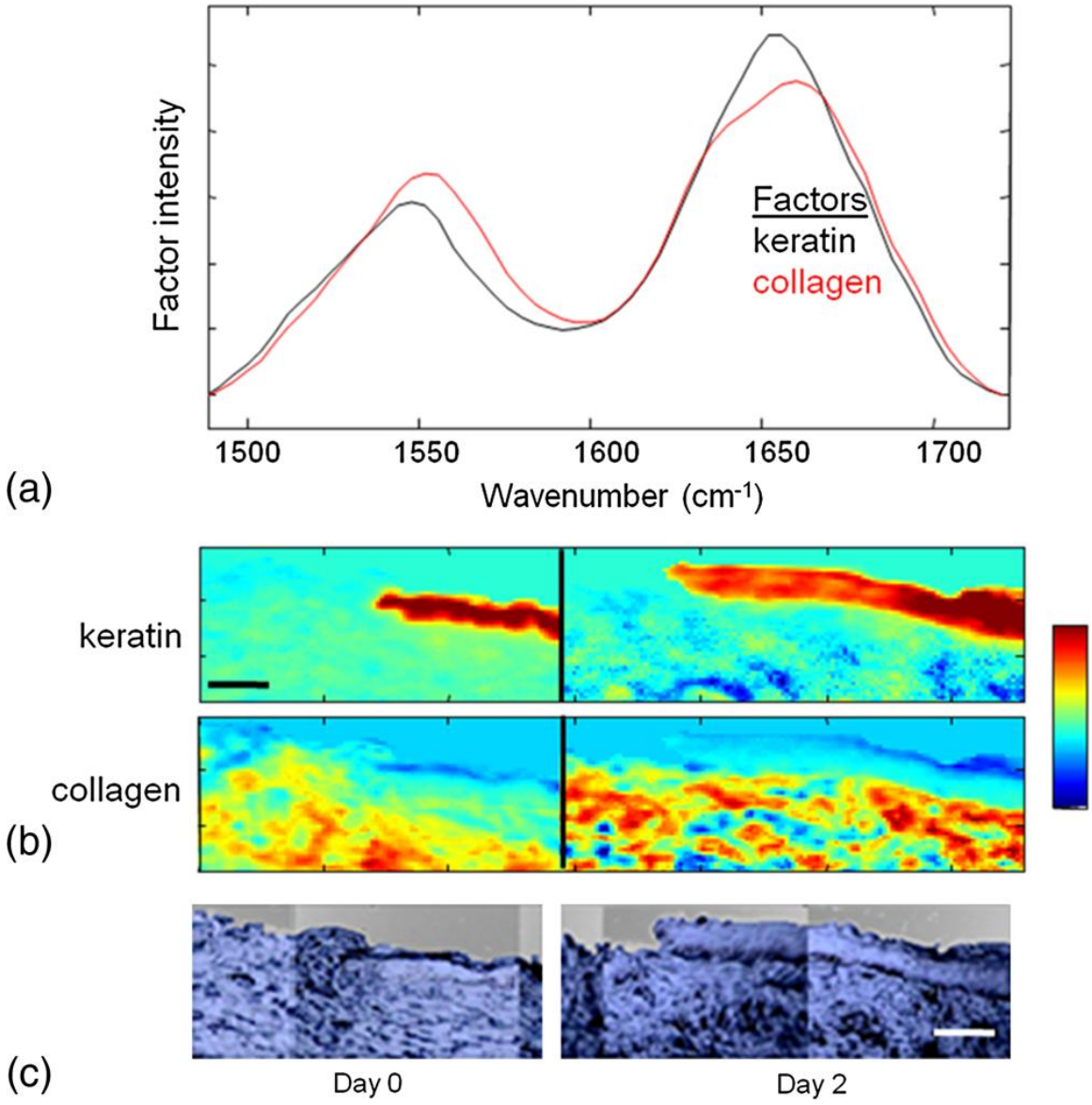

Fig. 3-3 Detection and IR characterization of the spatial distribution of keratin-rich and collagen-rich regions in day zero and day two of ex vivo wound healing model human skin sections utilizing factor analysis conducted over the 1490 to 1720 cm^{-1} region. (a) Two factor loadings in the 1490 to 1720 cm^{-1} region. (b) IR score images for two factor loadings with color coding scale bar of scores as follows: red > yellow > blue. (c) Visible images of the two sample sections. The 100-μm scale bar applies to all the images.

Factor loadings and score images from the C-H stretching region (2800 to 3000 cm^{-1}) calculated from the full set of skin sections (Fig. 3-1) are shown in Fig. 3-4(a) and 3-4(b), respectively. This spectral region was not analyzed in our prior study. The spectral patterns arise from relatively conformationally ordered (L1) or disordered (L2) lipid acyl chains. Acyl chains that are conformationally well-ordered, essentially all-trans, are characterized by methylene symmetric stretching (2850 cm^{-1}) and asymmetric stretching (2920 cm^{-1}) frequencies shifted down by 2 to 4 cm^{-1} from their counterparts in disordered chains. In our study, the methylene symmetric stretching mode (v_{sym} CH_2) is shifted from 2854.5 to 2852.7 cm^{-1} while the asymmetric stretching mode shifted from 2925.4 to 2922.3 cm^{-1}, reflecting an increased degree of conformational order in the chains.

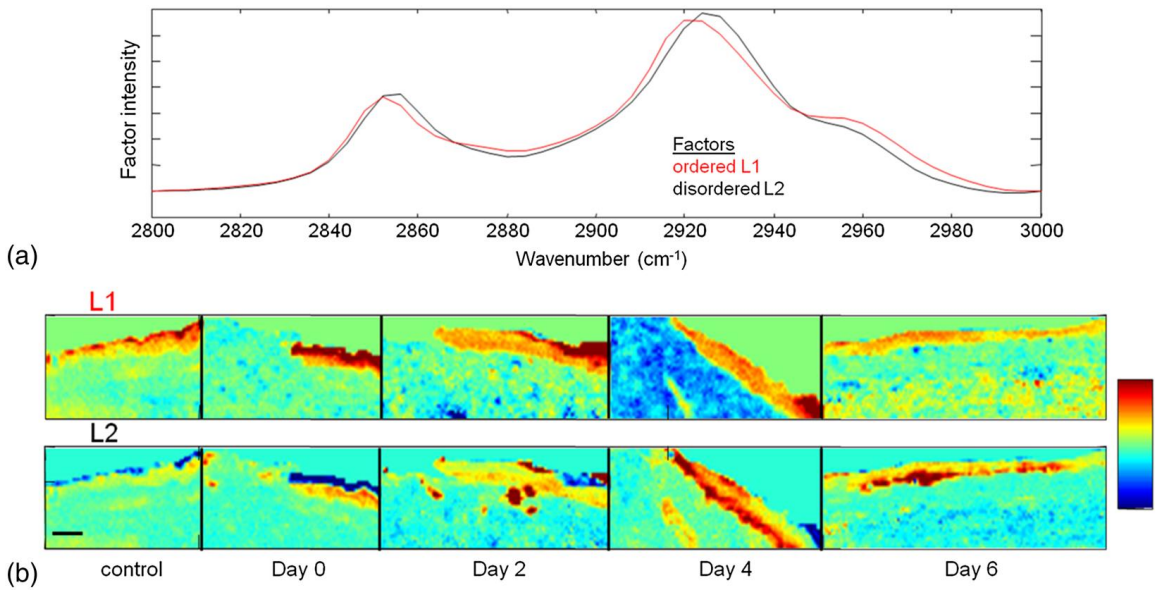

Fig. 3-4 IR characterization of acyl chain conformational order (factor analysis conducted over the 2800 to 3000 cm^{-1} region) of a nonwounded control and wounded skin sections at time points zero, two, four, and six days postwounding. (a) Factor loadings of L1, ordered chains (red) and L2, disordered chains (black). (b) Score images of L1 and L2 for the control and day zero, two, four, and six sections as marked. The 100-μm scale bar applies to all the images.

Concatenated images of factor scores generated from the loadings (L1 and L2) in the methylene stretching region are shown in Fig. 3-4(b) from the control skin and day zero, two, four, and six wound sections. The highest scores from the ordered lipid factor labeled L1 in the control and the period immediately following wounding (day zero) coincide with the SC as observed in the visual micrographs. The factor score images for L1 also confirm the identification of a small region of residual SC on the right side of the day two and four wound sections. In addition, slightly lower scores for factor L1 were observed in the nonwounded area of the viable epidermis (VE) (control, day zero and two) and throughout the MET (day two to six). Upon wounding, the spatial and temporal evolution of scores for the disordered lipid factor, L2, is notable.

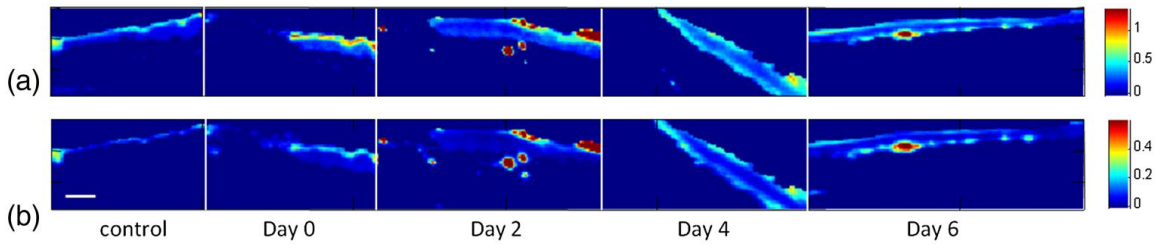

Fig. 3-5 Images of univariate IR spectral parameters for the nonwounded control sample and wounded skin sections at time points zero, two, four, and six days postwounding. The integrated area of the symmetric CH_2 stretching band (2840 to 2868 cm^{-1}) is displayed in (a) and provides a semi-quantitative measure of the lipid acyl chain concentration. The integrated area of the high-frequency half of the lipid carbonyl (1744 to 1756 cm^{-1}) is displayed in (b). The high-frequency half of the band was used to avoid interference from the incompletely resolved strong Amide I band (see Fig. 2). The 100-μm scale bar applies to all the images.

Scores were quite low throughout the entire area of the control skin sample and appear somewhat higher in the VE at day zero. The dark blue area limited to the top 10 to 20 μm in the control and at day zero and two in the images represents very low scores for the disordered lipid factor (L2) in the SC as anticipated. In the day two image, small pockets

with high scores, mostly in the area basal to the MET, were observed, prior to spreading throughout the basal area and leading edge of the MET on day four. The day six section displays high scores concentrated in the lower to middle regions of the newly formed epidermal layer.

A simple univariate measure was used to analyze the spatial distribution of the relative concentration of lipid in the dataset. The images shown in Fig. 3-5(a) were generated from the integrated area of the ν_{sym} CH_2 stretching band. The regions with high lipid content coincide with the ordered lipid located in the SC, as described above for Fig. 3-4(b) (L1 images) and with the disordered lipid (L2 images), especially the lipid pockets in the day two and day six sections. To aid in the identification of the chemical species of the disordered lipid, factor analysis was performed on the lipid C=O (1720 to 1770 cm^{-1}) stretching region (results not shown). Two major factors were observed, differing by about 2 cm^{-1} in carbonyl peak position. Both peak positions (1743 and 1745 cm^{-1}) are characteristic of (lipid) ester carbonyls, although the origin of the difference is unknown. To further probe the spatial distribution of the lipid carbonyl content, the integrated area of this band was measured and the data is displayed in Fig. 3-5(b) for the wound healing dataset. The areas with the highest concentration of lipid carbonyl intensity overlap with regions of high lipid acyl chain concentration [Fig. 3-5(b)] in the day two, four, and six sections and notably with the disordered lipid pockets as mentioned above.

An alternative means to characterize the physical state of the lipid present in a healing wound from a similar skin specimen six days after wounding is presented in Fig. 3- 6. We used a different manner of univariate measure to directly image lipid conformation via the methylene symmetric stretching frequency [Fig. 3-6(a)]. Herein, the 1 to 2 cm^{-1}

increase due to chain disorder in v_{sym} CH_2 comparing the SC to the VE is directly evident [Fig. 3-6(a)]. This type of univariate measure represents an average of the proportions of ordered and disordered lipid at a given location, whereas factor analysis provides separate images of ordered and disordered lipid species. In Fig. 3-6(a), lipids with disordered acyl chains, average v_{sym} CH_2 observed at 2854 to 2854.5 cm^{-1}, are observed throughout the MET and VE in the nonwounded area, along with the more ordered lipids of the SC (v_{sym}

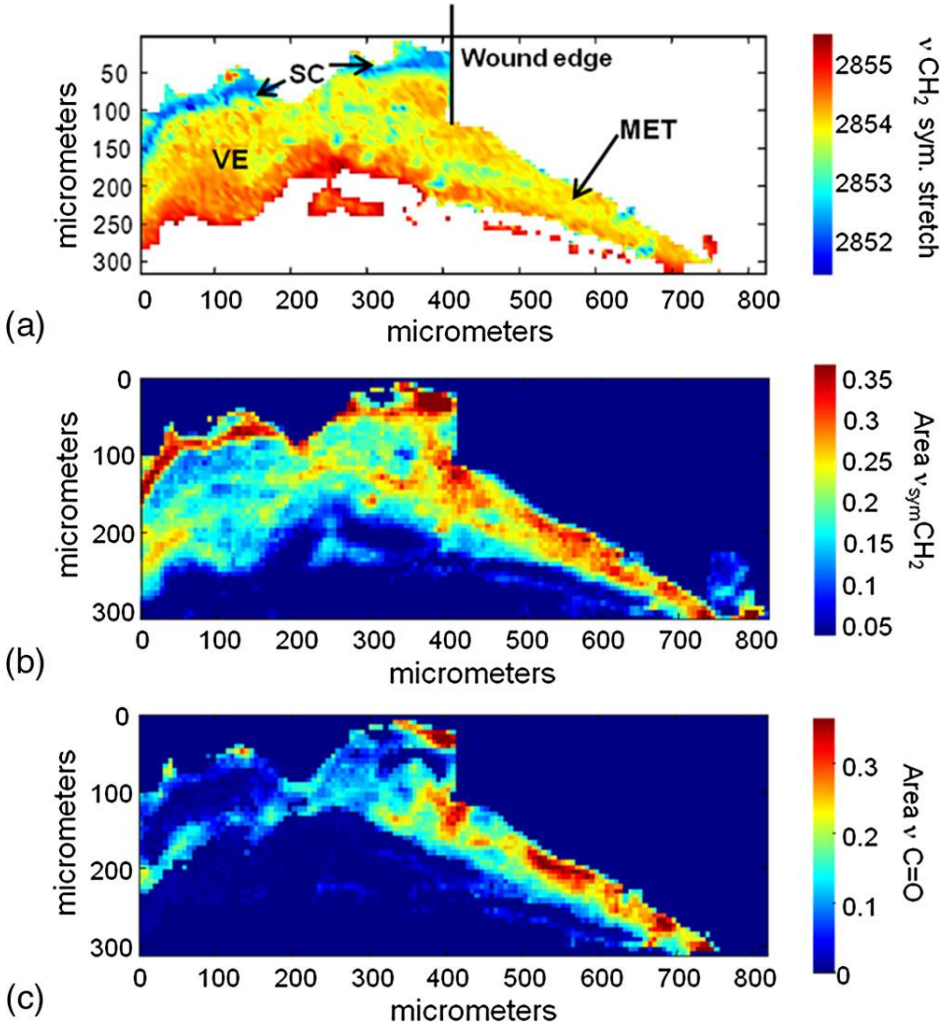

Fig. 3-6 Images of univariate IR spectral parameters for a day six postwounding section delineating (a) lipid acyl chain conformational order via the methylene symmetric stretching frequency, (b) relative lipid acyl chain concentration via the integrated area of the methylene symmetric stretching band (2840 to 2864 cm^{-1}), and (c) relative lipid ester concentration via the integrated area of the C=O stretching band (1728 to 1772 cm^{-1}).

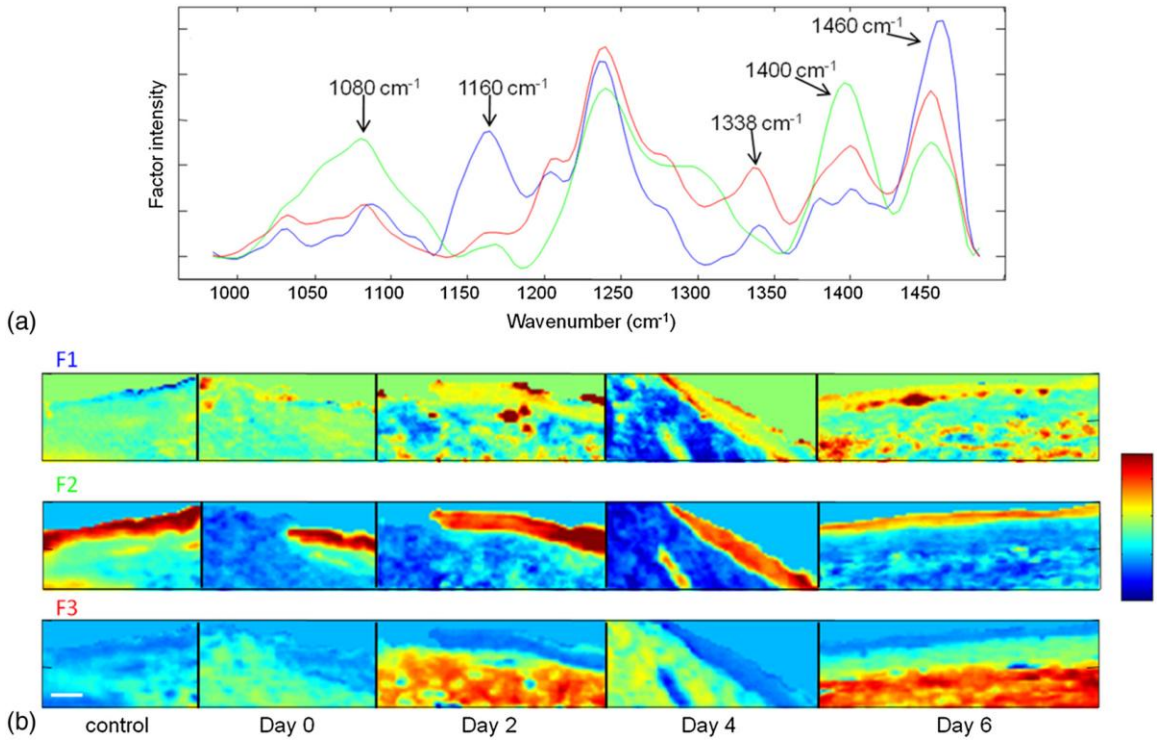

Fig. 3-7 IR characterization (factor analysis conducted over the 980 to 1480 cm^{-1} region) of nonwounded control and wounded skin samples at time points zero, two, four, and six days postwounding. (a) Factor loadings of F1 (blue), F2 (green), and F3 (red). (b) Score images of these three factors, showing spatial distribution of different chemical species for the control and day zero, two, four, and six sections as marked. The 100-μm scale bar applies to all the images.

CH_2 at 2852 cm^{-1}).

A measure of the integrated area of the methylene symmetric stretching band, an approximate monitor of relative lipid acyl chain concentration, is displayed in Fig. 3-6(b). An equivalent plot for the lipid C=O stretch is shown in Fig. 3-6(c). Comparison of Fig. 3-6(b) and 3-6(c) reveals that there is a significant overlap of area in the MET with both high methylene and carbonyl stretching intensities. Small pockets at the edge of the wound are observed as well. However, the integrated area of both stretching modes appears to be lower in the bulk of the nonwounded VE. As anticipated, high methylene

intensity in the SC [Fig. 3-6(b)] is also evident in the image. Further characterization of lipid, collagen, and keratin molecules is available through factor analysis of the 980 to 1480 cm^{-1} region (Fig. 3-7). We used the same wound specimens shown in Fig. 3-1. The three factor loadings shown in Fig. 3-7(a) reveal distinct spectral features unique to different chemical species as deduced from their spatial distributions displayed in the score images [Fig. 3-7(b)]. High scores for factor loading 1 (F1) map to the regions previously assigned to disordered lipid [Fig. 3-4(b), L2] and a relatively higher ester C=O content [Fig. 3-5(b)]. Correlating the three images, we tentatively assign the 1160 cm^{-1} band to the C-O single bond stretch of the ester group. The fact that the methylene bending mode, 1460 cm^{-1}, is the highest-intensity band in F1 is also consistent with the presence of lipid in these regions. Thus, the proposition that disordered lipids are present in regions below and within the lower areas of the MET is reasonably justified. Score images for the remaining two factor loadings, F2 and F3, display discrete spatial distributions readily assigned to keratin in the epidermis and collagen in the dermis, respectively. In addition, several spectral features observed in the loadings along with factor analysis in the Amide I and II region (data not shown) are consistent with this assignment. For example, the intense band at 1400 cm^{-1} in F2 arises from the symmetric carboxylate stretch. Keratin has a larger percentage of Glu and Asp that contain carboxylate side chains than collagen, thus indicating its presence. The loading F3, arising from the collagen-rich dermis, is also confirmed by the presence of the 1338 cm^{-1} peak. This mode has been tentatively assigned as a CH_2 wagging mode of the proline ring (Jackson, *et al*., 1995; Camacho, *et al*., 2001).

3.3.2 Gene Expression Analyses Reveal Deregulation of Genes Involved in Lipid Metabolism

Gene expression analyses were done by our collaborators Marjana Tomic-Canic *et al.* at the University of Miami. Microarray analyses were utilized by to study gene expression in ex vivo wounded skin specimens two and four days postwounding compared to healthy control skin (Table 1). Changes were detected in genes involved in lipid metabolism. Fatty acid desaturases 1 and 3 (FADS1 and FADS3), enzymes that regulate

Table 3-1 List of lipid metabolism-related genes regulated two and four days after wounding.

Fold change Wound/control		Gene symbol	Unigene component	Function
48 h	96 h			
−1.44	−2.01	DBT	Dihydrolipoamide branched chain transacylase	Lipid metabolism
−2.33	1.30	DLST	Dihydrolipoamide *S*-succinyltransferase	Lipid metabolism
3.28	2.80	FABP4	Fatty acid binding protein 4, adipocyte	Lipid metabolism
2.27	5.06	FADS1	Fatty acid desaturase 1	Lipid metabolism
1.63	2.48	FADS3	Fatty acid desaturase 3	Lipid metabolism
1.02	2.47	HELO1	Homolog of yeast long chain polyunsaturated fatty acid elongation enzyme 2	Lipid metabolism
−2.46	4.76	LOC51601	Lipoyltransferase	Lipid metabolism
−1.10	−2.22	PAFAH2	Platelet-activating factor acetylhydrolase 2	Lipid metabolism
−1.23	2.22	PLSCR1	Phospholipid scramblase 1	Lipid metabolism
1.07	4.65	SAA1	Serum amyloid A1	Lipid metabolism
2.32	1.17	SCD	Stearoyl-CoA desaturase	Lipid metabolism
1.19	−2.19	SDR1	Short-chain dehydrogenase/reductase 1	Lipid metabolism
1.56	3.91	EDG2	Endothelial differentiation, lysophosphatidic acid G-protein-coupled receptor, 2	Receptor, G-protein-coupled
−4.01	−2.50	HMGCS1	3-Hydroxy-3-methylglutaryl-Coenzyme A synthase 1	Steroid metabolism

unsaturation of fatty acids through the introduction of double bonds between defined carbons of the acyl chain, were induced over the four-day time period. In contrast, after

an initial induction of stearoyl-CoA desaturase (SCD) at two days postwounding, expression decreased by day four. The principal product of SCD is oleic acid formed by desaturation of stearic acid. Furthermore, suppression of 3-hydroxy-3-methylglutaryl-Coenzyme A synthase 1 (HMGCS1) was found at both time points tested. This enzyme catalyzes the reaction in which Acetyl-CoA condenses with acetoacetyl-CoA to form 3-hydroxy-3-methylglutaryl-CoA (HMG-CoA), an intermediate in cholesterol synthesis, indicating deregulation of, and in this case, a decrease in cholesterol synthesis.

3.4 Discussion

In this study we observed a disordered lipid phase in the wound area and characterized its spatial and temporal evolution as healing progressed through six days in ex vivo skin wounds. Changes in lipid physical state in the vicinity of the MET have neither been observed experimentally nor discussed significantly in the literature to date. However, several biochemical lines of published work provide a useful frame of reference for interpretation of the current results. The disordered lipid phase is characterized by a factor loading whose spatial distribution of high scores tracks the areas near and within the MET reasonably well in the two to six day stages of healing. The lipid chains are conformationally more disordered than those in the SC and in the control section VE (Fig. 3-4) as characterized by symmetric CH_2 stretching frequencies at ~2854.5 cm^{-1} and asymmetric CH_2 stretching frequencies at ~2925 cm^{-1}. This conclusion is reached because of the unique ability of IR to directly image lipid conformational order.

Three IR spectral regions provide evidence for the presence and involvement of disordered, ester-containing lipids during the wound healing (Figs. 3-4, 3-5, and 3-7). Although factor analysis provides an important qualitative evaluation of spectral

differences related to composition and molecular structure, a semi quantitative assessment of the evolution of particular features is better accomplished by univariate techniques (Figs. 3-5 and 3-6). Thus, the integrated area of the CH_2 symmetric stretching mode in Figs. 3-5(a) and 3-6(b) provides direct evidence for a progressive increase in the amount of lipid within and in the vicinity of the MET as healing progresses compared to the VE in the control section. In these figures, the relatively high amount of lipid in the SC is also evident, as anticipated, and will not be considered further. Comparing Fig. 3-5(a) to the factor score images derived from the CH stretching region in Fig. 3-4, it is clear that the regions within and in the vicinity of the MET with a higher lipid content [Fig. 3-5(a)] more closely coincide with the factor score images for the "disordered," L2, lipid constituent and not L1, the ordered lipid constituent [Fig. 3-4(b)].

Gene array analysis provides some evidence for an increase in the unsaturated lipid population through the induction of the fatty acid desaturases, FADS1 and FADS3 (Table 1). Unsaturation in lipid acyl chains generally increases conformational disorder. An obvious issue to consider is the relationship of this disordered lipid to keratinocyte behavior during the re-epithelialization phase of wound healing. One possible role for the increase in disordered lipid population related to wound healing may involve the EGFR, known to activate keratinocytes upon ligand binding (Jiang, *et al*., 1993). Elevation of EGFR regulates a wide range of cellular processes that are important during wound healing, including cell adhesion, expression of matrix proteinases, and keratinocyte proliferation and migration (Hudson, *et al*., 1998; Repertinger, *et al*., 2004). Of interest in the current work is the possible role of the physical state of lipid in the receptor environment on the control of EGFR function. Several studies addressing this issue have

suggested receptor localization in lipid rafts (Pike, *et al*., 2005; Ringerike, *et al*., 2001; Lambert, *et al*., 2008; Mathay, *et al*., 2008; Balbis, *et al*., 2010), cholesterol enriched domains involved in signal transduction. Pike et al (Pike, *et al*., 2005) reported that the EGFR-enriched lipid rafts are augmented in lipid classes that differ from those identified by the classical Triton X-100 extraction procedure that first defined lipid rafts. They suggest that unlike "traditional" raft composition, EGFR-containing rafts have a lower degree of chain saturation (Pike, *et al*., 2005). This suggests that the EGFR-enriched rafts are likely to be conformationally less ordered than "traditional" rafts, and are certainly much less ordered than SC lipids. Thus, it is tempting to speculate that the disordered lipid population observed in the current experiments may participate in EGFR activation and internalization. To discern whether the increase in the disordered lipids we observe in the MET is involved in the EGFR raft environment and/or internalization will require additional study.

The observed increase in the relative amount of disordered lipids within and in the vicinity of the MET could certainly be involved in additional functions related to wound healing. Some wound healing events directly involve lipids, although the conformational state of the lipids has not been reported. These may include the active involvement of phosphatidic acid (Mazie, *et al*., 2006), phosphoinositides, or diacylglycerol (Hudson, *et al*., 1998; Lambert, *et al*., 2009) in cell signaling or an increase in triglycerides as a source of energy for cell proliferation and migration as suggested by Kozel'tsev et al. (Kozel'tsev, *et al*., 2006) Other work, including the microarray analysis herein, suggests the indirect involvement of lipids in wound healing. The induction of the endothelial differentiation, lysophosphatidic acid G-protein coupled receptor 2 (EDG2) gene (Table

1), known to mediate proliferation among other functions, implies that the presence of lysophosphatidic acid is increased. Finally, an increase in a lipid population with relatively high acyl chain conformational disorder would tend to increase lipid diffusion rates, thus providing a more fluid environment for the migration of keratinocytes.

In summary, IR imaging data detects the presence and spatial distribution of a disordered lipid phase within and in the vicinity of the MET as healing progresses (day two to six) in the current *ex vivo* wound healing sections. Several possibilities are noted above for the biological relevance of these observations. Further mechanistic insight may be gained from molecular biology approaches such as immunofluorescent staining in an attempt to specify, for example, lipid involvement with EGFR activation. The current work likely provides some hypotheses to be tested in these further studies.

Chapter 4 Vibrational spectroscopy and microscopic imaging: novel approaches for comparing barrier physical properties in native and human skin equivalents

4.1 Introduction

Human and animal skin provide important experimental substrates for research and testing applications in the biomedical, pharmacological, and cosmetic worlds, but the continuing use of these materials for testing purposes is becoming progressively constrained. Although excised human skin is ideal for such studies, ethical considerations restrict its availability. As discussed elsewhere (Netzlaff, *et al*., 2005), animal skin has, until recently, been extensively used as an alternative. Two current impediments limit the use of animal skin. From the ethical side, the 2009 EU Directive 76/768/EEC effectively eliminates animal testing in the cosmetic industry by imposing bans (a) on testing finished cosmetic products and ingredients on animals and (b) on marketing finished cosmetic products that either have been tested in animals or that contain ingredients that have been tested in animals. In addition to the ethical issues, the transferability of conclusions drawn from animal skin experiments to human skin is problematic (Bronauph, *et al*., 1982; Andega, *et al*., 2001; Bouwstra, *et al*., 1995). Given the above impediments to the usage of excised skin, in vitro models are rapidly becoming the most widely used replacements for human and animal skin testing. As such, methods characterizing their biological and physical properties must be generated and evaluated. Thus, in Article 4a of the aforementioned directive, it is noted that "Member states shall prohibit (a) the marketing of cosmetic products where the final formulation . . . has been the subject of animal testing using a method other than an alternative method after such alternative method has been validated . . ."

To begin to satisfy the EEC requirements, in vitro methods for monitoring penetration of exogenous materials into human skin equivalents (HSEs) have begun to be evaluated. To cite a single example from the many available, Wagner *et al.* (Wagner, *et al*., 2001) proposed two in vitro cutaneous test systems for determination of permeation and penetration parameters, utilizing the Franz diffusion cell for the former and the Saarbruecken permeation model for the latter. More recently, Netzlaff et al. (Netzlaff, *et al*., 2005) evaluated several models of human epidermis for morphology and for their suitability for monitoring phototoxicity, irritancy, corrosivity, and transport. These authors concluded that "the barrier function of these reconstructed human epidermis models appears to be much less developed compared to native skin".

Since the molecular structure of the barrier in reconstituted skin evidently controls its transport functions, biophysical investigations of skin molecular organization should be useful in the development of improved, targeted designs of HSEs for particular purposes. Toward this end, imaging technologies are obviously required. As noted by Brohem *et al.* (Brohem, *et al*., 2011), standard monolayer two-dimensional (2-D) cell cultures cannot duplicate the architecture of skin; the need for in vitro three-dimensional (3-D) skin models is therefore clear. Technologies providing molecular structure information are anticipated to be useful for effective comparisons between reconstituted and excised human skin.

Conventional biophysical molecular structure techniques such as x-ray diffraction and electron and related microscopies as well as optically based imaging technologies such as optical coherence tomography have been profitably applied to characterize HSEs

(Lademann, *et al*., 2005; Pierce, *et al*., 2004; Yeh, *et al*., 2004). Each approach has advantages and limitations. X-ray diffraction-based methods (Ponec, *et al*., 2001; Bouwstra, *et al*., 1995; Bouwstra, *et al*., 1996; Bouwstra, *et al*., 1995; Ponec, *et al*., 2000) are most useful for detection of well-ordered (lipid) lamellar phases, but are not well suited for disordered and otherwise unstructured (e.g., protein containing) phases. Electron microscopy-based methods offer superb spatial resolution (Ponec, *et al*., 2001; Monteiro-Riviere, *et al*., 1997), but generally require substantial specimen preparation, which may alter molecular structures. Visible and fluorescence microscopy-based approaches provide no molecular structure information.

Within the set of techniques based on optical spectroscopy/ microscopy, infrared (IR) and Raman spectroscopies provide molecular structure information for characterization of the skin permeability barrier, including details about lipid packing and chain conformational order. The elucidation of structures of lipid models for the SC has been undertaken by several groups (cited below) in addition to our own, including academic laboratories in Leiden and Halle, and industrial laboratories in Geneva and New Jersey. In models such as the standard three component (ceramide, fatty acid, cholesterol) systems, the use of chain-perdeuterated lipid species enhances the specificity of vibrational spectra, while not affecting structural parameters. Early examples of this approach were given by Naik *et al.*(Naik, *et al*., 1995), from this laboratory, and others (Moore, *et al*., 1997; Percot, *et al*., 2001; Chen, *et al*., 2001; Rerek, *et al*., 2005).

In addition to information arising from lipid molecules, vibrational spectra are sensitive to protein secondary structure. Lin *et al.*(Lin, *et al*., 1996) used the Amide I spectral

region (1615 to 1690 cm^{-1}) to track the thermally induced conversion of keratin from α to β structure in the presence and absence of permeation enhancers. We have examined the same conversion in single corneocytes (Zhang, *et al*., 2007) and have also taken advantage of this spectral region in our initial studies of wound healing (Chan, *et al*., 2008).

Technical advances over the past 15 years permit the acquisition of spatially resolved IR and Raman spectra. The techniques of IR microspectroscopic imaging and confocal Raman microscopy have both been applied to characterize skin at close to the diffraction limit in each instance. The interplay of spectral and structural information from these studies provides unique insight into tissue structures. Several studies have revealed the advantages of these approaches for studying the skin barrier. The Puppels laboratory demonstrated (Caspers, *et al*., 2001; Caspers, *et al*., 2003; Schut, *et al*., 2002; Boncheva, *et al*., 2009) the feasibility of acquiring both in vivo and in vitro Raman spectra of skin. This was followed (Caspers, *et al*., 2002) by studies by the same group tracking dimethyl sulfoxide (DMSO) permeation to a depth of ~120 μm through palmar SC and the determination of the concentration profiles of natural moisturizing factor (NMF) and water. This laboratory demonstrated (Zhang, *et al*., 2007) an extension of this method to pharmacological problems through a study of the spatial distribution of the enzymatic hydrolysis of a 5-FU prodrug to the drug itself in full-thickness excised skin. Finally, in a report relevant to the current discussion, Tfayli *et al.* (Tfayli, *et al*., 2007) correlated observed Raman frequencies with tentative band assignments for an Episkin model. This work provides a useful starting point for the Raman characterization of artificial skin. The above citations indicate that vibrational spectroscopy, microscopy, and imaging are

suitable approaches for a comparative evaluation of molecular structure and barrier properties in excised human skin versus HSEs.

The current work presents three types of IR and Raman experiments that compare barrier properties in excised skin with HSEs. First, chain packing and conformational order are compared in the isolated SC of human skin, porcine skin, and in two HSEs, Epiderm 200X with an enhanced barrier function, and Epiderm 200 with a standard barrier function, both from MatTek Corporation (Ashland, MA). Second, the formation of ordered lipid domains enriched in cholesterol is compared for excised human skin with the two HSEs. Finally, lipid barrier dimensions and the spatial disposition of the ordered lipids are compared in these samples. The current experiments are intended to begin to define a general set of vibrational spectral parameters for comparing the spatial and molecular properties of reconstituted skin models with native skin, which in turn may provide an explanation of functional differences among these preparations.

4.2 Materials and Methods

4.2.1 Materials

Porcine biopsies from Yucatan white, hairless pigs were purchased from Sinclair Research Center, Inc. (Columbia, MI). Human abdominal skin specimens were obtained from dermatological offices (otherwise to be discarded) with informed consent and in accordance with institutional protocols. HSE tissues, in particular, Epiderm 200X (EpD200X) and Epiderm 200 (EpD200), were purchased from MatTek Corporation (Ashland, MA). EpD200 is a regular HSE product with 8-12 cell layers of viable epidermis (basal, spinous, and granular layers) and 10-15 cell layers of SC. EpD200X has

the same morphological property as EpD200, but with enhanced barrier function--designed for permeability studies.

4.2.2 IR Microscopic Imaging

Skin samples preparation and IR microscopic imaging follow the protocols as introduced in Chapter 2. Two specimens of each type of HSE were microtomed and three to five images were acquired for each specimen. Images of sections of excised human skin shown herein are typical of the many (>20) specimens examined.

4.2.3 Confocal Raman Microscopy

Skin sample surfaces were cleaned several times with a cotton swab, inserted into a brass cell with the stratum corneum side up, and placed underneath a microscope coverslip that was pressed gently against the skin to ensure good optical contact. The cell-coverslip interface was sealed with clay to keep the moisture level constant. Raman spectra were acquired with a Kaiser Optical Raman microprobe (Ann Arbor, Michigan) at a spectral resolution of 4 cm^{-1}. Spectra were acquired using a 60 s single exposure time, three accumulations, and cosmic ray correction. Two specimens of each type of HSE were examined and the Raman images of excised human skin shown herein are typical of the many specimens examined as mentioned above.

4.2.4 IR Spectra in Bulk Phases

Skin was treated with 0.5% trypsin solution at the air-liquid interface for one day. The stratum corneum was then peeled off, rinsed with distilled water, and transferred to a ZnSe window. The isolation of SC samples from EpD200X required a protocol slightly

different from human and pig skin samples, since there is no apparent distinctive physical property difference between the SC and epidermal layer in the samples. These samples were thus treated in the trypsin solution for two days, at which time no additional physical change could be observed (i.e., sample thicknesses after this time remained constant), and no additional tissue could be removed from the viable epidermis side by scratching with tweezers. The isolated HSE SC was then placed on a ZnSe window. SC samples were dried under house vacuum for a day or two. A second ZnSe window was placed on top and the sample was contained in a temperature-controlled IR cell (Harrick Scientific, Ossining, New York). IR spectra of the dried SC were acquired with a Nicolet 6700 spectrometer (Thermo Electron Corporation, Madison, Wisconsin) operating with a spectral resolution of 2 cm^{-1}. Melting curves were generated from spectra acquired at temperature increments of ~3 ℃ from 20 ℃ to the highest desired value as noted in Fig. 1. Temperature was controlled using a circulating water bath and monitored with a thermocouple (Fisher Scientific Thermostat, Model 9001, Pittsburgh, Pennsylvania) embedded in the sample cell. All experiments were run in duplicate and typical data are shown.

4.2.5 Factor Analysis of IR Images

ISys software (version 3.1.1 from Malvern Instruments, UK) was used for IR and Raman spectral analysis and production of images. The mechanisms and procedure of factor analysis of IR images were introduced in Chapter 2. Three to six significant factors were observed from most data sets in this study.

4.3 Results

4.3.1 Bulk Phase IR Spectroscopy

4.3.1.1 Conformation-sensitive regions of lipid IR spectra

One obviously important criterion for evaluating the function of HSEs is the structure and persistence of a permeability barrier (Ponec, *et al.*, 2001). Traditional (macroscopic) IR is used to compare SC lipid packing and chain conformational order in isolated human SC, porcine SC, and EpD200X. Two IR spectral regions sensitive to packing and structure are used for these purposes. The methylene rocking (715 to 735 cm^{-1}) contour is exquisitely sensitive to the packing motif adopted by the chains. As shown in Fig. 4-1(a), for SC isolated from human skin at temperatures less than ~30 ℃, the rocking mode frequency splits into a well-resolved doublet with peaks near 720 and 730 cm^{-1}. The presence of the higher frequency component is reliably diagnostic for orthorhombic perpendicular subcell packing of the lipid chains (Snyder, *et al*., 1979; Snyder, *et al*., 1961). With

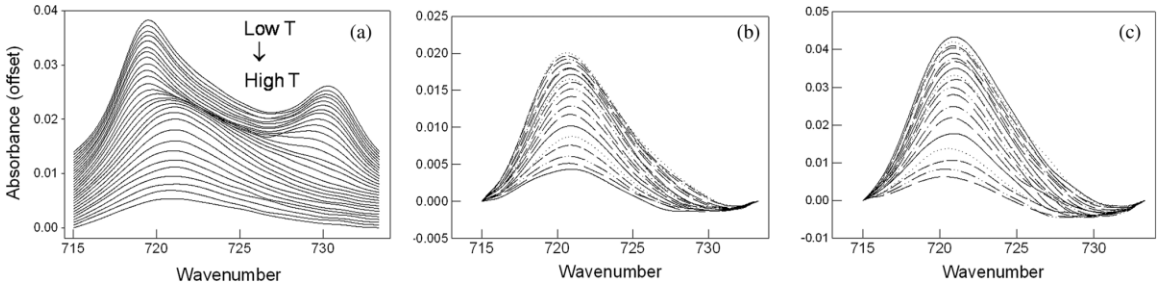

Fig. 4-1 Stacked absorbance plots of the methylene rocking region (715 to 733 cm^{-1}) from (a) isolated human stratum corneum as the temperature is progressively increased from 18 ℃ to 104 ℃ going from top to bottom; (b) isolated porcine stratum corneum spectra were acquired from 20 ℃ to 72 ℃; and (c) barrier enhanced EpD200X stratum corneum from which spectra were acquired from 20 ℃ to 72 ℃.

Increasing temperature, the doublet progressively collapses to a single peak at ~720 cm^{-1}, reflecting the disappearance of the orthorhombic packing motif and its likely replacement by hexagonal packing arrangements or (at higher temperatures) disordered chains. The progressive disappearance of the orthorhombic phase is tracked as a function of temperature in Fig. 4-2(a), in which the 730 cm^{-1} band intensity has been normalized to the skin protein Amide II mode near 1550 cm^{-1}.

In contrast to human SC, porcine SC as shown in Fig. 4-1(b) displays a somewhat asymmetric rocking mode contour with a peak at ~721 cm^{-1} and no detectable peak near

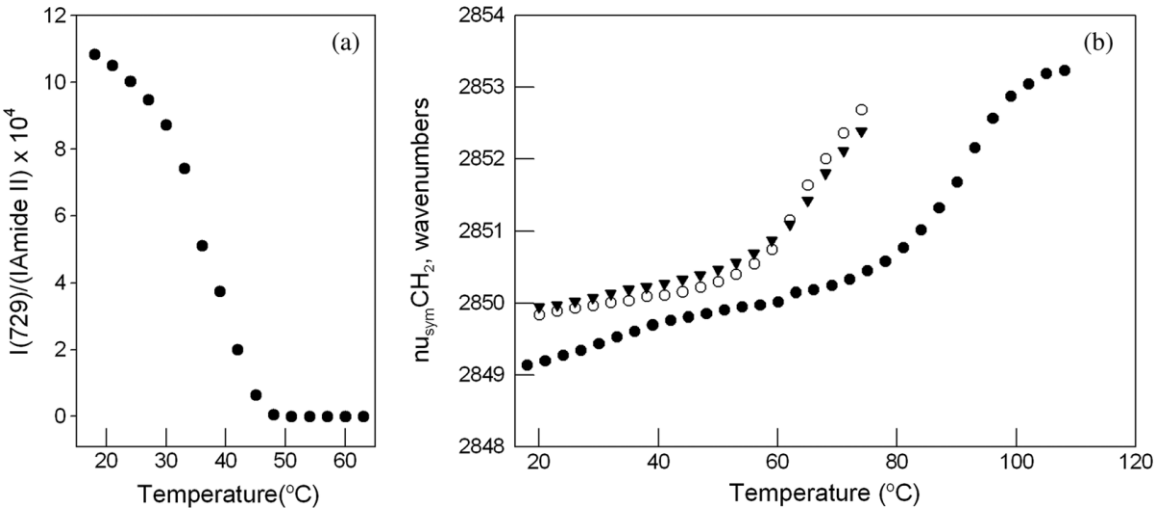

Fig. 4-2 (a) Temperature dependence of the area of the 729 cm^{-1} band arising from the orthorhombic phase in human SC as the temperature was increased as shown. The band intensity was normalized to the intensity of the Amide II mode in the spectrum. (b) Temperature dependence of the CH_2 symmetric stretching frequency for human SC (•), EpD200X SC (○), and porcine SC (▾).

730 cm^{-1} (although the asymmetry may hint at the presence of a weak feature there at the very lowest temperatures). According to the correlations discussed above, the concentration of orthorhombically packed lipids in this tissue is diminished compared to

human SC. Although the absence of an orthorhombic phase is not necessarily indicative of a substantially impaired barrier, certain functional assays in porcine skin indeed suggest a less efficient barrier than in human SC (Bronaugh, *et al*., 1982; Andega, *et al*., 2001; Bouwstra, *et al*., 1995). Results similar to porcine skin are noted [Fig. 4-1(c)] for EpD200X, including a slight inflection near 730 cm^{-1} in the lowest temperature spectrum again, possibly hinting at the presence of a very small proportion of orthorhombically packed structures.

The methylene symmetric ($\upsilon_{sym}CH_2$, 2845 to 2855 cm^{-1}) and asymmetric ($\upsilon_{asym}CH_2$, 2914 to 2928 cm^{-1}) stretching bands have also proven useful for characterization of lipid assemblies. As is well known (Mendelsohn, *et al*., 1986), the frequencies of these modes are sensitive primarily to changes in chain intramolecular conformational order (trans-gauche isomerization). As an example of the utility of this spectral region, the temperature dependence of $\upsilon_{sym}CH_2$ is plotted in Fig. 4-2(b) for SC isolated from human excised skin, porcine SC, and EpD200X. Two transitions are evident for the human SC sample. The hexagonal → disordered (L_α) transition beginning at 70 ℃ and terminating at ~95 ℃ to 100 ℃ is accompanied by a frequency increase of 3.4 cm^{-1}, from ~2850 to 2853.4 cm^{-1}. This increase defines the progressive formation of a highly disordered lipid structure, with a final frequency similar to that observed in L_α phase of phospholipids (Mendelsohn, *et. al.*, 1986). The second broad transition from ~20 ℃ to 40 ℃, detected by a significantly smaller frequency increase from ~2849.2 to 2849.7 cm^{-1}, reflects the orthorhombic to hexagonal packing transition previously detailed from the rocking mode contour in Figs. 4-1(a) and 4-2(a). This small increase indicates that the chains remain conformationally ordered in both phases.

The situation is markedly different for the porcine SC and EpD200X samples compared to human SC. For the porcine and HSE samples, the main lipid order → disorder transition is noted [Fig. 4-2(b)] at much lower temperatures (~50 ℃ to 70 ℃) than in human SC. The lipid phase at low temperatures in porcine and in EpD200X SC is characterized by conformationally ordered chains but also by the absence of significant levels of orthorhombic subcell packing. While there is no direct IR marker for hexagonally packed phases in the SC, the transitions noted above are consistent with their occurrence. From a functional viewpoint, the permeability barriers presented by orthorhombic versus hexagonally packed phases are likely to be quite different. Orthorhombic phases are characterized by rigid chains locked into a highly ordered packing motif while hexagonal phases are suggested from NMR studies (Langen, *et al*., 2000) of polyethylene to undergo rapid rotational motion about their long axes. One might anticipate that the barrier to permeability is enhanced in lipid lamellae containing orthorhombic phases, if all other factors are assumed equal. However, as shown by Ponec *et al.* (Ponec, *et al*., 2001), other factors (e.g., lipid composition) evidently play a role in barrier properties. It is nevertheless clear that the IR parameters described above provide a useful biophysical characterization of lipid packing and structure within the skin barrier.

4.3.2 Confocal Raman Microscopic Determination of Skin Properties

To supplement skin barrier packing information, evaluation of spatial heterogeneity in lipid composition or chain order is possible via an approach whereby spatially resolved structural information may be generated. We illustrate the utility of confocal Raman microscopy to address this issue. As noted earlier, confocal Raman microscopy permits

acquisition of spectra with a spatial resolution of 1 ~ 2 μm in the lateral dimension and 3 μm in the direction perpendicular to the SC surface. An inherent experimental problem with this technology is the single-beam nature of the experiment. When carried out in an

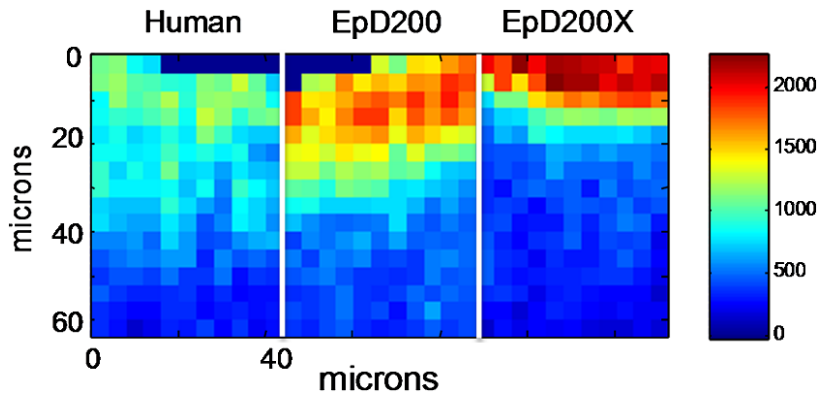

Fig. 4-3 Development of a Raman intensity standard. The area of the 1004 cm^{-1} band arising from the ring breathing mode of protein Phe residues is plotted as a function of position for samples of full thickness excised human skin, EpD200, and EpD200X. Spectra were acquired over a 2-D image plane every 4 μm to a depth of 60 μm as shown. The vertical scale bar is color coded for values of Raman scattering intensity as shown on the right hand panel.

environment such as skin in which the refractive index changes unpredictably, relative concentration information cannot be directly inferred from peak intensities. The measured intensities must be corrected for scattering efficiency changes as the excitation source samples sites at increasing depths within the tissue. Our approach to this problem (Fig. 4-3) is based on the observation that in skin samples studied to date, the intensity of the Phe ring stretching vibration at 1004 cm^{-1} decays mostly monotonically with depth from the skin surface. The assumption required to utilize the 1004 cm^{-1} to normalize the scattering intensities is that the concentration of Phe residues from skin proteins is constant with depth.

With this assumption, the diminution in 1004 cm^{-1} peak intensity as the excitation laser is focused progressively deeper in the tissue is presumed to arise completely from scattering losses (i.e., the inability of Raman photons from deep in the tissue to reach the detector) rather than concentration variations. The type of data acquired routinely is shown in Fig. 4-3 for full-thickness excised human skin, EpD200, and barrier enhanced EpD200X, respectively. The intensity of the 1004 cm^{-1} band as a function of depth shows similar trends in each case, i.e., diminution with depth is more or less monotonic, but the magnitude of the effect varies from sample to sample. The vertical depth to which the variation in scattering intensity is considered reasonable (i.e., is not affected greatly by

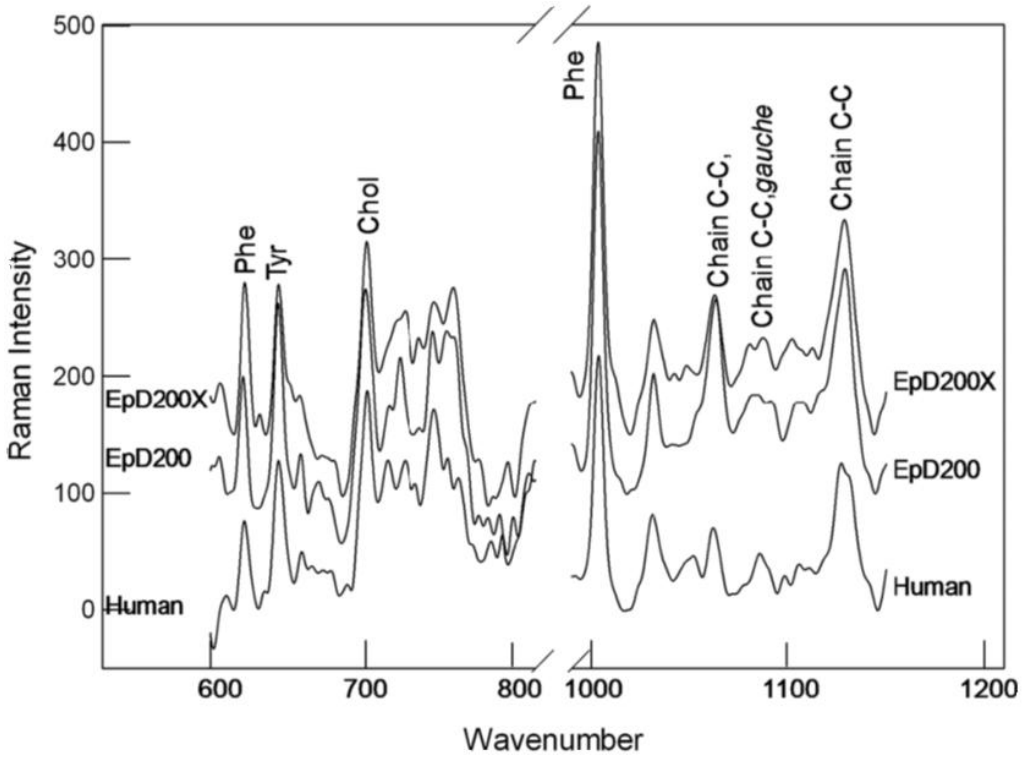

Fig. 4-4 Raman spectral data from the SC of the samples indicated. Some assignments of the various spectral features are given. The intensities in the 600 to 810 cm^{-1} region have been multiplied by a factor of 3 compared to those in the 990 to 1150 cm^{-1} region.

noise) occurs at a depth of 50 μm for human skin and EpD200 and 40 μm for the EpD200X sample. We assume the more conservative (latter) value for the following.

The utility of confocal Raman microscopy for characterizing lipid domains in skin is depicted in Figs. 4-4 and 4-5. Typical spectra collected from the SC of excised human skin, EpD200, and EpD200x over the range 580 to 810 and 990 to 1150 cm^{-1} are shown in Fig. 4-4. Features of interest are (1) the 701 cm^{-1} band arising from cholesterol (Zhang, *et al.*, 2007), (2) the 1004 cm^{-1} Phe band discussed previously, and (3) two chain C─C stretching modes near 1063 and 1130 cm^{-1} whose origins (Snyder, *et al.*, 1967) are as follows: The 1000 to 1150 cm^{-1} region contains skeletal vibrations in which alternate

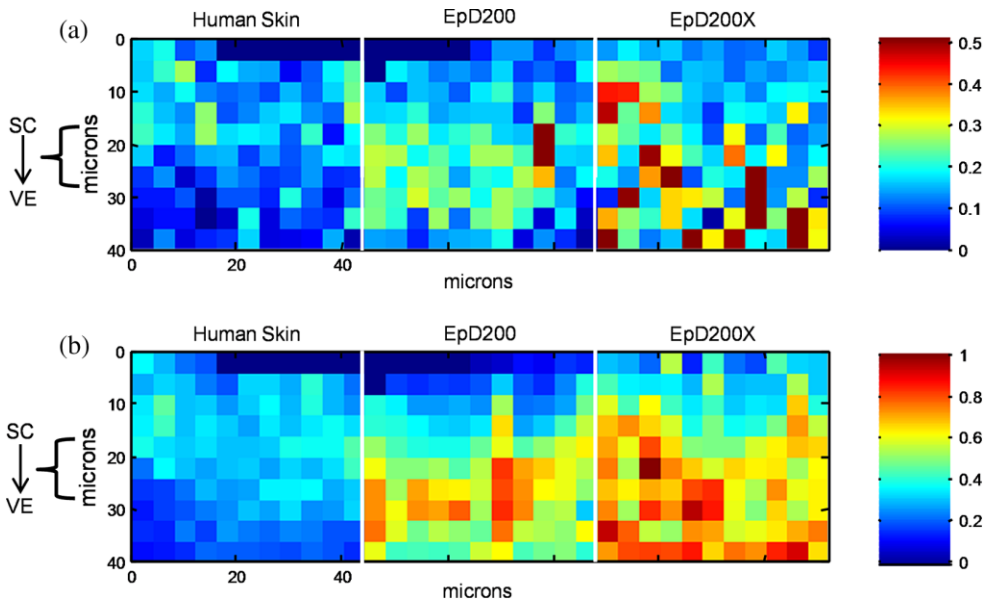

Fig. 4-5 (a) Spatial distribution of the area ratio of the 701⁄1004 cm^{-1} bands for samples of full-thickness excised human skin, EpD200, and EpD200X as marked. This ratio provides a measure of the occurrence of lipid pockets enriched in cholesterol. See text for details. (b) Spatial distribution of the area ratio of the 1063⁄1004 cm^{-1} bands for samples of human skin, EpD200, and EpD200X as shown. This ratio provides a measure of the occurrence of ordered lipid phases, since the 1063 cm^{-1} band arises from a particular vibration of all-trans lipid chains.

carbon atoms move in opposite directions. These "skeletal optical modes" appear in ordered lipid phases as strong features from the k = 0 modes of an all-trans chain at 1130 cm^{-1} (A_g symmetry in polyethylene) and 1060 cm^{-1} (B_{1g} symmetry in polyethylene). In disordered phases a feature arises at 1080 to 1100 cm^{-1} from uncoupled C─C stretching vibrations in chain segments containing gauche rotations. These features are labeled in Fig. 4-4.

From the measured band intensities, interesting structural information may be inferred. Thus, the peak height ratio 701⁄1004 cm^{-1} is used to monitor cholesterol-enriched domains in the epidermis. This parameter is imaged to a depth of 40 μm in Fig. 4-5(a) for excised full-thickness human skin, EpD200, and EpD200X. Substantial variations in the distribution of cholesterol-enriched lipid domains are noted between these materials and reveal the presence of many more cholesterol-enriched lipid pockets in the EpD200X samples. In contrast, excised human skin shows lower relative cholesterol levels generally and many fewer pockets. EpD200 reveals intermediate levels of these structural elements. We note that the delineation of the SC and viable epidermis (VE) boundary as shown in Fig. 4-5(a) pertains primarily to human skin. These two regions of the tissue are difficult to distinguish spectroscopically in the HSEs.

Further insight into domain formation is evident from plots in Fig. 4-5(b) of the 1063⁄1004 cm^{-1} peak intensity ratios. Significant differences are again observed in this parameter between the samples. Pockets of a relatively higher concentration of conformationally ordered lipid are observed between depths of 15 and 40 μm for the EpD200X and between 20 and 35 μm for the EpD200. In contrast, the confocal Raman

image of full thickness excised human skin shows less variability in the concentration range of ordered lipid, with the higher concentrations appearing throughout the SC. Quantitatively, the level of ordered lipids in the HSE pockets is approximately twice that observed in the human SC. From this experiment, the Raman imaging approach is shown to provide unique information about cholesterol-enriched pockets and the distribution of conformationally ordered lipid in both SC and epidermal regions.

4.3.2.1 Comparative IR microscopic imaging of excised human skin and Epiderm 200X

Compared with confocal Raman measurements, IR imaging permits convenient sampling of substantially larger areas, up to several mm^2. This gain is partly offset due to worse spatial resolution at the longer wavelengths involved in the IR measurement compared with Raman microscopy. A disadvantage of IR is that confocal measurements are not easy due to the transmission based nature of the measurement. Confocal image plane masking and complicated instrumentation are needed for the confocal measurement (Wetzel, *et al*., 2011; Murdoc, *et al*., 2010). On the positive side, spectral S⁄N ratios are significantly higher in the IR compared with the Raman measurement.

The utility of IR imaging for comparison of full-thickness excised human skin with HSE is shown in Figs. 4-6 and 4-7 in which the results of factor analysis for EpD200X and human skin are depicted for two spectral regions, namely the C─H stretching region (2800 to 3000 cm^{-1}) in Fig. 4-6, and the 1180 to 1480 cm^{-1} region in Fig. 4-7. Primary IR spectral data from these samples were concatenated prior to the application of factor analysis. Six significant factor loadings (labeled F1 to F6 in the right panel of each figure)

were observed in each spectral region. The score plots derived from each are labeled F1 to F6 on the left side of the left hand figure in each instance. In Fig. 4-6, the spectral-like features depicted in the loadings are assigned as follows: ~2850 and ~2920 cm^{-1}, lipid methylene symmetric and asymmetric stretching modes; ~2873 cm^{-1}, protein symmetric CH_3 stretching.

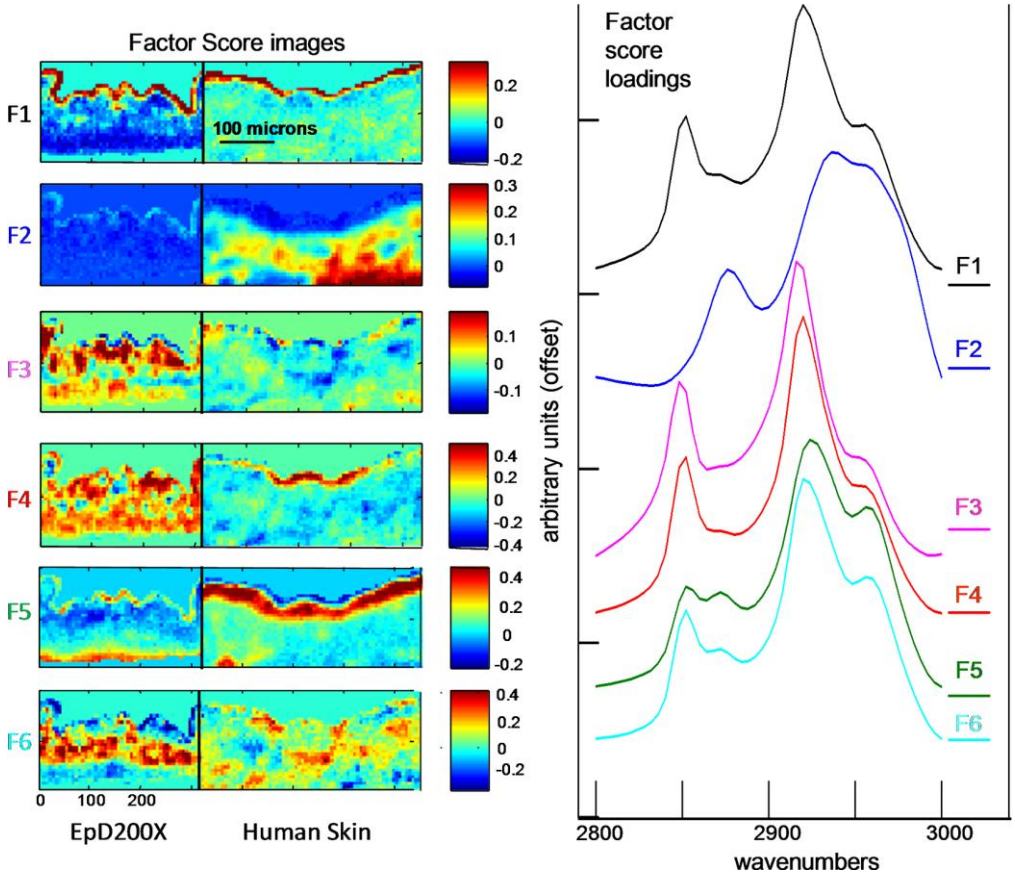

Fig. 4-6 Factor loadings and score images for the C─H stretching region (2800 to 3000 cm^{-1}) of full-thickness excised human skin sample and EpD200X. The original IR imaging data were concatenated and factor analysis was then undertaken. Six significant loadings labeled F1 to F6 were extracted from the data and are depicted (overlaid) in the right hand panel. The scores from each loading are plotted in the left hand panel as labeled for both human skin and the HSE.

As in the confocal Raman images, the main value of IR imaging arises because the spatial distribution of the chemical and structural information inherent in the spectra are exposed.

As such, factor loadings can be used to identify the main chemical contributors to the variance at particular regions in the score plots of particular factors. The color coding schemes in Figs. 4-6 and 4-7 are used to define the relative contribution of each factor to a particular pixel in each plot. These are in the progressively diminishing sequence red > orange > yellow > green > blue > purple depicted in the color bars adjacent to each image. We now consider the structural ramifications of the variances detected.

The factor F1 in Fig. 4-6 depicts a reasonably ordered lipid population ($\upsilon_{sym}CH_2$ = 2851.7 cm^{-1}) with very little protein, as deduced from the low IR intensity of protein methyl stretching modes. The vertical dimension of the SC layer in the F1 factor score image perpendicular to the skin surface in each tissue is ~3 pixels (~20 μm), and corresponds to the anticipated thickness of this layer.

Factor loading F2 (Fig. 6), with high scores in human skin and no counterpart in EpD200X, arises from a protein-rich loading with little detectable lipid as deduced from the absence of a lipid feature near 2850 cm^{-1} and the presence of an intense feature at 2877 cm^{-1}. The protein is readily identified as collagen both from the characteristic shape of its Amide I contour (Chan, *et al*., 2008) (spectral data not shown here) and from the presence of the 1338 cm^{-1} band characteristic (Belbachir, *et al*., 2009) of collagen 4-hydroxyproline (hyp) residues shown in factor loadings F3 and F4 (human skin) in Fig. 4-7. In this instance, the molecular structure information in the loading (F3 in Fig. 4-7) and the similarity in the score plots between F2 in Fig. 4-6 and F3 in Fig. 4-7 confirm the

imaged species as collagen, mostly in the dermal region. Since EpD200X is created from keratinocytes, no collagen is anticipated in this HSE.

Two additional factors in Fig. 4-6, F3 and F4, depict conformationally ordered lipid chains with methylene frequencies of 2849.2 and 2851.2, respectively. These lipids are spatially distributed in the viable epidermal (VE) region of EpD200X, which is not normally considered to possess major barrier functions. No counterparts (with similar score images) are observed for the human skin. The spatial distribution of high scores for

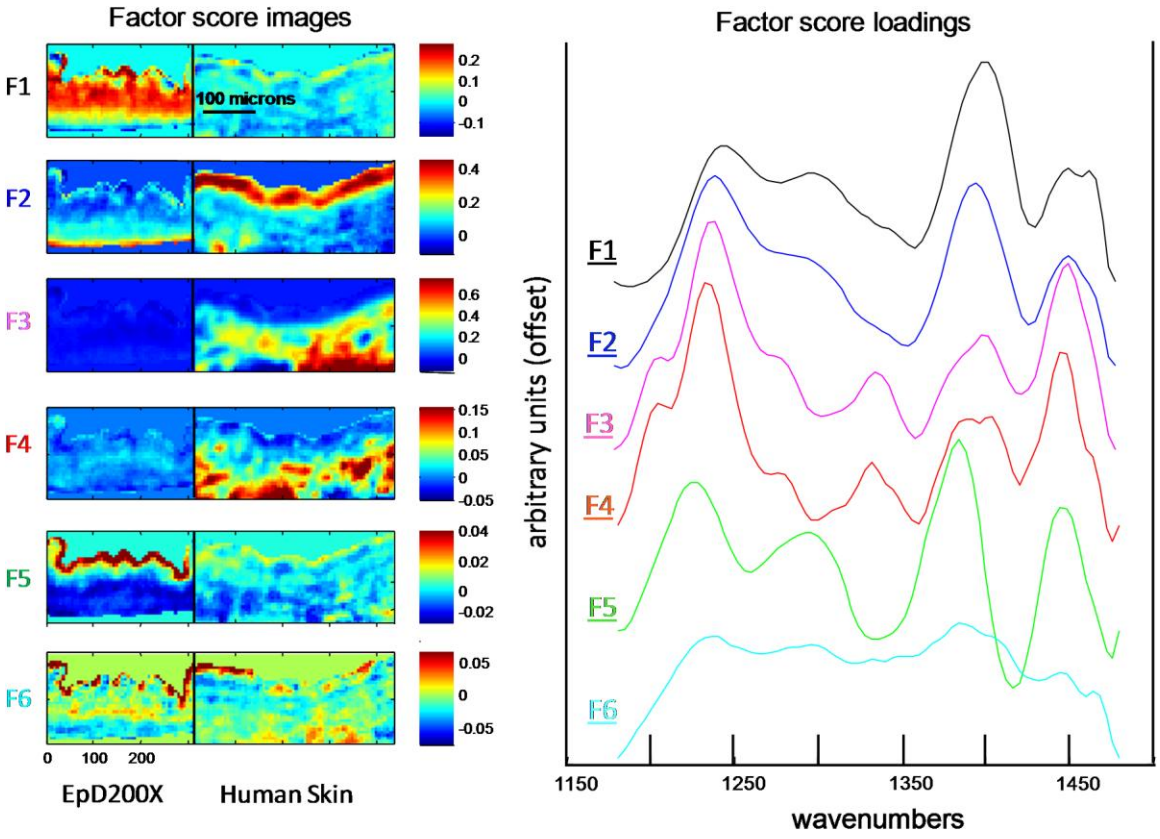

Fig. 4-7 Factor loadings and score images for the 1180 to 1480 cm^{-1} region of full-thickness excised human skin and EpD200X. The same data set was used as in Fig. 6. Six significant loadings labeled F1 to F6 were extracted from the data and are depicted (overlaid) in the right hand panel. The scores from each loading are plotted in the left hand panel as labeled for both human skin and the HSE.

F3 and F4 in the upper VE of EpD200X is consistent with the confocal Raman image [Fig. 4-5(b), right] of the relative concentration of ordered lipid (1063/1004 cm^{-1} peak intensity ratio).

In addition, a substantially disordered lipid population characterized by the factor loading F6 in Fig. 4-6 with a methylene symmetric stretching frequency of 2855.8 cm^{-1} is evident mostly in the lower region of the viable epidermis for both EpD200X and in the dermal and VE regions of human skin. The structural significance of this lipid is unclear, but presumably it is not likely to be involved in barrier functions. Finally, we note the presence of very similar factor scores from F5 in Fig. 4-6 and F2 in Fig. 4-7, with suggestive spatial distributions. In human skin, the loading is concentrated in the VE. Examination of the C─H spectral region (F5 in Fig. 4-6), indicates a mixture of lipid and protein content as shown by the presence of both 2850 and 2875 cm^{-1} spectral features, while the loading in the 1180 to 1475 cm^{-1} region (F2 in Fig. 4-7) shows no 1338 cm^{-1} feature, indicating the absence of collagen. The major protein contributor to the variance is thus identified as keratin. The complement to this in the HSE section appears to be present in factors F1 and F5 in Fig. 4-7, again with the absence of the collagen 1338 cm^{-1} band and the spatial distribution of high scores located in keratin-rich areas. Our prior studies of wound healing (Chan, *et al*., 2008) suggest that this spectral region, in particular the intensity distribution in Amide III components, may be sensitive to different keratin types. In the HSE, the molecular origin of the high factor scores observed in the ~10-micron-thick region at the bottom of F5 in Fig. 4-6 and F2 in Fig. 4-7 is undetermined.

A drawback with factor analysis is the lack of a straightforward relationship between the intensity of a factor loading in a score image and the concentration of chemical constituents of the skin in the particular pixels of interest. Simple univariate analysis can overcome this issue as shown in Fig. 4-8 in which the spatial distribution of the lipid/protein ratio is presented as the 2852⁄2872 cm^{-1} peak height ratio. In excised human skin, the lipid content is maximized in the thin layer (~20 μm) corresponding to the SC, while in the EpD200X, the lipid layer is 70 to 100 μm thick and encompasses the entire epidermal layer.

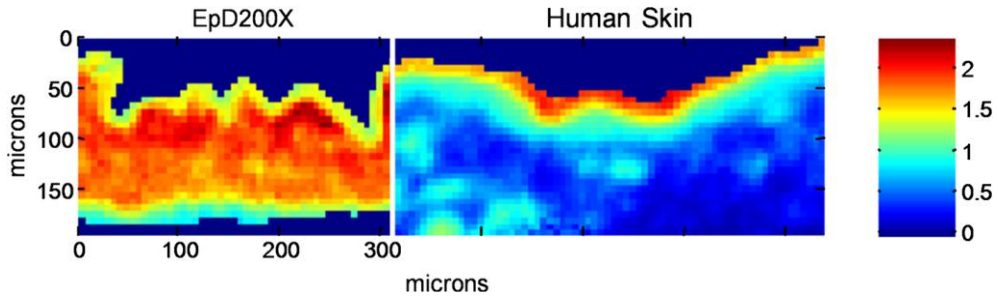

Fig. 4-8 Examination of the location of excess lipid in the barrier enhanced EpD200X and in excised human skin using a simple univariate measure. The intensity ratio (IR) (2852⁄2873 cm^{-1}) is imaged with color coding as shown on the right hand panel. The parameter tracks the lipid/protein ratio in the 2-D image plane.

The power and detail available from IR imaging for the characterization of HSEs is evident from these figures. The "lipid enhanced" EpD200X reveals substantial extra lipid (shown in factors F3 and F4 in Fig. 4-6, and in the univariate image in Fig. 4-8) located in all epidermal layers in addition to the anticipated ordered lipid layer of the SC (F1 in Fig. 4-6). However, the relevance of the expanded spatial distribution of ordered lipid in HSE to barrier function is an interesting, albeit currently unresolved, issue.

4.4 Discussion

4.4.1 Macroscopic IR Experiments

As is evident from Figs. 4-1 and 4-2, various spectral regions have sensitivities to different elements of molecular structure and organization. Thus, orthorhombic chain packing motifs are easily identified from the IR methylene rocking contours in Fig. 4-1. In applications from this laboratory utilizing this spectral parameter, we have tracked the kinetics of orthorhombic phase reformation following thermal perturbation in both isolated SC (Pensack, *et al*., 2006) and in three-component SC model systems (Moore, *et al*., 2006). Boncheva et al. have used similar spectral parameters with ATR-IR spectroscopic sampling in vitro to acquire thermotropic information from the SC in full thickness skin (Boncheva, *et al*., 2008).

The reliability of these IR spectra-structure correlations is established from comparison of our detection of orthorhombic phases in the SC with the x-ray diffraction study of Ponec *et al.* (Ponec, *et al*., 2001), who observed orthorhombic phases in native (human) SC at 30 ℃ that disappeared by 45 ℃, consistent with our measurements on isolated human SC (Fig. 1). In addition, they obtained wide-angle and electron diffraction results consistent with chain hexagonal packing in reconstructed tissues. The latter observation is consistent with our observations in HSE of minimal orthorhombic structure. Thus the spectra-structure correlations utilized here are not only consistent with a myriad of prior IR studies on simpler samples such as alkanes or phospholipids but agree with the Bouwstra lab x-ray studies of samples possessing full biological complexity.

4.4.2 Vibrational Imaging

Confocal Raman microscopy offers the significant advantages over other imaging approaches in that neither probe molecules nor substantial sample preparation is required. Either full-thickness skin or skin from which the dermal layer has been trimmed are each fully suitable. Confocal measurements may be acquired to a depth of 80 μm with a "Z" resolution of ~2 to 3 μm. In contrast, IR absorption measurements preclude confocal applications and require skin samples that have been microtomed to the appropriate thickness. However, IR imaging provides some advantages for comparative characterization of skin sections. First, samples may be examined to any desired depth. As shown in Figs. 4-6 and 4-7, the conformational order of the SC lipids and disorder of the dermal lipids and the presence of collagen are easily detected. Also, as demonstrated in our initial studies of a healing wound (Chan, *et al*., 2008), the spatial distribution and activation of various keratin types is suggested from their distinctive characteristic spectral contours in the 1175 to 1450 cm^{-1} region.

4.4.3 Vibrational Spectroscopy and Imaging as a Probe of HSE Structure

To date, the type of structural information available from various physical measurements on HSEs have been elegantly demonstrated in several studies by the Leiden group who used a combination of histology, electron microscopy, and small angle x-ray diffraction. For example, in their relatively early study (Ponec, *et al*., 2001) of "human epidermis reconstructed on de-epidermized dermis," they observed, among other features of interest, formation of lamellar bodies, extrusion of same at the stratum granulosum/ SC interface and the presence of well-ordered lamellar lipid phases, with the SC lipids predominantly

in a hexagonal sublattice. In a second investigation (Ponec, *et al*., 2000), tissue architecture and quality of the permeability barrier were tracked in commercially available reconstructed human skin models and compared to human tissue. The same laboratory has more recently compared (Bouwstra, *et al*., 2008) water distribution and NMF content in HSEs and human skin and showed that the SC water level in HSEs is regulated by factors in addition to NMF. This study is relevant to issues such as desquamation, a process controlled by enzymes dependent on pH and water levels.

The above well-designed investigations provide a useful basis for comparison of native tissue with HSEs. The vibrational spectroscopy and imaging approaches described in the current work provide additional useful elements of molecular structure information. Thus, it is not possible from electron microscope (EM) or from imaging experiments with probe molecules to detect particular protein structures or alterations in same, to characterize the spatial distribution of disordered lipid phases, nor to elucidate the presence of cholesterol-containing domains. Finally, this laboratory has recently demonstrated that IR imaging, in which Beer's law is obeyed, permits the estimation of the spatial distribution of the absolute concentration of exogenous materials in skin (Mao, *et al*., 2012).

In addition to the evaluation of endogenous skin constituents, IR and Raman imaging experiments permit characterization of perturbations in molecular structure induced by exogenous substances. Should drugs, permeation enhancers, or other exogenous skin additives alter the physical properties of the endogenous skin components, the inherent ability of IR and Raman spectroscopies to track molecular structure changes in response to the presence of exogenous substance confers unique advantages.

In the current proof-of-principle application, the lipid packing and chain conformational order differences observed between the isolated SC of human, porcine, and EpD200X, revealed in Figs. 4-1 and 4-2, provide a useful means to compare and contrast packing motifs in various samples. In addition, the confocal Raman data in Figs. 4-4 and 4-5 reveal the presence of extensive cholesterol containing domains in the barrier-enhanced HSE compared to excised human skin. Finally, we learned from IR imaging (Figs. 4-6 and 4-7) that the spatial location of the enhanced lipid population in EpD200X was found to be throughout the epidermal region, leaving its relevance to skin barrier function unclear. As the level of structural information that can be acquired from vibrational imaging experiments develops, these measurements should generally provide a useful guide to the relationships between barrier structure and function within HSEs.

Although the use of IR and Raman imaging technologies to characterize reconstituted skin barriers are limited to date, there are studies in the literature suggesting that these approaches ought to be of general utility. For example, Bommannan *et al.* (Bommannan, *et al*., 1990) utilized nonimaging ATR-IR in combination with tape stripping to evaluate the disorder of the SC intercellular lipids as a function of depth. In another application, the Puppels lab has applied Raman microscopy toward the same end (Caspers, *et al*., 2003). These structural parameters may obviously define sample-to-sample differences in barrier function and are easily detected with current instrumentation. The current work along with the aforementioned studies demonstrates that extension of these types of measurements to HSEs is quite feasible.

4.5 Characterization of Lipid Distribution in a Modified MatTek HSE

As an example of the power of the current technology to track modification in HSE structure, a group of lipid-deprived HSE samples were treated with an inhibitor which inhibits the synthesis of lipid in skin. The inhibitor was dissolved in a delivery vehicle, topically applied to commercial HSE samples and cultured for a few more days. As a control, another group of lipid deprived HSE samples treated with delivery vehicle only were also cultured under the same conditions. Both groups were harvested after culture and analyzed with IR imaging. The same protocols were followed as mentioned previously.

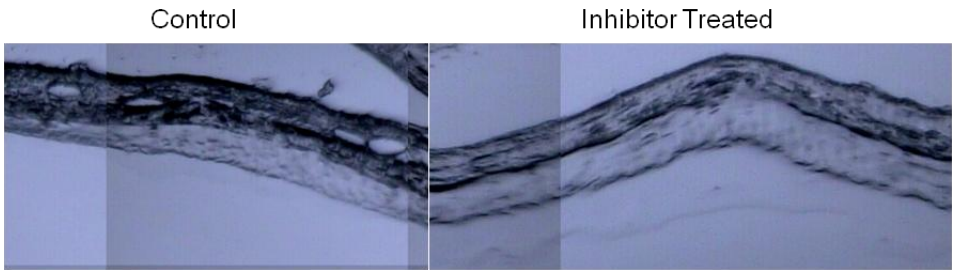

Fig. 4-9. Visible image of two samples: lipid deprived HSE samples treated with delivery vehicle only (left); lipid deprived HSE samples treated with delivery vehicle and inhibitor (right).

Two representative section samples (Fig. 4-9) are analyzed here. As the inhibitor was anticipated to alter lipid synthesis in skin, the wavenumber region 2800-3000 cm^{-1} was studied (Fig. 4-10). Three distinct different factors are generated. F1 is a typical factor for a structure with high lipid content. As can be seen in the factor score image, the high score of F1 can only be observed in the upper layer of the control sample; this high score part corresponds to the darker shaded part of the visible image, where the SC layer exists.

In the inhibitor treated sample, F1 is also relatively stronger in the SC, however, at a much lower concentration. F2 depicts mostly protein content, which is representative for epidermis. In the factor score image, F2 has a high concentration in the epidermis of the control; however it is evenly distributed between the SC and the epidermis in the inhibitor treated sample. F3 shows an even distribution in both samples and there is no obvious rationale for differences in the strength of this score between the samples.

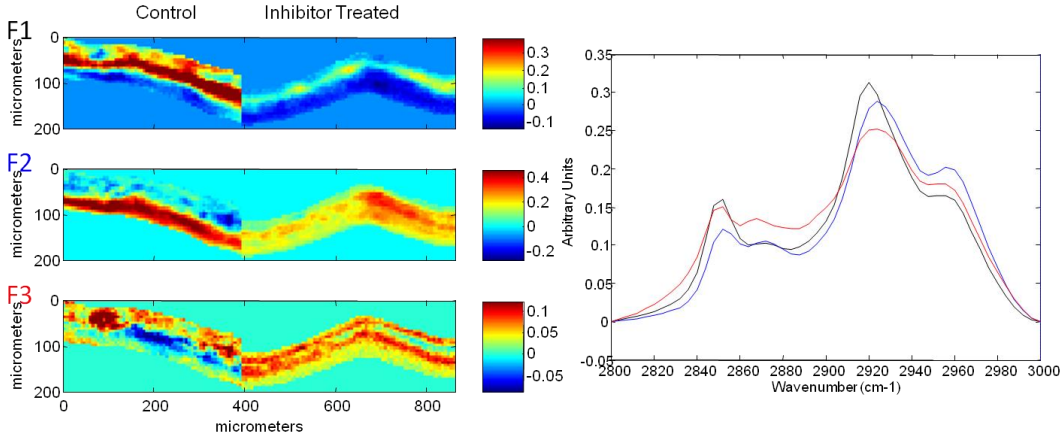

Fig. 4-10. Factor analysis of wavenumber 2800-3000 cm^{-1} region: F1, factor shows high lipid content, strong in SC layer of control, weak in the inhibitor treated one; F2, factor shows protein content, representative for epidermis, strong in the epidermal layer in control, evenly distributed in the inhibitor treated one; F3, factor shows protein content, evenly distributed in both samples.

The factor analysis above gives a good hint for further data analysis: there is a different lipid distribution between these two samples. Simple univariate analysis was conducted to provide a semi quantitative study of lipid distribution. As shown in Fig. 4-11, the peak height ratio of 2852/2872 cm^{-1} (lipid/protein) reveals a distinct lipid content difference in these two samples as was noted previously in the factor analysis. The high score pixels

still mainly reside in the SC layer of the control, even the epidermis layer of the control has a score level close to the SC layer of the inhibitor treated sample. The statistics of

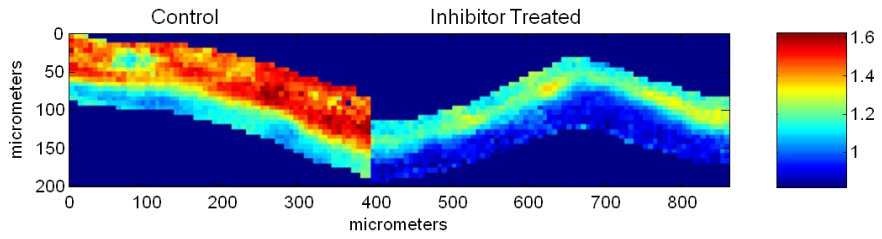

Fig. 4-11 Peak height ratio of 2852/2872 cm^{-1}, an indicator of lipid/protein ratio. Higher lipid content was observed in control sample, the ratio is higher in the SC layer in both samples.

Fig. 4-11 presented in Fig. 4-12 reveal more information concerning the peak height ratio score in both samples (Fig. 4-11). Three groups of scores are observed in the image and these different groups correspond to different layers of these two samples. The highest

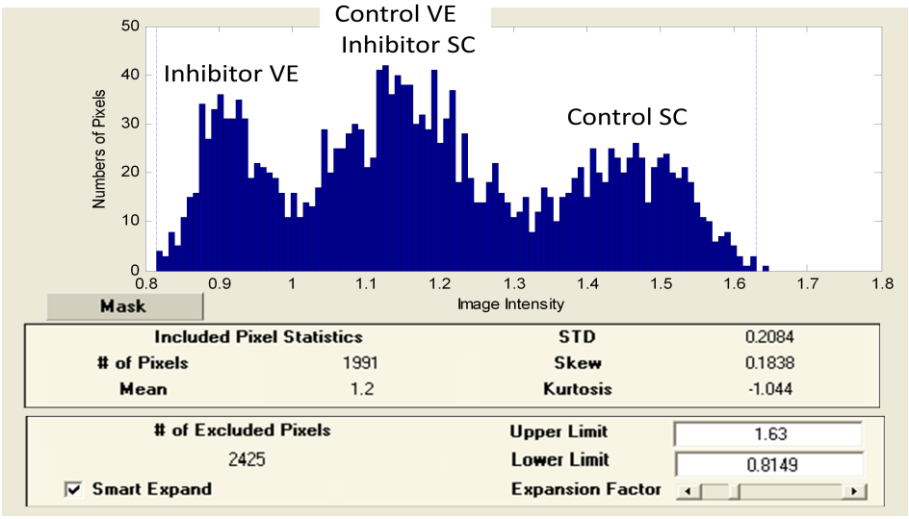

Fig. 4-12 Statistics of (Figure 4-11) Peak height ratio of 2852/2872 cm^{-1} (lipid/protein)

scores with an average of ~1.4 reside in the SC of the control, the middle scores around 1.1 correspond to the epidermis layer of the control and SC layer of the inhibitor treated sample, the lowest scores around 0.9 exist mainly in the epidermis layer of inhibitor treated sample. A peak area ratio of these two peaks (2852 cm^{-1} (2844-2864 cm^{-1})/2872cm^{-1} (2864-2884 cm^{-1})) as shown in Fig. 4-13 also shows results similar to those form the peak height ratio (Fig. 4-11). The statistics of this score image has the same

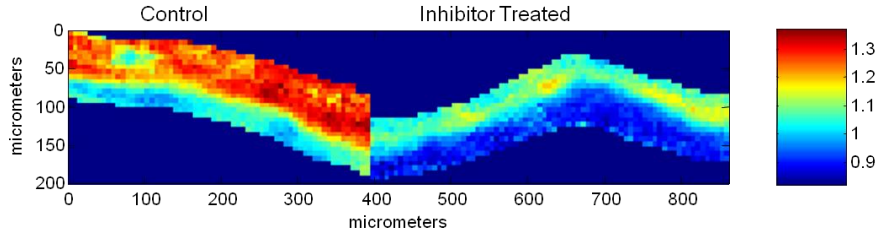

Fig. 4-13 Peak area ratio of peak 2852 cm^{-1} (2844-2864 cm^{-1})/2872 cm^{-1} (2864-2884 cm^{-1}), another way to show the ratio of lipid/protein in HSE samples.

pattern as shown in Fig. 4-12. A spectral moments image shows the center of mass for peak 2852 cm^{-1} (2836-2860 cm^{-1}) was also generated (Fig. 4-14) to study the peak's frequency difference in these two samples. Both layers of the control have lower frequencies compared to corresponding part of the inhibitor treated sample.

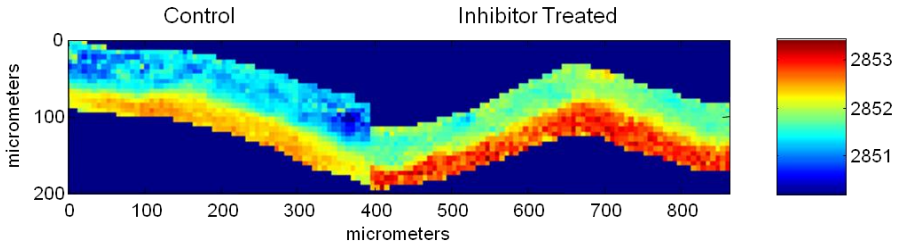

Figure 4-14 Spectral moments: Center of mass image of peak in 2836-2860 cm^{-1}.

4.5.1 Discussion

The current IR imaging study reveals the lipid content and distribution in the HSE samples treated to modify the lipid composition. Compared to the control sample treated with delivery vehicle only, a relatively lower lipid content in both the SC and epidermis layers of the inhibitor treated samples was observed, this effect probably results from the presence of the inhibitor: the synthesis of lipid was stopped or delayed in the HSE sample. The spectral moments study shows a less ordered lipid organization in the inhibitor treated samples. The biological cause of these effects needs further elucidation, but the IR imaging analysis provides a useful indicator of possible future research directions.

4.6 Conclusions

In view of the constraints noted in Sec. 1 limiting the use of animal and human skin and therefore demonstrating the necessity to utilize reconstituted constructs, vibrational spectroscopy and microscopic imaging provide a useful set of molecular structure-based parameters for exploring differences between human skin and HSEs. Future studies will center around evaluation of a statistically significant set of HSEs. One goal of such studies will be to generate correlations between physical properties of the barrier deduced from vibrational imaging and biological functions of the barrier. The effect of drugs and other factors on the structural and functional change of HSEs can also be studied with this non-invasive method.

Chapter 5 Infrared microscopic imaging study of protein glycation in diabetic foot ulcer wound healing

5.1 Introduction

Foot ulcer is a major complication developed with a risk of 12-25% in diabetic patients. Due to their special pathological conditions, the healing of diabetic foot ulcers (DFUs) is compromised and delayed, sometimes they even cause amputation: 84% of diabetic-related leg amputations are caused by DFUs (Leung, *et al.*, 2007).

The normal wound healing process is a well-orchestrated process includes three sequential, overlapping phases: inflammation, new tissue formation and remodeling. For the healing of DFUs, several biological mechanisms relevant to this process are impaired by ischemia, neuropathy, infection, increased protease, lack of protease inhibitors, deficiencies in cytokine and growth factors, *etc.* (Bennett, *et al.*, 2003; Brem, *et al.*, 2000; Brem, *et al.*, 2007; Luo, *et al.*, 2011). All these impairments delay the healing process: the inflammatory phase is prolonged, morphology of fibroblasts changed, angiogenesis is delayed, and keratinocytes appear to stop proliferating and differentiating.

Among factors that impair DFUs healing, the formation of advanced glycation end products (AGEs) has been considered to be important mechanism delaying the healing process. Hyperglycemia caused by the lack of glucose control in diabetic patients provides the environment for glycation of structural proteins. This process is a non-enzymatic glycosylation event: A Schiff base is formed by a condensation reaction of the carbonyl group of sugar aldehydes with the N-terminus or free-amino groups via a nucleophilic addition. Through a series of rearrangements and acid-base catalysis, more

stable Amadori-products are formed. A small fraction of these Amadori-products undergo further oxidative reactions, transferred into more stable AGEs. This is an irreversible procedure and AGEs will accumulate in the tissue. The AGEs formation procedure alters peptide structure, function and stability (Huijberts, *et al*., 2008). Further conducted by Nass *et al.* suggested the glycation of platelet-derived growth factor (PDGF) results in decreased biological activity, which might contribute to reduced healing of DFUs (Nass, *et al*., 2010).

Very few observations of the glycation in DFUs have been reported. In a study by Hashmi et al., HPLC was used to analyze protein extracts from Type 2 diabetes patients' foot plantars. Greater pentosidine (a biomarker for AGEs) concentrations compared with healthy people were found (Hashmi, *et al.,* 2006). Immunofluorescence and liquid chromatography-electrospray ionization time-of-flight mass spectrometry were also employed to study the presence of N-(Carboxymethyl) lysine (CML), human skin (Kavabata *et al.*, 2011). In this study, an anti-AGE antibody (6D12), which recognizes CML was needed, and laborious sample preparation was required. Diffuse reflectance near-infrared (NIR) skin spectroscopy was used in non-invasive diabetes screening by Heise et al. A maximum accuracy of 87.8% was achieved in the classification of diabetics and non-diabetics. Due lack of extensive spectra-structure correlations, chemical and structural information from skin in the NIR spectral region is relatively limited. (Heise, *et al.*, 2006)

Significant improvements in mid-IR spectroscopic techniques in recent years has enabled the application of Fourier transform infrared (FTIR) microscopic imaging in the study of

human skin, 6,000 to 10,000 complete mid-IR spectra of skin samples can be routinely acquired from ~5 μm thick sections in 40 minutes with a pixel resolution of ~6 × 6 μm. The spectral information contained in each pixel provides a method for studying the spatial distribution of skin components and their structural properties.

In our recent studies of cutaneous wound healing, we used IR microscopic imaging to study the spatial distribution of lipid structure in an ex vivo human organ culture skin wound healing model. Carbonyl-containing lipid species with disordered chains were located within and in the vicinity of the migrating epithelial tongue (MET) during the healing process from day zero to day six. This new finding led us to propose several possibilities for biological changes during cutaneous wound healing process and validated the application of FTIR microscopic imaging to the study of wound healing.

The current thesis section presents a comparison between a non-healing DFU sample and a healing DFU sample using FTIR microscopic imaging. Different spectral regions were compared and analyzed. The difference of the C-O stretch band at ~1030 cm^{-1} is suggested to be sensitive to the degree of non-enzymatic glycation in DFUs. This new observation could be a preliminary study for the diagnosis and prognosis of DFUs healing.

5.2 Materials and Methods

5.2.1 Human diabetic foot ulcer skin sample

Human diabetic foot ulcer skin specimens at the wound site were obtained from surgery in accordance with institutional protocols at the University of Miami Miller Medical

School. One was a non-healing/delayed healing wound sample and the other was a healing wound sample.

5.2.2 IR imaging Experiments

Diabetic Foot Ulcer Samples

After surgery, samples were flash frozen with liquid nitrogen to avoid ice damage to skin structure. Skin samples preparation and IR microscopic imaging follow the protocols as introduced in Chapter 2. One set of ten images were prepared and analyzed for each specimen as shown in the results.

Control Experiment: Non-enzymatic Glycation of the Stratum Corneum

Human skin was treated with 0.5% trypsin (w/v) trypsin in pH 7.4 phosphate buffered saline solution at the air-liquid interface for one day. The stratum corneum was then peeled off, rinsed three times with distilled water, and transferred to solutions prepared as follows: pH 7.4 buffer solution was used for the control trial, 0.2 M glucose pH 7.4 buffer solution was used for the glycation trial (Delbridge, *et al.*, 1985). Stratum corneum samples were soaked in the solutions and incubated at 34.5 ℃ for 5 days. Each stratum corneum sample was removed from the solution and rinsed 5X with distilled water. After transferring to CaF_2 IR windows, these samples were air-dried for one day. IR microscopic images were collected as noted above for diabetic foot ulcer sample.

5.2.3 IR Data Analysis

ISYS software version 3.1(Malvern Instruments, LTD, UK) was used for the IR spectral analysis. Linear baseline corrections were applied to spectral regions of interest before

analyzing. Several mathematical and statistical methods such as peak height ratio, principal component analysis (PCA) and factor analysis (FA) were employed in our study. Mechanism and procedure of PCA and FA of IR images were introduced in Chapter 2. In our study, there are usually three to six factors observed in the diabetic foot ulcer data set.

5.3 Results

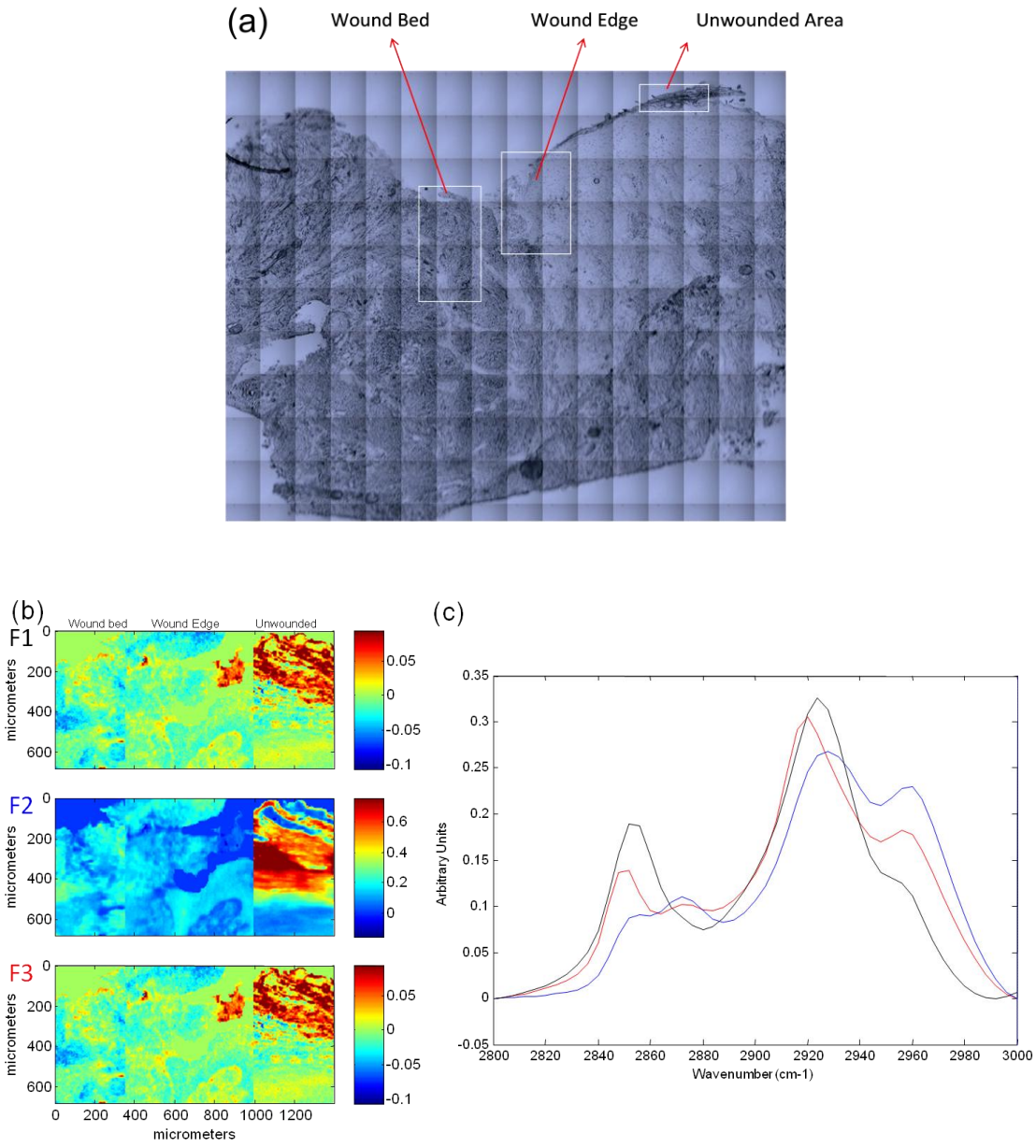

Fig. 5-1 Non-healing DFU sample: (a). Visible image of the non-healing DFU sample section. (b). IR score images of factor loadings with color coding scale bar of scores as follows: red>yellow>blue. (c). Three factor loadings in the 2800 to 3000 cm^{-1} region.

Dozens of IR images from both the healing DFU sample and the non-healing DFU sample were taken for comparison and analysis. Three different sites were chosen for image acquisition as follows: The unwounded area (healthy area), wound edge and wound bed (healed part for the healing DFU). Several images were taken from each site and representative images were selected and concatenated for analysis.

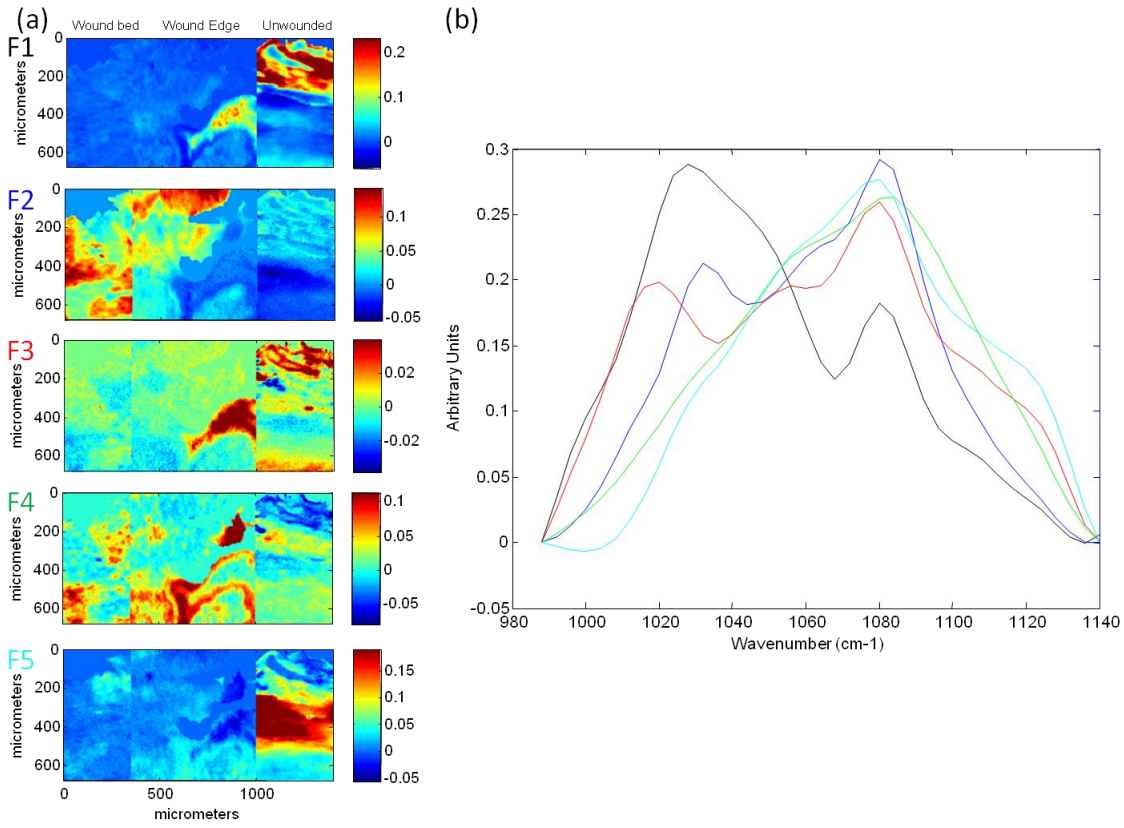

Fig. 5-2 Non-healing DFU sample: (a). IR score images of factor loadings with color coding scale bar of scores as follows: red>yellow>blue. (b). Five factor loadings in the 988 to 1140 cm-1 region.

In the factor analysis of the C-H stretch region (2800-3000 cm^{-1}) of a concatenated image containing three different sites, 3 factors were generated (Fig. 5-1), other factors that shared similar characteristics were omitted. No factor of typical collagen spectra was

observed in the image, this might due to the fact that the thickness of the sample is not deep enough to observe the dermal layer of foot skin. F1 and F3 are typical lipid spectra for SC and these two factors are mainly in the 'stratum corneum' layer of skin. F3 in the outer layer is more ordered compared with the inner layer where F1 reside. This might be explained as the differentiation of SC in the skin, however the SC here is much thicker (600 microns) than common SC (10-20 microns). F2 has a high methyl stretching signal and is close to a typical epidermis spectrum, this can be explained by the keratin rich structure of foot plantar skin (Hashmi, *et al.*, 2006).

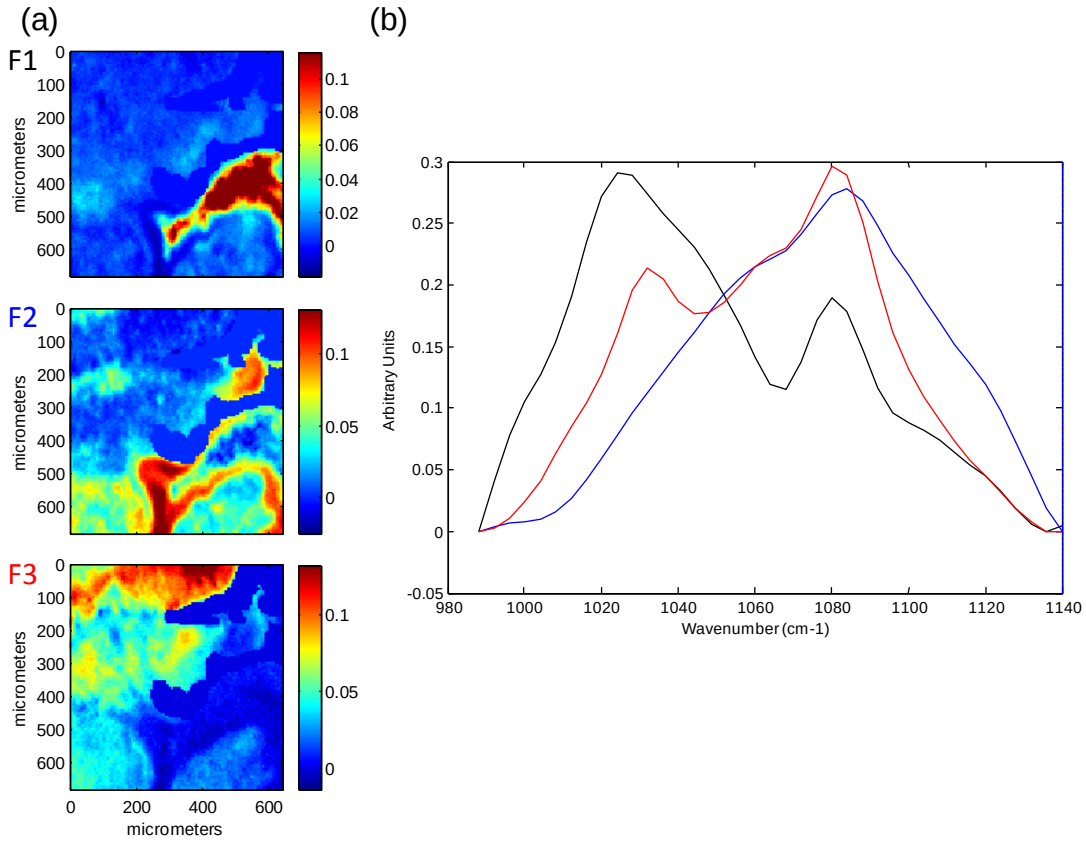

Fig. 5-3 Non-healing DFU sample: (a) Score images of three factors obeserved in the MET region, showing different glycation magnitude of proteins in different part. (b) Factor loadings of three factors .

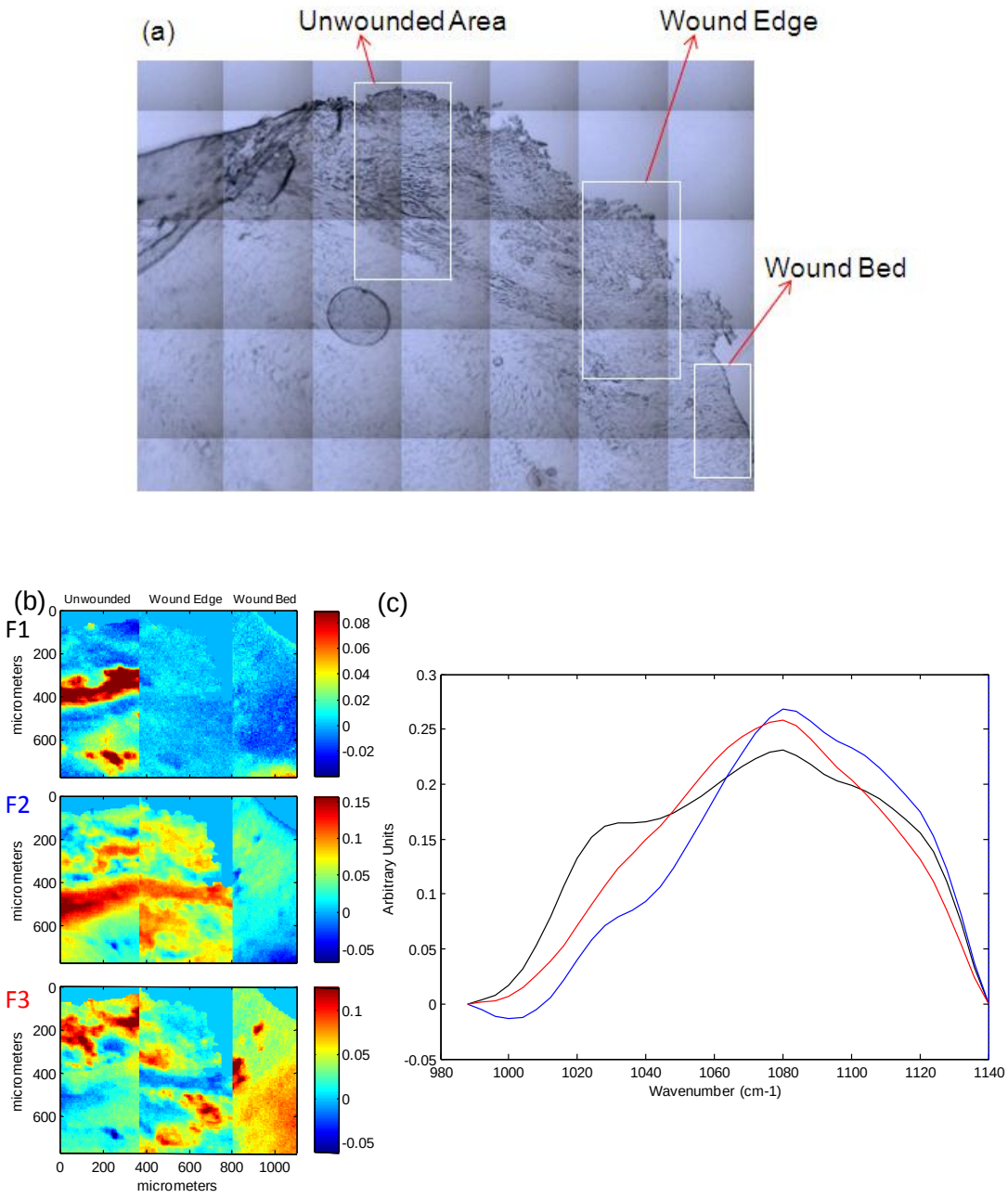

Fig. 5-4 Healing DFU sample: (a) Visible image of three different part in a healing DFU sample section. (b) Score images of three factors of three different parts in a healing DFU sample. (c) Factor loadings of F1 (black), F2 (blue), and F3 (red).

Factor analysis of 988-1140 cm^{-1} region where glucose has strong absorption was conducted (Fig. 5-2). Five distinctive factors were generated in this region and a unique factor (factor 1) not present in normal human skin was observed. Factor 1 has an intense peak at 1032 cm^{-1} and this factor only exists in the central part of the MET and in the outer layer of the SC. This peak at 1032 cm^{-1} might well arise from the glycated structure in DFU tissue. Factor 2 shows a spectral pattern similar to those observed in the normal human skin dermis layer. A similar spatial distribution to factor 1 was observed for factor 3, with lower wave numbers compared to factor 2. Factor 3 may also arise from protein glycation. Surrounding the MET and in part of the wound bed is factor 4, which has only one big peak at around 1080 cm^{-1}. Factor 5 only exists in the non-wounded area and also shows only a big peak at around 1080 cm^{-1}.

For further detailed information, 988-1140 cm^{-1} region of MET image, a single image of this area was analyzed (Fig. 5-3). Three distinctive different factors in the MET area were observed; factor 1 in the central part of MET and was surrounded factor 2, a typical factor for viable epidermis. As mentioned above in Fig. 5-2, factor 1 might be attributed to the high magnitude of protein glycation and this glycation of MET might explain the cessation of this DFU healing. Factor 3 in this analysis shows a typical pattern in epidermis.

Compared with the non-healing DFU sample, the healing DFU sample shows a quite different situation, as shown in Fig. 5-4, for the 988-1140 cm^{-1} region. No factor shows a strong band at 1032 cm^{-1} (Factor 1 in Fig. 5-3) was observed in this sample. Only factor 1 has a relatively high shoulder at the 1032 cm^{-1} region, the rest factors share similar type

of a factor for epidermis layer. From these images where Beer's law is obeyed, we can propose that the amount of glycation in the healing DFU sample is lower than the non-healing one.

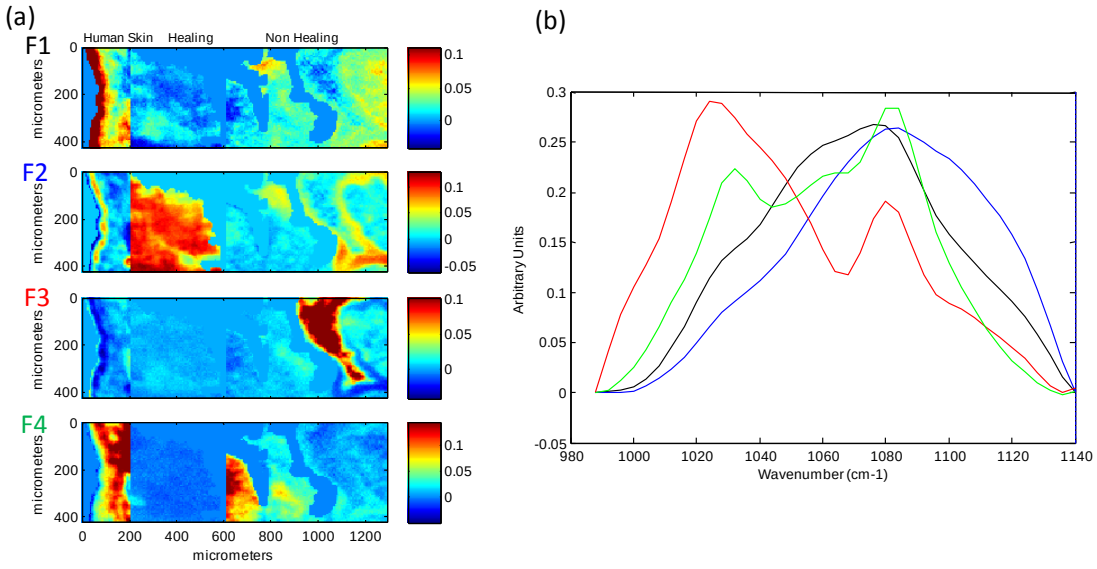

Fig. 5-5 (a) Score images of three factors obeserved in normal human skin, healing DFU, and non-healing DFU; from left to right. (b) Factor loadings of four factors

In Fig. 5-5, we compared normal human skin with the MET of a healing DFU and non-healing DFU in the 988-1140 cm^{-1} region. 4 factors were generated for comparison. Factor 1 mainly exists in the SC and in the epidermis layer in normal human skin. Factor 2 is present in all three samples. For normal human skin, it is in the viable epidermis; in the healing DFU sample, factor 2 is present throughout this region. However, in the non-healing DFU sample, it mainly is observed in the area surrounding the MET. Factor 3 shows a strong band at 1032 cm^{-1} and resides mainly in the central part of MET in the non-healing DFU. Factor 4 distributes in the dermis of normal human skin and in the wound bed of the non-healing DFU.

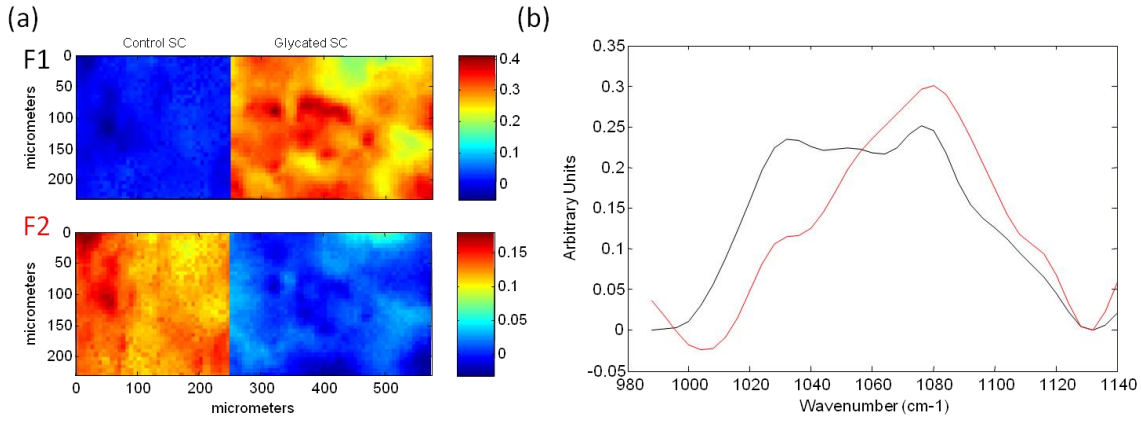

Fig. 5-6 (a) Score images of two factors showing glycation of proteins in two SC samples treated with different solutions. (b) Factor loadings of F1 (black), and F2 (red).

For further support of the proposal that the peak at 1032 cm^{-1} from glycation, a control experiment using normal skin SC was conducted and the data was analyzed as shown in Fig. 5-6. A distinctive change was observed in the 988-1140 cm^{-1} region for the glycated control SC. Factor 1 shows an obvious increase at the 1032 cm^{-1} for the glucose treated SC and this factor was not observed for the control SC sample. We can safely draw a conclusion that the peak shows at 1032 cm^{-1} is caused by the non-enzymatic glycation in the SC. Though the status of glycation of the DFU samples might be different, the SC control experiment still offers a strong supportive proof.

A univariate method, peak height ratio, was also used to compare the relative strength of peak 1032 cm^{-1} and peak 1080 cm^{-1}. As shown in Fig. 5-7, values higher than 0.8 (with a range from 0.8 to 1.5) mainly reside in the central part of MET in the non-healing DFU, where a strong band at 1032 cm^{-1} was observed in Fig. 5-5. In the peak height ratio analysis of the control experiment, similar situation was also observed. In Fig. 5-8, values higher than 0.8 only exist in the glycated SC. Though the range of values of the control

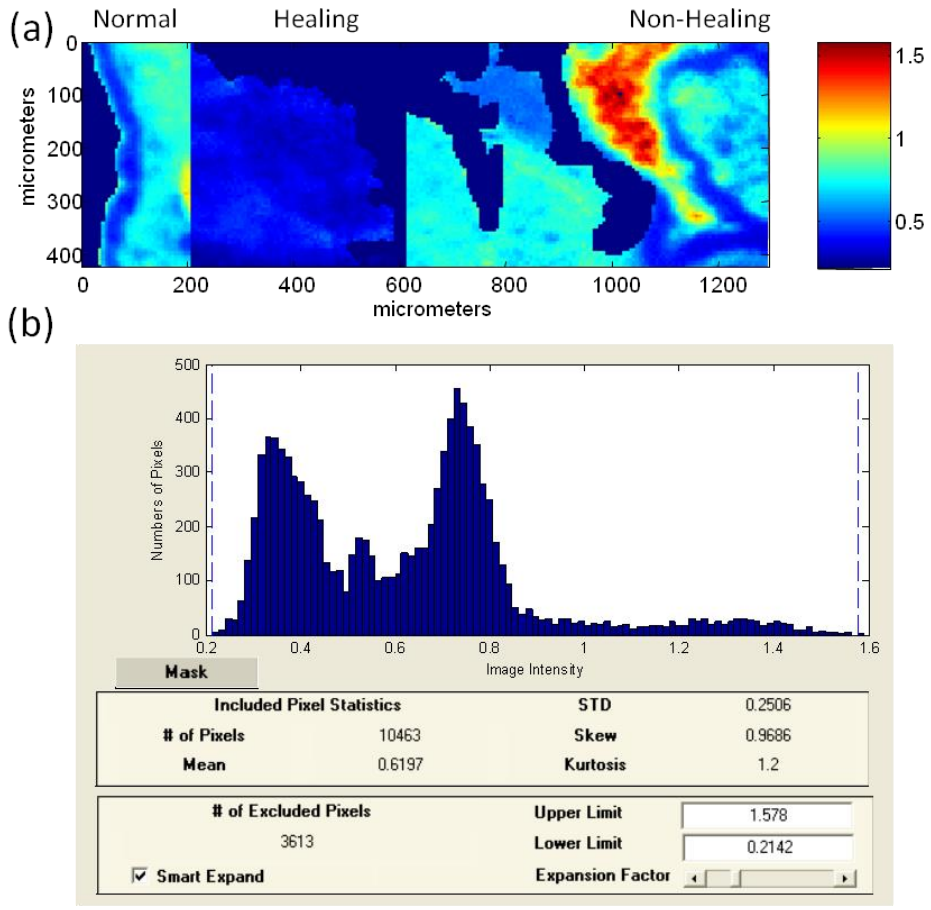

Fig. 5-7 (a) Score images of peak height ratio 1032/1080 cm^{-1} value showing normal human skin, healing DFU and non-healing DFU samples. (b) Histogram of value distribution.

experiment is lower than in the MET of non healing sample, an obvious increase of the values was observed due to glycation of the samples.

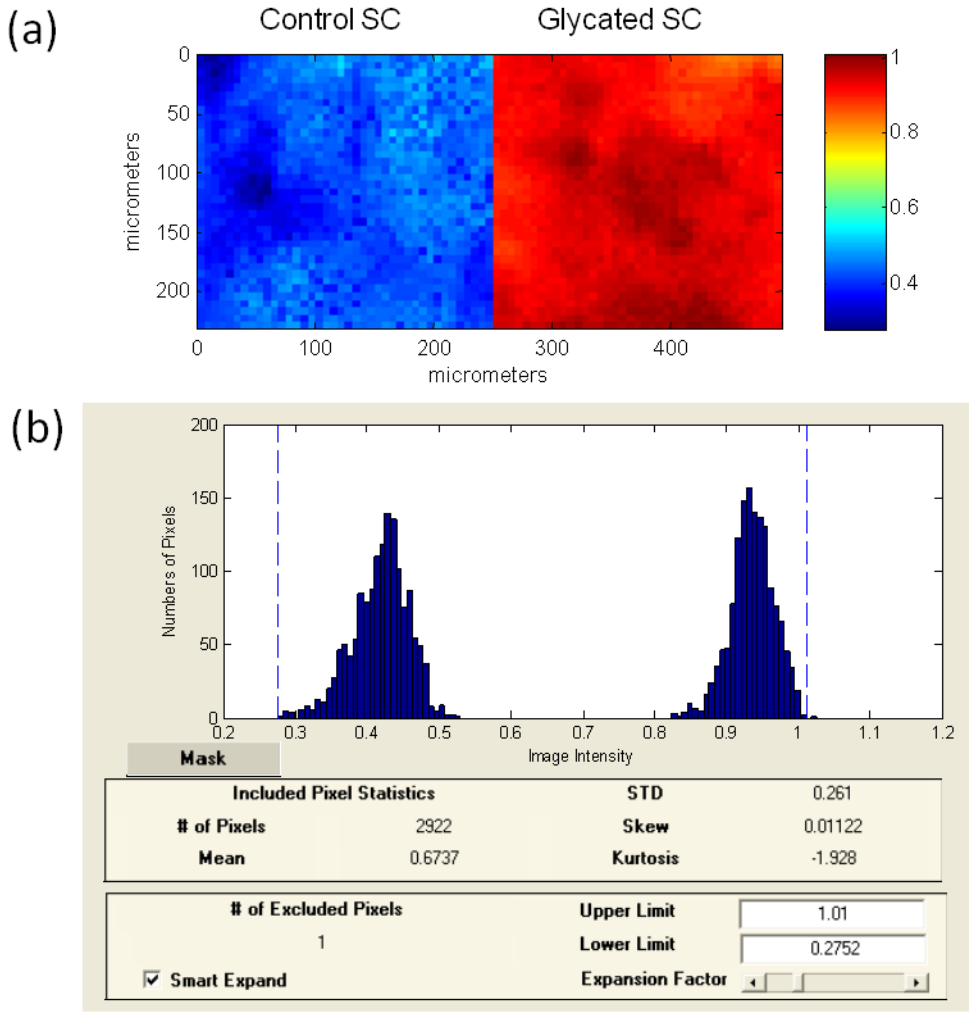

Fig. 5-8 (a) Score images of peak height ratio 1032/1080 cm^{-1} value showing control SC and glycated SC samples. (b) Histogram of value distribution.

5.5 Discussion

In the factor analysis of 988-1140 region (Fig. 5-5), Factor 1 reveals the existence of a unique chemical signature in the non-healing DFU. This factor has a high absorbance at the ~1032 cm^{-1}, which might be attributed to the C-O bond in the glucose structure. Compared with the healing DFU sample, no such a factor was observed. Factor analysis

of the MET region also shows that the glycated part exists only in the central area of the MET, whose periphery is surrounded by non-glycated structure. Molecular and biochemical confirmation of this observation need further elucidation.

As suggested by Hori et al., there are several experimental models for advanced glycation end products using albumin, collagen, elastin, etc. (Hori, *et al.*, 2012). In the current work we used normal human skin stratum corneum, which is more convenient, for the glycation model. The non-enzymatic glycation protocol by Delbridge et al. was followed (Delbridge, *et al.*, 1985). In the control experiment of non-enzymatic glycation, obvious change was observed in the 990-1100 region, which was attributed to a C-O stretching mode. The sample treated with glucose solution demonstrates a distinctive difference compared with the control sample from the same piece of skin. In addition the 1032 band contour was similar (but not identical to) that noted in the DFU. The results of this non-enzymatic glycation experiment may serve as a promising control for the explanation of the results observed in the DFU samples.

Although the application of IR imaging in the in vivo diagnosis and prognosis of DFUs healing is limited by the sample preparation requirement, this pioneering study suggests a further utility of ATR-FTIR, which does not have such a requirement, in this area. Tetteh et al. has investigated the application of ATR-FTIR spectroscopic imaging in a study of skin permeation (Tetteh, *et al.*2009). With a specific target spectral region and suitable analytical method, the technology has the distinct possibility of being applied in a (clinical) study of DFU healing.

References

Andega, S., Kanikkannan, N., and Singh, M. (2001). "Comparison of the effect of fatty alcohols on the permeation of melatonin between porcine and human skin," J. Contr. Release 77(1–2), 17–25.

Asbill, C., Kim,N., El-Kattan, A., Creek, K., Wertz, P., and Michniak, B. (2000). "Evaluation of a Human Bio-Engineered Skin Equivalent for Drug Permeation Studies," Pharm. Research. 17(9), 1092–1097.

Bakker Schut, T. C. et al., (2002). "Real-time tissue characterization on the basis of in vivo Raman spectra," J. Raman Spectrosc. 33(7), 580–585.

Balbis, A. and Posner, B. I. (2010). "Compartmentalization of EGFR in cellular membranes: role of membrane rafts," J. Cell. Biochem. 109(6), 1103–1108.

Baum, C., and Arpey, C. J. (2005). "Normal Cutaneous Wound Healing: Clinical Correlation with Cellular and Molecular Events," Dermatol Surg. 31, 674–686.

Belbachir, K. et al.. (2009). "Collagen types analysis and differentiation by FTIR spectroscopy," Anal. Bioanal. Chem. 395(3), 829–837.

Bennett, S. P., Griffiths, G.D., Schor1, A. M., Leese, G. P. and Schor, S. L. (2003). "Growth factors in the treatment of diabetic foot ulcers," British J. Surgery. 90, 133–146.

Bird, B., Miljkovic, M., Romeo, M. J., Smith, J., Stone, N., George, M.W., Diem, M. (2008). "Infrared micro-spectral imaging: distinction of tissue types in axillary lymph node histology." BMC Clinical Pathology. 8(1), 1–14.

Boateng, J. S., Matthews, K. H., Stevens, H. N.E., Eccleston, G. M. (2008). "Wound Healing Dressings and Drug Delivery Systems: A Review," J. Pham. Sci. 97(8), 2892–2923.

Bommannan, D., Potts, R. O., and Guy, R. H. (1990). "Examination of stratum corneum barrier function in vivo by infrared spectroscopy," J. Invest. Dermatol. 95(4), 403–408.

Boncheva, M. et al., (2009). "Depth profiling of Stratum corneum hydration in vivo: a comparison between conductance and confocal Raman spectroscopic measurements," Exp. Dermatol. 18(10), 870–876.

Boncheva, M., Damien, F., and Normand, V., (2008). "Molecular organization of the lipid matrix in intact Stratum corneum using ATR-FTIR spectroscopy," Biochim. Biophys. Acta 1778(5), 1344–1355.

Bouwstra, J. A. et al., (1995). "Characterization of the stratum corneum structure in reconstructed epidermis by X-ray diffraction," J. Lipid Res. 36(3), 496–504.

Bouwstra, J. A. et al., (1995). “Lipid organization in pig stratum corneum,” J. Lipid Res. 36(4), 685–695.

Bouwstra, J. A. et al., (1996). “Phase behavior of isolated skin lipids,” J. Lipid Res. 37(5), 999–1011.

Bouwstra, J. A. et al., (2008). “Water distribution and natural moisturizer factor content in human skin equivalents are regulated by environmental relative humidity,” J. Invest. Dermatol. 128(2), 378–388.

Brem, H., Balledux, J., Bloom, T., Kerstein, M. D., Hollier, L. (2000). “Healing of Diabetic Foot Ulcers and Pressure Ulcers With Human Skin Equivalent,” Arch. Surg.135(6), 627-634.

Brem. H., and Tomic-Canic, M.. (2007). “Cellular and molecular basis of wound healing in diabetes,” J. Clin. Invest. 117 (5), 1219–1222 .

Brohem, C. A. et al., (2011). “Artificial skin in perspective: concepts and applications,” Pigm. Cell Melanoma Res. 24(1), 35–50.

Bronaugh, R. L., Stewart,R. F. and Congdon, E. R. (1982). “Methods for in vitro percutaneous absorption studies II. Animal models for human skin,” Toxicol. Appl. Pharmacol. 62(3), 481–488.

Camacho, N.P., West, P., Torzilli, P. A., Mendelsohn, R. (2001) “FTIR microscopic imaging of collagen and proteoglycan in bovine cartilage.” Biopolymers. 62(1), 1–8.

Caspers, P. J. et al., (2001). “In vivo confocal Raman microspectroscopy of the skin: noninvasive determination of molecular concentration profiles,” J. Invest. Dermatol. 116(3), 434–442.

Caspers, P. J. et al., (2002). “Monitoring the penetration enhancer dimethyl sulfoxide in human stratum corneum, in vivo by confocal Raman microscopy,” Pharm. Res. 19(10), 1577–1580.

Caspers, P. J., Lucassen, G. W. and Puppels, G. J. (2003). “Combined in vivo confocal Raman spectroscopy and confocal microscopy of human skin,” Biophys. J. 85(1), 572–580.

Chan, K. L. A. et at., (2008). “A coordinated approach to cutaneous wound healing: vibrational microspectroscopic imaging and molecular biology,” J. Cell. Mol. Med. 12(5B), 2145–2154.

Chen, H-C. et al., (2001). “Effect of cholesterol on miscibility and phase behavior in binary mixtures with synthetic ceramide 2 and octadecanoic acid. Infrared studies,” Biochim. Biophys. Acta 1512(2), 345–356.

Clark, R. A.F., Ghosh, K. and Tonnesen, M. G. (2007), “Tissue Engineering for Cutaneous Wounds,” J. Inv. Derm. 127, 1018–1029.

Coulombe, P. A. (2003). “Wound epithelialization: accelerating the pace of discovery,” J. Invest. Dermatol. 121(2), 219–230.

DeLangen, M., Luigjes, H., and Prins, K. O. (2000). “NMR study of chain dynamics in the hexagonal high-pressure phase of polyethylene,” Polymer 41(3), 1193–1203.

Delbridge, L., Ellis, C.S., Robertson, K., Lequesne, L.P. (1985). “Non-enzymatic glycosylation of keratin from the stratum corneum of the diabetic foot,” British J.Derma.112, 547-554.

Gazi, E. et al., (2007). “Direct evidence of lipid translocation between adipocytes and prostate cancer cells with imaging FTIR microspectroscopy,” J. Lipid Res. 48(8), 1846–1856.

Gieringer, M., Elliott, K., Gosepath, J. and Naim, R. (2010). “Keloids: Fundamental Principles and Prospects (Review),” Molec. Med. Reports. 3, 13–19.

Gooris, G. S. and Bouwstra, J. A. (2007). “Infrared spectroscopic study of stratum corneum model membranes prepared from human ceramides, cholesterol, and fatty acids,” Biophys. J. 92(8), 2785–2795.

Gurtner, G. C., Werner, S., Barrandon, Y. and Longaker, M. T. (2008). “Wound Repair and Regeneration,” Nature. 453, 314–321.

Hardle, W., Simar, L. (2012). Applied Multivariate Statistical Analysis (Third Edition). Springer. ISBN 978-3-642-17228-1.

Hashmi, F., Malone-Lee, J., Hounsell, E. (2006). “Plantar skin in type II diabetes: an investigation of protein glycation and biomechanical properties of plantar epidermis,” Eur. J. Dermatol. 16 (1), 23–32.

Hattori, N., Carrino, D. A., Lauer, M. E., Vasanji, A., Wylie, J. D., Nelson, C. M., and Apte, S. S. (2011). “Pericellular Versican Regulates the Fibroblast-Myofibroblast Transition: A Role For Adamts 5 Protease-Mediated Proteolysis,” J. Bio. Chem. 286(39), 34298–34310.

Heise, H.M., Haiber, S., Licht, M., Ihrig, D.F., Moll, C., and Stücker, M. (2006). “Recent progress in non-invasive diabetes screening by diffuse reflectance near-infrared skin spectroscopy,” Proc. of SPIE. Vol. 6093, 609310.

Hori, M., Yagi, M., Nomoto, K., Ichijo, R., Shimode, A., Kitano, T., Yonei, Y. (2012). “Experimental Models for Advanced Glycation End Product Formation Using Albumin, Collagen, Elastin, Keratin and Proteoglycan,” Anti-Aging Med. 9 (6), 125-134.

Hudson, L. G. and McCawley, L. J. (1998). “Contributions of the epidermal growth factor receptor to keratinocyte motility,” Microsc. Res. Tech. 43(5), 444–455.

Huijberts, M. S. P., Schaper, N. C., Schalkwijk, C. G. (2008). "Advanced glycation end products and diabetic foot disease," Diabetes Metab. Res. Rev. 24(Suppl 1): S19–S24.

Jackson, M. et al. (1995). "Beware of connective tissue proteins: assignment and implications of collagen absorption in infrared spectra of human tissues," Biochim. Biophys. Acta 1270(1), 1–6.

Jiang, C.-K. et al., (1993). "Epidermal growth factor and transforming growth factor a specifically induce the activation- and hyperproliferationassociated keratine 6 and 16," Proc. Natl. Acad. Sci. USA 90(14), 6786–6790.

Kawabata, K., Yoshikawa, H., Saruwatari, K., Akazawa, Y., Inoue, T., Kuze, T., Sayo, T., Uchida, N., Sugiyama, Y., (2011). "The presence of N^{ε}-(Carboxymethyl) lysine in the human epidermis," Bioch. et Biophy. Acta. 1814, 1246 – 1252.

Kelley, S. B., Olerud, J. E., Witztum, J. L., Curtiss, L. K., Gown, A. M., Odland, G. F. (1989). "A method for localizing the early products of nonenzymatic glycosylation in fixed tissue," J. Invest. Dermatol. 93(3), 327-331.

Kozel'tsev, V. L. et al., (2006). "Changes in wound field lipids in rat skin," Bull. Exp. Biol. Med. 142(4), 493–494.

Lademann, J. et al., (2005). "Application of optical coherent tomography for skin diagnostics," Laser Phys. 15(2), 288–294.

Lambert, S. et al., (2008). "Internalization of EGF receptor following lipid rafts disruption in keratinolcytes is delayed and dependent on p38 MAPK activation," J. Cell. Physiol. 217(3), 834–845.

Lambert, S., Gniadecka, R. and Poumay, Y. (2009). "Cholesterol and lipid rafts as regulators of signaling through the EGF receptor in keratinocytes," Open Dermatol. J. 3(2), 151–158.

Lazo, N.D., Meine, J.G., Downing, D.T. (1995). "Lipids are covalently attached to rigid corneocyte protein envelopes existing predominantly as β-sheets: a solid-state nuclear magnetic resonance study," J. Invest. Dermatol. 105, 296–300.

Leung, P. C., (2007) "Diabetic foot ulcers - a comprehensive review," *Surgeon*. 5(4), 219-231. The Royal Colleges of Surgeons of Edinburgh and Ireland

Liao, H., Zakhaleva, J., Chen, W. (2009). "Cells and tissue interactions with glycated collagen and their relevance to delayed diabetic wound healing," Biomaterials 30, 1689–1696.

Lin, S. Y., Duan, K. J., and Lin, T. C., (1996). "Microscopic FT-IR/DSC system used to simultaneously investigate the conversion process of protein structure in porcine stratum

corneum after pretreatment with skin penetration enhancers," Methods Find. Exp. Clin. Pharmacol. 18(3), 175–181.

Luo, S., Yufit, T., Carson, P., Fiore, D., Falanga, J., Lin, X., Mamakos, L., Falanga, V. (2011). "Differential Keratin Expression During Epiboly in a Wound Model of Bioengineered Skin and in Human Chronic Wounds," The Inter. J. Lower Extremity Wounds. 10(3), 122–129.

MacNeil, S. (2007). "Progress and opportunities for tissue-engineered skin," Nature. 445, 874–880.

Mao, G. et al., (2012). "Imaging the distribution of sodium dodecyl sulfate in skin by confocal Raman and infrared microspectroscopy," Pharm. Res. 29(8), 2189–2201.

Mathay, C. et al., (2008). "Heparin-binding EGF-like growth factor is induced by disruption of lipid rafts and oxidative stress in keratinocytes and participates in the epidermal response to cutaneous wounds," J. Invest. Dermatol. 128(3), 717–727.

Mazie, A. R. et al., (2006). "Epithelial cell motility is triggered by activation of the EGR receptor through phosphatidic acid signaling," J. Cell Sci. 119(8), 1645–1654.

Mendelsohn, R. and Mantsch, H. H. (1986). "Fourier transform infrared studies of lipid-protein interaction," in Progress in Protein-Lipid Interaction, A. Watts and J. J. H. M. de Pont, eds., Elsevier, Amsterdam, Vol. 2, pp. 103–146.

Mendelsohn, R. and Mantsch, H. H. (1986). "Fourier transform infrared studies of lipid/protein interaction," Chapter 4 in Progress in Protein-Lipid Interactions 2, A. Watts and J. J. H. H. M. de Pont, Eds., pp. 103– 146, Elsevier, Amsterdam, Netherlands.

Mendelsohn, R. et al., (2003). "Infrared microspectroscopic imaging maps the spatial distribution of exogenous molecules in skin," J. Biomed. Opt. 8(2), 185–190.

Monteiro-Riviere, N. A. et al., (1997). "Comparison of an in vitro skin model to normal human skin for dermatological research," Microsc. Res. Tech. 37(3), 172–179.

Moore, D. J. et al., (2006). "Kinetics of membrane raft formation: fatty acid domains in stratum corneum lipid models," J. Phys. Chem. B 110(5), 2378–2386.

Moore, D. J., Rerek, M. E., and Mendelsohn, R. (1997). "FTIR spectroscopy of the conformational order and phase behavior of ceramides," J. Phys. Chem. B 101(44), 8933–8940.

Moore, D. J., Rerek,M. E. and Mendelsohn, R. (1997). "Lipid domains and orthorhombic phases in model stratum corneum: evidence from Fourier transform infrared spectroscopy studies," Biochem. Biophys. Res. Commun. 231(3), 797–801.

Murdock, J. N., et al., (2010). "Measuring cellular-scale nutrient distribution in algal biofilms with synchrotron confocal infrared microspectroscopy," Spectroscopy. 25(10), 32–41.

Naik, A. et al., (1995). "Mechanism of oleic acid-induced skin penetration enhancement in vivo in humans," J. Contr. Release 37(3), 299–306.

Nass, N., Vogel, K., Hofmann, B., Presek, P., Silber, R. E., Simm, A. (2010). "Glycation of PDGF results in decreased biological activity," Inter. J. of Biochem. & Cell Bio. 42, 749–754.

Netzlaff, F. et al., (2005). "The human epidermis models EpiSkin®, SkinEthic® and EpiDerm®: an evaluation of morphology and their suitability for testing phototoxicity, irritancy, corrosivity, and substance transport," Eur. J. Pharm. Biopharm. 60(2), 167–178.

Patel, G. K. et al., (2006). "Numerous keratinocyte subtypes involved in wound re-epithelialization," J. Invest. Dermatol. 126(2), 497–502.

Pensack, R. D. et al., (2006). "Infrared kinetic/structural studies of barrier reformation in intact stratum corneum following thermal perturbation," Appl. Spectrosc. 60(12), 1399–1404.

Percot, A. and Lafleur, M. (2001). "Direct observation of domains in model stratum corneum lipid mixtures by Raman microspectroscopy," Biophys. J. 81(4), 2144–2153.

Pierce, M. C. et al., (2004). "Advances in optical coherence tomography imaging for dermatology," J. Invest. Dermatol. 123(3), 458–463.

Pike, L. J., Han,X., and Gross, R.W. (2005). "Epidermal growth factor receptors are localized to lipid rafts that contain a balance of inner and outer leaflet lipids," J. Biol. Chem. 280(29), 26796–26804.

Ponec, M. et al., (2000). "Lipid and ultrastructural characterization of reconstructed skin models," Int. J. Pharm. 203(1–2), 211–225.

Ponec, M. et al., (2001). "Barrier function in reconstructed epidermis and its resemblance to native human skin," Skin Pharmacol. Appl. Skin Physiol. 14(Suppl.1), 63–71.

Pouliot, R., Germain, L., Auger, F. A., Tremblay, N., Juhasz, J. (1999). "Physical characterization of the stratum corneum of an in vitro human skin equivalent produced by tissue engineering and its comparison with normal human skin by ATR-FTIR spectroscopy and thermal analysis (DSC)," Bioch. et Biophy. Acta. 1439, 341–352.

Repertinger, S. K. et al., (2004). "EGFR enhances early healing after cutaneous incisional wounding," J. Invest. Dermatol. 123(5), 982–989.

Rerek, M. E. et al., (2005). “FTIR spectroscopic studies of lipid dynamics in phytosphingosine ceramide models of the stratum corneum lipid matrix,” Chem. Phys. Lipids 134(1), 51–58.

Ringerike, T. et al.. (2001). “Cholesterol is important in control of EGF receptor kinase activity but EGF receptors are not concentrated in caveolae,” J. Cell Sci. 115(6), 1331–1340.

Schubert, J. M., Bird, B., Papamarkakis, K., Miljković, M., Bedrossian, K., Laver, N., Diem, M. (2010). “Spectral cytopathology of cervical samples: detecting cellular abnormalities in cytologically normal cells.” Lab. Invest. 90, 1068–1077.

Singer, A. J. and Clark,R. A. F. (1999). “Cutaneous wound healing,” N. Engl. J. Med. 341(10), 738–746.

Snyder, R. G. (1961). “Vibrational spectra of crystalline n-paraffins. Part II. Intermolecular effects,” J. Mol. Spectrosc. 7(1–6), 116–144.

Snyder, R. G. (1979). “Vibrational correlation splitting and chain packing for the crystalline n-alkanes,” J. Chem. Phys. 71(8), 3229–3235.

Snyder, R. G., (1967). “Vibrational study of the chain conformation of the liquid n-paraffins and molten polyethylene,” J. Chem. Phys. 47(4), 1316–1360.

Tetteh, J., Mader, K.T., Andanson, J.-M., McAuley, W.J., Lane, M.E., Hadgraft, J., Kazarian, S.G., Mitchell, J.C. (2009). “Local examination of skin diffusion using FTIR spectroscopic imaging and multivariate target factor analysis,” 642(1–2), 246–256.

Tfayli, A. et al., (2007). “Molecular characterization of reconstructed skin model by Raman microspectroscopy: comparison with excised human skin,” Biopolymers 87(4), 261–274.

Tobin, D. J. (2006), “Biochemistry of Human Skin—Our Brain on The Outside,” Chem. Soc. Rev. 35, 52–67.

Tomic-Canic, M. et al., (2007). “Streptolysin O enhances keratinocyte migration and proliferation and promotes skin organ culture wound healing in vitro,” Wound Repair Regen. 15(1), 71–79.

Toriseva, M., b and Kähäri, V. M. (2009). “Proteinases in Cutaneous Wound Healing,” Cell. Mol. Life Sci. 66, 203–224.

Usui, M. L. et al., (2005). “Morphological evidence for the role of suprabasal keratinocytes in wound reepithelialization,” Wound Repair Regen. 13(5), 468–479.

Usui, M. L., Mansbridge, J. N., Carter, W. G., Fujita, M., and Olerud, J. E. (2008). “Keratinocyte Migration, Proliferation, and Differentiation in Chronic Ulcers From

Patients With Diabetes and Normal Wounds," J. Histochem. & Cytochem. 56(7), 687–696.

Vicanova, J. et al., (1998). "Stratum corneum lipid composition and structure in cultured skin substitutes is restored to normal after grafting onto athymic mice," J. Invest. Dermatol. Symp. Proc. 3(2), 114–120.

Wagner, H. et al.. (2001). "Interrelation of permeation and penetration parameters obtained from in vitro experiments with human skin and skin equivalents," J. Contr. Release 75(3), 283–295.

Walters, K. A. and Roberts, M. S. (2002). Dermatological and Transdermal Formulations. Chapter 1: The Structure and Function of Skin. Marcel Dekker, Inc. ISBN: 0-8247-9889-9. 1–40.

Wetzel, D. et al., (2011). "Synchrotron infrared confocal microspectroscopic spatial resolution or a customized synchrotron/focal plane array system enhances chemical Imaging of biological tissue or cells," Nuclear Instru. and Met. in Phy. Res. A. 649, 179–183

Yeh, A. T. et al., (2004). "Imaging wound healing using optical coherence tomography and multiphoton microscopy in an in vitro skin-equivalent tissue model," J. Biomed. Opt. 9(2), 248–253.

Zhang, G. et al., (2006). "Vibrational microspectroscopy and imaging of molecular composition and structure during human corneocyte maturation," J. Invest. Dermatol. 126(5), 1088–1094.

Zhang, G. et al., (2007). "Imaging the prodrug-to-drug transformation of a 5-Fluorouracil derivative in skin by confocal Raman microscopy," J. Invest. Dermatol. 127(5), 1205–1209.

Zhang, G. et al., (2007). "Vibrational microscopy and imaging of skin: from single cells to intact tissue," Anal. Bioanal. Chem. 387(5), 1591–1599.

List of Publications

Publications at Rutgers University:

1. Guo Yu, Olivera Stojadinovic, Marjana Tomic-Canic, Carol R. Flach, and Richard Mendelsohn; "Infrared microscopic imaging of cutaneous wound healing: lipid conformation in the migrating epithelial tongue." Journal of Biomedical Optics 17(9), 096009 (September 2012) ;
2. Guo Yu, Guojin Zhang, Carol R. Flach, and Richard Mendelsohn; "Vibrational spectroscopy and microscopic imaging: novel approaches for comparing barrier physical properties in native and human skin equivalents." Journal of Biomedical Optics 18(6), 061207 (June 2012) ;
3. Pui Lam Chiu, Daniel D. T. Mastrogiovanni, Dongguang Wei, Cassandre Louis, Min Jeong, Guo Yu, Peter Saad, Carol R. Flach, Richard Mendelsohn, Eric Garfunkel, and Huixin He; "Microwave- and nitronium ion-enabled rapid and direct production of highly conductive low-oxygen graphene." Journal of the American Chemical Society, Volume 134, Issue 13, 5850–5856; (April 4, 2012);

Publications at Peking University:

1. Guo Yu, Zemei Ge, Tieming Cheng and Runtao Li; L-Proline-based phosphamides as a new kind of organocatalysts for asymmetric direct Aldol reactions; Chinese Journal of Chemistry Volume 26, Issue 5, 911–915, (May, 2008).

Curriculum Vitae

Birth: January 1, 1983, in Changsha, Hunan, China

Education:

09/2008-05/2013	Ph.D., Chemistry, Rutgers University-Newark Campus Advisor: Dr. Richard Mendelsohn
09/2005-12/2007	M. Sc., Chemical Biology, Peking University Advisor: Dr. Runtao Li
09/2001-06/2005	B. Sc., Pharmaceutical Sciences, Peking University